THE RESTRICTED FULL THREE BODY PROBLEM: APPLICATIONS TO BINARY ASTEROID EXPLORATION

by

Julie Bellerose

A dissertation submitted in partial fulfillment
of the requirements for the degree of
Doctor of Philosophy
(Aerospace Engineering)
in The University of Michigan
2008

Doctoral Committee:

Professor Daniel J. Scheeres, University of Colorado at Boulder, Chair
Professor N. Harris McClamroch
Professor Nilton O. Renno
Professor Peter D. Washabaugh
Assistant Professor Anouck R. Girard

To my parents, Rolland and Denise

ACKNOWLEDGEMENTS

First, I would like to thank my advisor Professor Daniel Scheeres. This work would not have been possible without his advice, guidance and teaching. I also thank my doctoral committee for providing comments and feedback on this work during the past years that I have been studying in Michigan. I would like to extend this acknowledgement to the faculty, staff and students in the Aerospace department, or connected, with whom I had an extraordinary time.

I would like to acknowledge support via Fellowships from the Natural Sciences and Engineering Research Council of Canada and the Canadian Space Agency, which supported my doctoral program.

This research was funded, in part, by a grant from the Jet Propulsion Laboratory/California Institute of Technology Director's Research and Development Fund. Special thanks go to Mr. Steven Chesley and Dr. Alan Chamberlin in the Solar System Dynamics group at JPL for providing me the Near Earth Asteroids close approach data files, which numbered to about 5000 files. The data was produced using the JPL Near Earth Object Program (www.neo.jpl.gov).

Finally, I would like to thank all my friends and family. And I dedicate this dissertation to my parents.

PREFACE

This dissertation was submitted at the University of Michigan in partial fulfillment of the requirements for the degree of Doctor of Philosophy in Aerospace Engineering, and defended on April 16 2008. The doctoral committee was composed of Professor Daniel Scheeres, committee chair, Professor Harris McClamroch, Professor Peter Washabaugh, Professor Nilton Renno, and Assistant Professor Anouck Girard. This thesis is a comprehensive work based on the following papers that have been published in journals and presented at conferences:

Publications

J. Bellerose and D.J. Scheeres, 2008, General Dynamics in the Restricted Full Three Body Problem, *Acta Astronautica*, 62 (10-11), 563-576.

J. Bellerose and D.J. Scheeres, 2008, The Restricted Full Three-Body Problem: Application to Binary System 1999 KW4, *Journal of Guidance, Control, and Dynamics*, 31 (1), 162-171.

J. Bellerose and D.J. Scheeres, 2008, Energy and Stability in the Full Two Body Problem, *Celestial Mechanics and Dynamical Astronomy*, 100 (1), 63-91.

J. Bellerose and D.J. Scheeres, 2007, Stability of Equilibrium Points in the Restricted Full Three Body Problem, *Acta Astronautica*, 60, 141-152.

D.J. Scheeres et al., 2006, Dynamical Configuration of Binary Near-Earth Asteroid (66391) 1999 KW, *Science*, 314 (5803), 1280-1283.

S.J. Ostro et al., 2006, Radar Imaging of Binary Near-Earth Asteroid (66391) 1999 KW4, *Science*, 314 (5803), 1276-1280.

D.J. Scheeres and J. Bellerose, 2004, The Restricted Hill Full 4-Body Problem: Application to spacecraft motion about binary asteroids, special edition of Dynamical Systems, M.Dellnitz and J.E.Marsden.

Conferences

J. Bellerose and D.J. Scheeres, 2008, Mission to Binary Asteroids: 1999 KW4 as a Case Study, Spaceflight Mechanics Meeting, Galveston, TX, AAS 08-170.

D.J. Scheeres, E.G. Fahnestock, and J. Bellerose, 2008, Binary Asteroid System Dynamics and Scientific Investigations, presented at the first IPEWG Meeting in Okinawa, Japan (January 2008).

J. Bellerose and D.J.Scheeres, 2007, Mission Design to Binary Asteroid Systems, International Astronautical Congress, IAC-07-C1.4.05, Hyderabad, India.

J. Bellerose and D.J. Scheeres, 2007, Dynamics of the Restricted Full Three-Body Problem, presentation at CanCam 2007, June 2007, Toronto, Canada.

J. Bellerose and D.J. Scheeres, 2007, Periodic Orbits in the Restricted Full Three-Body Problem, presentation at the Division of Dynamical Astronomy (DDA) Conference, May 2007, Ann Arbor, MI.

J. Bellerose and D.J.Scheeres, 2007, Energy Constraints in the Restricted Full Three-Body Problem: Application to Binary System 1999 KW4, Spaceflight Mechanics Conference, Sedona, AZ, AAS-07-224.

J. Bellerose and D.J.Scheeres, 2006, General Dynamics in the Restricted Full Three-Body Problem for an Ellipsoid-Sphere System, IAC05-C1.5.05, Spain.

J. Bellerose and D.J.Scheeres, 2006, Periodic Orbits in the Full Two-Body Problem, AAS 06-169, Florida.

J. Bellerose and D.J.Scheeres, 2005, Periodic Orbits in the Restricted Full Three-Body Problem for an Ellipsoid-Sphere System, IAC05-C1.6.02, Japan.

J. Bellerose and D.J.Scheeres, 2005, Periodic Orbits in the vicinity of the Lagrangian Points of Restricted Full Three-Body Problem, AAS 05-295, Lake Tahoe, CA.

J. Bellerose and D.J. Scheeres, 2004, Stability of Equilibrium Points in the Restricted Full Three Body Problem, IAC-04-A.7.03 , Vancouver, Canada.

TABLE OF CONTENTS

LIST OF FIGURES

LIST OF TABLES

CHAPTER 1

INTRODUCTION

1.1 Missions to Small Bodies of our Solar System

Over the past decade, robotic missions have been sent to small bodies, providing a basic understanding of their environment. Although some missions such as Galileo visited a few small bodies on their way to other planets, NASA launched its first asteroid mission in early 1996 with NEAR, arriving at the asteroid Eros in 2000 and landing on it in 2001 around Valentine's day [32]. Stardust followed by taking samples of a comet's tail, comet Wild 2, in 2004, after a flyby of asteroid Annefrank two years earlier [37]. Deep Impact was sent to comet Tempel 1 and impacted it in 2005, revealing its internal structure in more details [35]. Then, NASA launched New Horizons Pluto-Charon in early 2006 to the Pluto-Charon system, which is the first mission going to that binary system. New Horizons is scheduled to arrive at Pluto in 2015, continuing its exploration to the Kuiper Belt objects in the 2016-2020 time frame [33]. The NASA mission DAWN was just launched in the Fall 2007, on its way to asteroids Vesta and Ceres arriving in 2011 and 2015, respectively [29]. The European Space Agency (ESA) sent Rosetta in 2004 to comet 67P/Churyumov-Gerasimenko. Rosetta will fly by two asteroids, Stein and Lutetia, on September 2008 and July 2010, respectively, before orbiting Gerasimenko for 17 months when it reaches its target in 2014 [40]. The Japanese Aerospace Exploration Agency (JAXA) may have the first sample return mission, Hayabusa (Muses-C),

Mission	Space Agency	Comments
Hayabusa-2	JAXA	2^{nd} sample return (SR) to asteroid
Marco Polo	JAXA, ESA	SR to dormant comet or binary system
LEONARD	CNES	Binary system 1999FG3 as possible target
Ishtar	UK	Study of internal composition of asteroid
Simone	UK	Collaborating spacecraft to NEAs
Apies	UK	Collaborating spacecraft to NEAs
Don Quijote	ESA	Orbiter and impactor study at asteroid
NEASR-TRS	ESA	Asteroid SR mission
Phobos-grunt	Russia, ESA	Landing on Phobos, moon of Mars
PRIME	CSA (UWO)	Landing on Phobos, moon of Mars
AsteroidFinder	DLR	Asteroid observation program
ASTEX	DLR	In situ investigation of NEAs
Stardust-Next	NASA	Study comet Tempel-1 in more details
WISE	NASA	IR survey mission for NEO population
NEOStar	NASA	Space-based NEO detection

Table 1.1: Current mission proposals by space agencies presented at the First Meeting of The International Primitive Body Exploration Working Group (IPEWG), held in Japan in January 2008 [62]. See references [56, 98, 95, 41, 16, 39, 42, 34, 38, 51, 48, 47, 43, 36].

reaching the asteroid Itokawa in 2005. The mission is now on its way back to Earth [49, 21, 57].

New missions to small bodies are under development or under concept studies by several space agencies. The mission proposals are listed and described in Table 1.1. Note that a few of them, such as Marco Polo and LEONARD are looking at a recently discovered type of asteroid system, binary asteroids, as possible targets.

Since these small bodies have not been subjected to erosion or high pressures, and are believed to have formed during the early stage of our solar system, studying small bodies on a close scale may answer some fundamental questions about the formation and evolution of our solar system. Some of these small body systems are found to be in pairs with the two bodies in orbit about each other, and are usually called binary asteroids. It is currently estimated that about sixteen percent of the Near Earth Asteroid population may be binaries [55]. Current interest in studying Near Earth

Objects involves finding more about their external and internal composition. A few studies have looked at the possible formation path of binary systems, involving formation through fission of a single asteroid [82], planetary flybys [96, 73, 17], or capture of one or more bodies [87, 54]. To give support to these theories, research into small body ephemerides from the JPL Near Earth Object Program [31, 30] also indicates that some of these systems have gone through frequent flybys of the Earth and other planets of our solar system. A binary system formed from a single body may give a direct view on its interior. Hence, a binary asteroid system can give insights into both the geology and dynamics of asteroids, motivating this research.

Sending a spacecraft to these systems is not trivial. A binary system is in fact a mini "three-body problem" such as the motion of a spacecraft in the Earth-Moon system. However, in the binary case, one needs to account for the non-spherical shape of the bodies. Despite the low gravity accelerations, astronomical observations indicate that the time scale of motion around these systems are on the order of 10's of hours. It has also been shown that the motion is strongly perturbed by the system itself, close approaches to other bodies and solar effects [71, 55, 87, 81, 17, 96]. Hence, this research develops and investigates dynamical models for the motion of a binary system, as well as for a spacecraft in its vicinity.

1.2 Literature Review and Contributions

1.2.1 The Full Two Body Problem

Studying the motion of two bodies in space is not a new problem in itself. The Two-Body Problem is commonly used for trajectory analysis. The problem becomes computationally hard when the mass distribution of the bodies are taken into account, referred to as the Full Two-Body Problem shown in Figure 1.1, where R, V, Ω_1, and Ω_2 are the position, velocity, and angular velocities of the system. The problem formulation of the "full" binary system itself has been posed and studied in

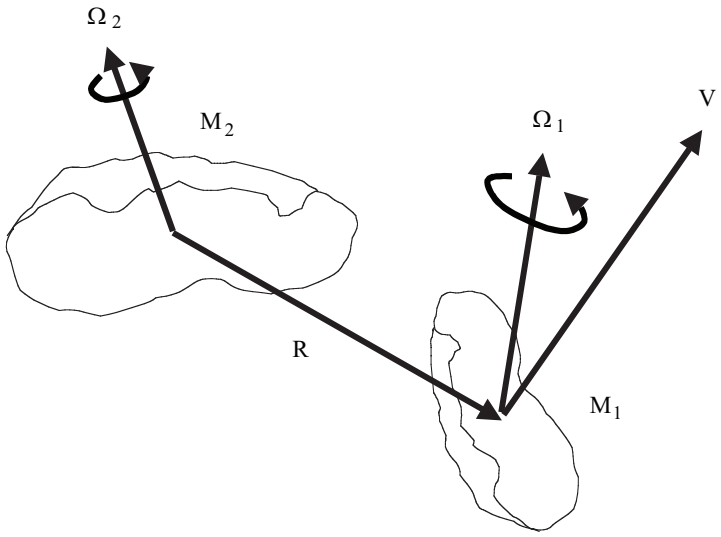

Figure 1.1: Full 2-Body Problem (F2BP).

earlier works, see [53, 80, 79, 84, 86, 52, 22]. A general formulation is possible, and was first discussed in [53, 15] for different shapes, where mutual potential expressions, methods of reduction, and equilibrium solutions were also derived. Among other derived methods of computations, reference [86] approached the problem using polyhedral mutual potential and potential derivatives while other studies have used other mathematical methods such as Lie group computations [52].

To reduce the number of degrees of freedom, a method of reduction for the F2BP is to assume one of the bodies to be a sphere, as shown in Figure 1.2. Note that the angular velocity of the sphere is now trivial. At the simplest, one can retrieve the problem of asteroid orbiters. The conditions for relative equilibria and their stability in the F2BP are derived in [80] for a system with one of the bodies being a sphere while the other one is of arbitrary shape. An ellipsoid-sphere system was further investigated in [79, 84], on which the current document builds up. The ellipsoid-sphere system provides a first-order approximation giving accurate insights on the dynamics of the real system, and can easily accommodate the partial

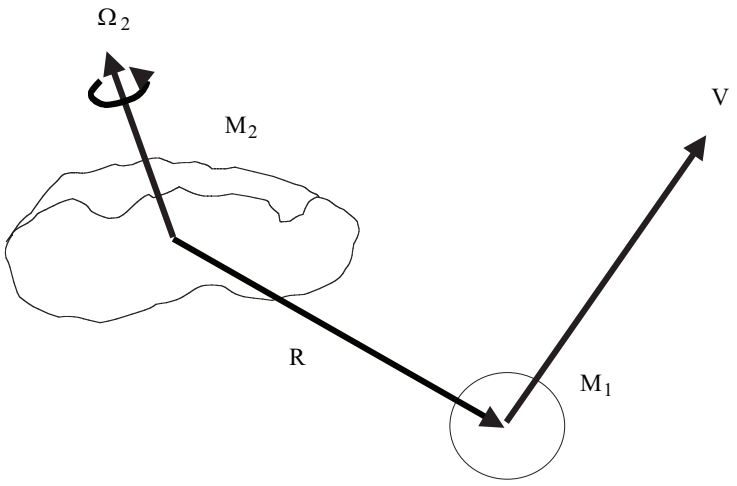

Figure 1.2: The Full Two Body Problem under "Sphere Restriction".

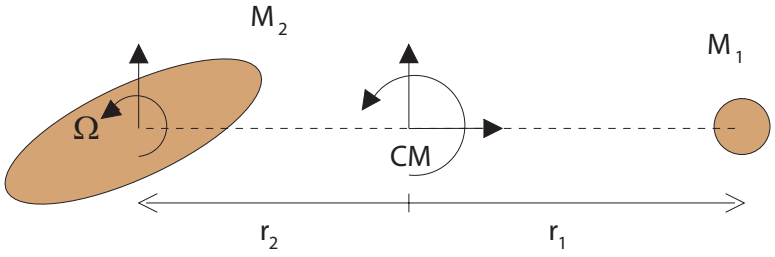

Figure 1.3: Geometry of the Full Two Body Problem for an ellipsoid-sphere system.

astronomical data obtained through observations. The ellipsoid-sphere model is shown in Figure 1.3, where CM is the system's center of mass, and Ω represents the ellipsoid spin which may be different than the mutual orbit rate. In this research, the conditions for equilibrium are further investigated, and perturbations are studied leading to periodic orbits. Results show that the equilibrium states are the minimum energy points of nearby periodic families. Simulations also indicate possible paths from unstable to stable configurations, giving insights on how these binary systems may evolve in time.

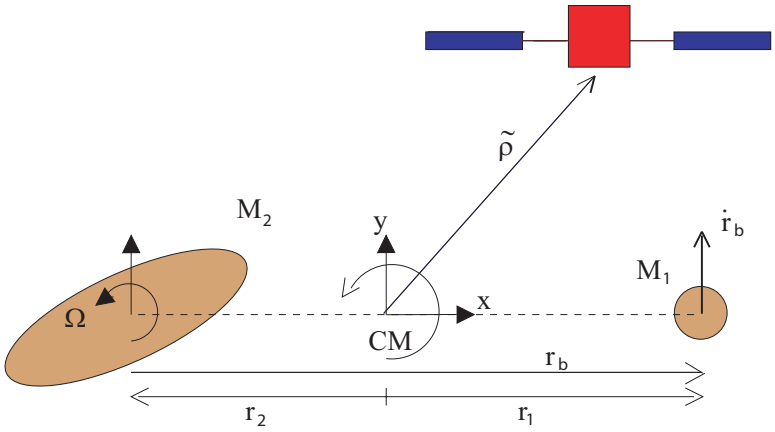

Figure 1.4: The Restricted Full Three-Body Problem

1.2.2 The Restricted Full Three Body Problem

Having defined the dynamics of the F2BP, the problem of binary system orbiters can then be studied. This problem integrates two other classical problems of astrodynamics: the Hill Problem and the Restricted Three Body Problem (see also [85]). The Hill problem studies the dynamics of two mutually orbiting bodies in orbit about a larger mass. The Restricted Three body Problem (R3BP) investigates the dynamics of a massless particle in the gravitational field of two spherical primaries. The Hill problem and the R3BP have been studied extensively [91]. At the limit of having two spherical bodies, the binary system orbiter problem studied here retrieves results from the R3BP. Since the mass distribution is taken into account, the problem is referred to as the Restricted Full Three Body Problem (RF3BP).

Under the ellipsoid-sphere assumption, the RF3BP is shown in Figure 1.4 where $\tilde{\rho}$ is the position of the massless spacecraft with respect to the system's center of mass. For this case, the research looks at the effect of the non-spherical body on the dynamics of particles in this gravitational field by characterizing the equilibrium solutions and their stability, and by developing analytical methods for investigating more general dynamics. At the limit, the results match the R3BP. Investigating the analogue L_1 Lagrangian point, the research also looks at transit paths between the

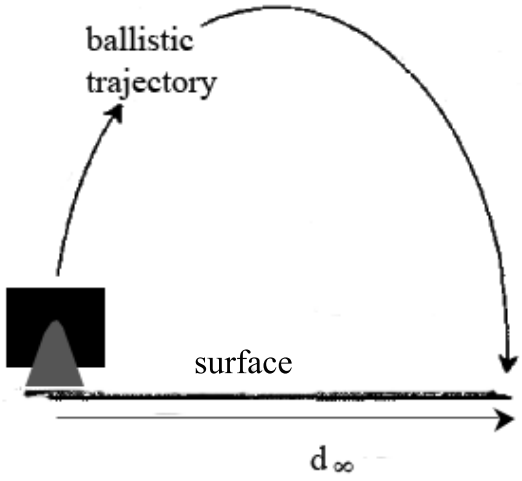

Figure 1.5: Hopping motion on asteroids.

bodies and their associated surface conditions. These transfer paths also exist in the R3BP although the small scale environment of binary asteroids offer a practical and justifiable application of these transits.

1.2.3 Surface Dynamics and Control

Since a non-spherical shape is now included for one of the primaries, surface constraints become important to consider. For scientific investigations, rendezvous missions carrying small landers to small bodies receive an increased interest as landers can perform autonomous tasks on the surface. There is some heritage from previous missions such as the Mars probes, however, wheeled vehicles would be difficult to control and keep track of on an asteroid due to its low gravity environment. One alternative is to use a "hopping" mechanism, as originally designed for the Hayabusa mission. The "hopper", MINERVA, is a good example that uses a torque driving system as the main driver [101, 100]. Ball Aerospace has also designed a spherical robot for studying the surface [89]. A schematic of a hopper motion is drawn in Figure 1.5. Thus, this research looks at the impact dynamics

on asteroids and develops an analytical method to estimate the distance covered and time of travel. Since, the motion takes place on a rotating asteroid, the effect of the rotating asteroid itself is also investigated, where it is shown that the surface dynamics follow the surface equilibria stability of the asteroid.

Then, the next question is how one can control such robot applications on these small bodies. The advantage of hoppers is that they could easily investigate the surface by controlling their initial bounce velocity and orientation from estimating the jumping distance to be covered for a set desired location. Hence, the research looks at control of both single and multiple hoppers to allow a variety of exploration applications. Many control strategies have been considered, especially for rovers, unmanned aerial vehicles and spacecraft formation [2, 27, 94, 66, 92, 3]. Some of them involve leader-follower approaches [28] or string and mesh-stable approaches [90, 66]. Other possible approaches include virtual structures [3, 92] and potential methods [103]. These methods are difficult to implement in the asteroid environment. However, one can modify some of these techniques, such as sliding-mode control method [63, 102], to successfully carry out missions. Therefore, the research develops a first order model for impact dynamics and control of single probes as well as collaborating hoppers.

1.2.4 Mission Design to a Binary Asteroid System

Finally, this research integrates results and findings from the F2BP, the RF3BP, and the surface dynamics in order to develop a mission to a binary asteroid system, taking advantage of the binary system's dynamical features. The proposal uses the binary system 1999 KW4 as a case study, where the bodies can be approximated as a small ellipsoid and a larger sphere. The mission is designed such that the approach to the binary is made through the smallest ellipsoidal body; from an energy consideration, this side of the binary system becomes available first, and,

from astronomical observations, the small body is usually more stable. From an orbiting platform, small landers can be ejected and placed on the surface for further exploration. After hopping to the other side of the small ellipsoidal body, facing the spherical primary, they can then travel across the analogue L_1 Lagrangian point region to reach the massive body using a simple jump. The mission design can also be applied to other accessible binary systems, which is briefly explored in this research.

1.3 Thesis Outline

This dissertation is divided into four main sections. In Chapter 2, the dynamics of two orbiting bodies is first studied, the Two Body Problem (2BP). Since the mass distribution of the bodies is taken into account, it is referred as the Full Two Body Problem (F2BP). In this chapter, both the time-invariant and time-varying problems are investigated. The relative equilibrium configurations are studied and linked to periodic orbits. It is shown that the stable equilibria are the minimum energy state of a periodic family given a value of angular momentum. From these computations, it is also possible to expand on possible evolution scenarios for binary systems.

In Chapter 3, the dynamics of the F2BP is used in the study of the dynamics of a particle, or a spacecraft, in this gravitational field. The problem is called the Restricted Full Three Body Problem (RF3BP). Equilibrium solutions and energy constraints are investigated in order to map the region of motion of a particle in this gravity field. Considering that the bodies have a specific shape, transfer between the bodies may also be allowed under certain conditions, which can lead to natural mass and momentum transfer characteristics of binary systems. The more general problem of non-equilibrium is then studied, especially for periodic orbits near the equilateral Lagrangian points using two different approximation methods.

Motivated by current plans on Near Earth Objects sample return missions,

the dynamics and control of surface exploration hopping robots are modeled and simulated in Chapter 4. A prediction model on the bouncing dynamics is developed to estimate the distance traveled and time to reach a stop. The effect of an asteroid spin and an ellipsoidal gravity field on surface motion is investigated giving a motivation for control of single and multiple collaborating landers.

Finally, Chapter 5 discusses a case study for a mission design to the binary system 1999 KW4 that can take advantage of the particular dynamics of binaries, explaining the different phases from approaching the system to landing on the bodies themselves. The dynamics of the F2BP and of the RF3BP of Chapters 2 and 3 are used, as well as the surface dynamics and control from Chapter 4. Finally, the last section compares the 1999 KW4 system to other available systems in terms of ΔV requirements and surface velocities and constraints.

CHAPTER 2

THE FULL TWO-BODY PROBLEM

2.1 Problem Definition

The study of binary systems constitutes an important field of celestial mechanics and astronomy. Studies have looked at binary systems ranging in size from stars to the small bodies of our solar system. Understanding the dynamics of two orbiting bodies has a fundamental impact on the system evolution and on practical concerns related to spacecraft navigation. We call the situation the Two-Body Problem (2BP) when we look at the translational dynamics of two bodies. When we consider non-spherical mass distributions of these bodies, this problem is referred to as the Full Two-Body Problem (F2BP) and involves coupling between translational and rotational motion. In general, the system has twelve degrees of freedom, which are the position vectors $\boldsymbol{R_1}$ and $\boldsymbol{R_2}$, as shown in Figure 2.1, and the two attitudes of the bodies, $\boldsymbol{A_1}$ and $\boldsymbol{A_2}$. We can combine $\boldsymbol{R_1}$ and $\boldsymbol{R_2}$ into $\boldsymbol{R} = \boldsymbol{R_2} - \boldsymbol{R_1}$, removing three degrees of freedom. An additional three degrees of freedom can be removed by taking the relative attitude $\boldsymbol{A_2}^{\mathrm{T}}\boldsymbol{A_1}$. However, the angular momentum still include both attitudes.

The research from A. Maciejewski and from J.M.A. Danby [53, 15] gives fundamentals of the Full Two Body Problem by discussing systems of a number of extended rigid bodies. They give basic equations of motion, discuss reduction of these systems' parameters, relative equilibria, and mutual potential expressions

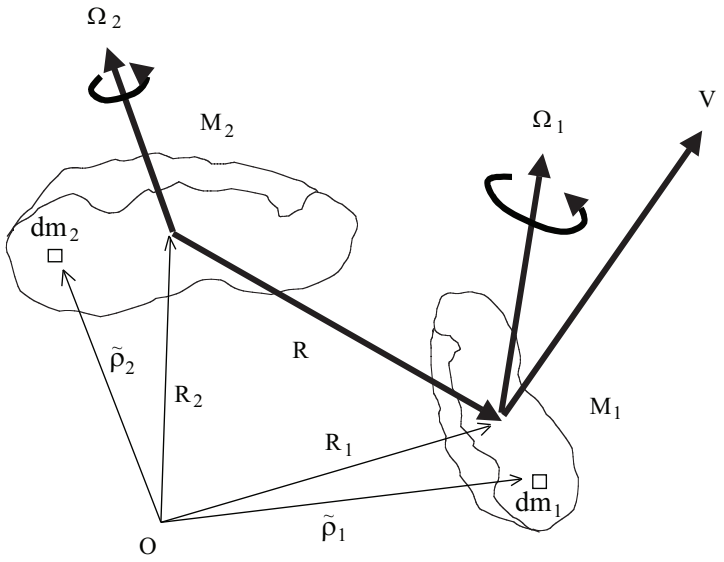

Figure 2.1: Full 2-Body Problem (F2BP) in an inertial frame.

which depend on the shape, mass distribution and orientation of these bodies. As the "full" problem is complex, one can simplify the problem by modeling one of the bodies as a sphere eliminating its attitude dynamics. Conditions for relative equilibria and their stability in the F2BP are derived in [80] for the second body being of arbitrary shape. With the equations of motion written in a frame fixed to the general body, one can also remove three more degrees of freedom from its attitude dynamics. The next sections build up on an ellipsoid-sphere model, first introduced in [79, 84], which keeps interesting dynamical features and has useful symmetry properties.

2.2 Mutual Potential

The mutual potential is an integral over two massive bodies, written as

$$\tilde{U} = -\int_{M_1}\int_{M_2} \frac{G\mathrm{d}m_1\mathrm{d}m_2}{|\tilde{\boldsymbol{\rho}}_\mathbf{1} - \tilde{\boldsymbol{\rho}}_\mathbf{2}|}, \tag{2.1}$$

where G is the universal gravitational constant, M_1 and M_2 represent the two bodies, $\boldsymbol{R_1}$ and $\boldsymbol{R_2}$ represent their position vector from an inertial origin, $\mathrm{d}m_1$ and $\mathrm{d}m_2$ are two mass elements in each body, and $\tilde{\boldsymbol{\rho}}_\mathbf{1}$ and $\tilde{\boldsymbol{\rho}}_\mathbf{2}$ are the position vectors of these two mass elements. The computation of the mutual potential is not trivial in this case. Current and past researches have looked into methods and expressions to compute the mutual potential. In reference [86], the authors have derived polyhedron potential computations to model irregularly shaped bodies. Other methods involve the use of Lie Group computations [52].

The problem is simplified by letting one of the bodies be a sphere while allowing the second body to have a general shape as shown in Figure 2.2. Using this sphere restriction allows one to simplify the computations as the rotational velocities of a sphere are trivial, leaving now nine degrees of freedom, the position vectors $\boldsymbol{R_1}$, $\boldsymbol{R_2}$ shown in Figure 2.2, and the attitude of the general body, $\boldsymbol{A_2}$, but keeping the interesting characteristics from the general body dynamics. Taking the relative dynamics $\boldsymbol{R} = \boldsymbol{R_2} - \boldsymbol{R_1}$ allows to remove three other degrees of freedom. In [15], Danby discusses properties of rigid bodies and potential expressions of some bodies such as a sphere and an ellipsoid, which will be used in later sections.

In the general case of the sphere restriction, $\tilde{U}$ is the mutual potential, defined as

$$\tilde{U} = -GM_1 \int_{M_2} \frac{dm_2}{|\tilde{\boldsymbol{\rho}}_\mathbf{1} - \tilde{\boldsymbol{\rho}}_\mathbf{2}|}, \tag{2.2}$$

where M_1 here is the mass of the sphere and M_2 represents the general body. This problem can be expressed in a few ways depending on the reference frame; in a inertial frame as shown in Figures 2.2 and 2.1, or a rotating frame fixed at the system's center of mass or fixed at one of the bodies. If the frame is fixed to the general body, the mutual potential is time-invariant, which is independent of whether the system is in relative equilibrium or not. Note that it is always possible to transform back to an inertial frame.

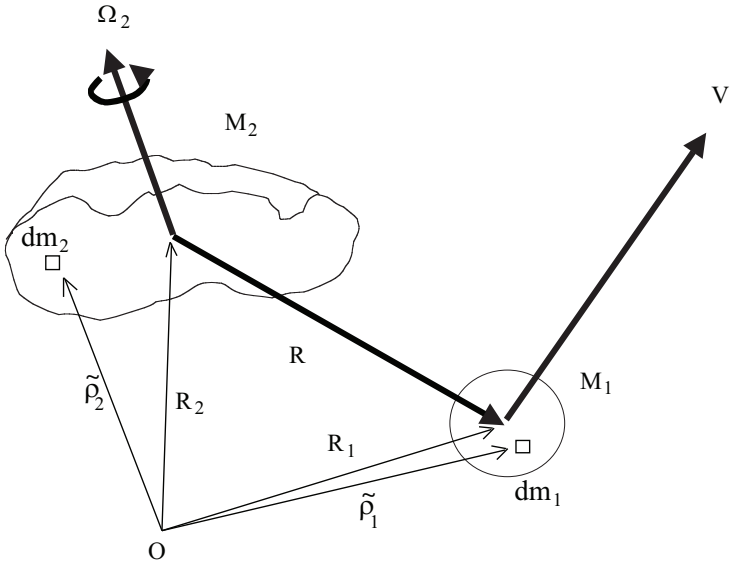

Figure 2.2: Simplified Full Two Body Problem; F2BP under "Sphere Restriction" in the inertial frame.

Hence, for a frame fixed at the center of mass of the non-spherical body,

$$\tilde{U} = -GM_1M_2\hat{U}(\boldsymbol{r_b}), \tag{2.3}$$

where

$$\hat{U} = \frac{1}{M_2}\int_{\beta_2} \frac{dm_2(\tilde{\boldsymbol{\rho}})}{|\boldsymbol{r_b} + \tilde{\boldsymbol{\rho}}|}, \tag{2.4}$$

$\boldsymbol{r_b}$ is the relative position between the sphere and the other body in the body fixed frame, and $\tilde{\boldsymbol{\rho}}$ is the position vector of a mass element of the general body. These parameters are shown in Figure 2.3. Note that $\hat{U}$ is a point mass potential that has been normalized. Previous work has investigated the equations of motion of a binary system, mostly describing conditions for equilibrium configurations of a system composed of a sphere and a general body, and the stability conditions of these equilibria [80].

A general method of approximation is to express the general body potential using spherical harmonics [45], which simplifies if the coordinate frame is along the

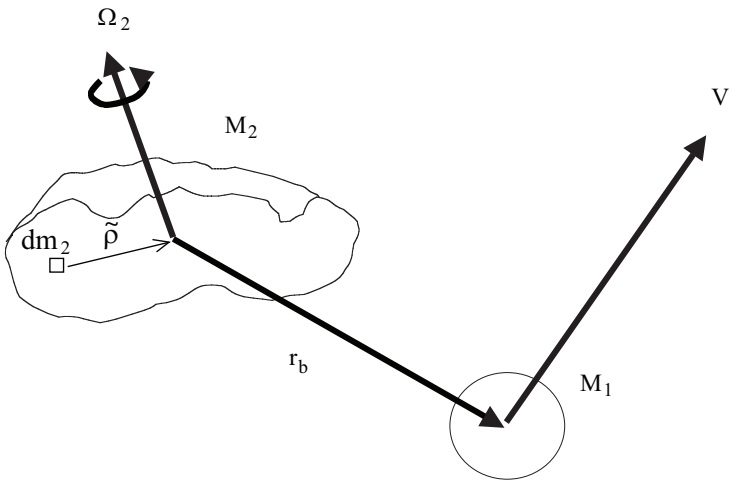

Figure 2.3: F2BP under "Sphere Restriction" with parameters expressed in the general body fixed frame.

principal moments of inertia of the general body. It is usually expressed in the form

$$\tilde{U} = \sum_{l=0}^{\infty}\sum_{m=0}^{l}\left(\frac{R_0}{r}\right)^l P_{lm}\sin\delta\left(C_{lm}\cos(m\lambda) + S_{lm}\sin(m\lambda)\right), \tag{2.5}$$

where the P'_{lm}s are associated Legendre functions and the C'_{lm}s and S'_{lm}s are the spherical harmonics coefficients, and where δ and λ are the usual spherical coordinates of latitude and longitude in the general body. This model will be used in a later chapter. However, a closed form for the mutual potential would be more convenient to work with.

An ellipsoid-sphere system has also been studied in [84, 79], investigating relative equilibria and stability. As described in [15], the potential of an ellipsoid can be written in terms of elliptic integrals. The exterior potential of an ellipsoid with sides α, β, γ and uniform density ρ, is expressed as

$$\tilde{U} = G\rho\alpha\beta\gamma\int_{\lambda}^{\infty}\left(1 - \frac{x^2}{\alpha^2+v} - \frac{y^2}{\beta^2+v} - \frac{z^2}{\gamma^2+v}\right)\frac{dv}{\Delta(v)}, \tag{2.6}$$

where

$$\Delta(v) = \sqrt{(\alpha^2+v)(\beta^2+v)(\gamma^2+v)}, \tag{2.7}$$

$0 < \gamma \leq \beta \leq \alpha$, γ and β correspond to the z and y semi-axes of the ellipsoid, and λ satisfies

$$\left(1 - \frac{x^2}{\alpha^2 + \lambda} - \frac{y^2}{\beta^2 + \lambda} - \frac{z^2}{\gamma^2 + \lambda}\right) = 0. \tag{2.8}$$

Because of the symmetry properties of the ellipsoid, and the closed form expression for the potential, in the current work, the dynamics of an ellipsoid-sphere system is studied in more detail and used as a base for modeling the dynamics of particles in the gravity field of a binary system.

2.3 Equations of Motion

Defining a rotating coordinate system in the frame fixed to the general body allows us to discard its attitude dynamics from the equations of motion; in this frame the mutual potential is time-invariant. The ellipsoid was chosen for its symmetry properties and its closed form potential energy expression. The geometry of the problem is represented in Figure 2.4. The system is defined as M_1 and M_2 for the sphere and the ellipsoid, respectively, and the relative distance from the bodies' center of mass is $\boldsymbol{r_b}$. The two bodies orbit about their center of mass indicated as "CM" on Figure 2.4. If the mass ratio is defined as

$$\nu = \frac{M_1}{M_1 + M_2}, \tag{2.9}$$

then, relative to their center of mass, they each orbit at,

$$\boldsymbol{r_1} = (1 - \nu)\boldsymbol{r_b} \tag{2.10}$$

and

$$\boldsymbol{r_2} = -\nu \boldsymbol{r_b}. \tag{2.11}$$

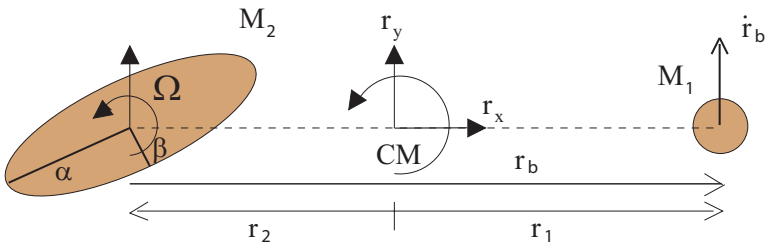

Figure 2.4: Geometry of the Full Two Body Problem for an ellipsoid-sphere system.

In this frame, the two bodies' relative dynamics are defined by

$$\ddot{\boldsymbol{r_b}} + 2\boldsymbol{\Omega} \times \dot{\boldsymbol{r_b}} + \dot{\boldsymbol{\Omega}} \times \boldsymbol{r_b} + \boldsymbol{\Omega} \times (\boldsymbol{\Omega} \times \boldsymbol{r_b}) = G(M_1 + M_2)\frac{\partial \hat{U}}{\partial \boldsymbol{r_b}} \tag{2.12}$$

and the rotational dynamics of the ellipsoid are described by

$$\hat{\boldsymbol{I}} \cdot \dot{\boldsymbol{\Omega}} + \boldsymbol{\Omega} \times \hat{\boldsymbol{I}} \cdot \boldsymbol{\Omega} = -GM_1 \boldsymbol{r_b} \times \frac{\partial \hat{U}}{\partial \boldsymbol{r_b}}, \tag{2.13}$$

where $\boldsymbol{\Omega}$ is the angular velocity of the ellipsoid and $\hat{\boldsymbol{I}}$ is its inertia matrix [77]. Note that Eq. (2.12) is defined for any non-spherical body in general with the mutual potential expressed in Eqs. (2.3,2.4) [79].

To simplify the computation, the maximum radius of the ellipsoid, α, and the mean orbital motion of the system at this radius, $n = \sqrt{G(M_1 + M_2)/\alpha^3}$ from relative motion in the point mass two-body problem [72], are chosen as length and time scales, respectively. The normalized distance between the two bodies and angular velocity of the ellipsoid are expressed as

$$\boldsymbol{r} = \frac{\boldsymbol{r_b}}{\alpha} \tag{2.14}$$

and

$$\boldsymbol{\omega} = \frac{\boldsymbol{\Omega}}{n}. \tag{2.15}$$

Let $\boldsymbol{r} = r_x\hat{\imath} + r_y\hat{\jmath} + r_z\hat{k}$. As derived in [77], the Lagrangian form of the F2BP

dynamics can be written as follows,

$$\ddot{\boldsymbol{r}} + 2\boldsymbol{\omega} \times \dot{\boldsymbol{r}} + \dot{\boldsymbol{\omega}} \times \boldsymbol{r} + \boldsymbol{\omega} \times (\boldsymbol{\omega} \times \boldsymbol{r}) = \frac{\partial U}{\partial \boldsymbol{r}} \tag{2.16}$$

and

$$\boldsymbol{I} \cdot \dot{\boldsymbol{\omega}} + \boldsymbol{\omega} \times \boldsymbol{I} \cdot \boldsymbol{\omega} = -\nu \boldsymbol{r} \times \frac{\partial U}{\partial \boldsymbol{r}}. \tag{2.17}$$

For the ellipsoid, the normalization above is used to express the potential as

$$U = \frac{3}{4} \int_{\lambda}^{\infty} \phi(\boldsymbol{r}, v) \frac{dv}{\Delta(v)} \tag{2.18}$$

with

$$\phi(\boldsymbol{r}, v) = 1 - \frac{r_x^2}{1+v} - \frac{r_y^2}{\beta^2+v} - \frac{r_z^2}{\gamma^2+v} \tag{2.19}$$

and

$$\Delta(v) = \sqrt{(1+v)(\beta^2+v)(\gamma^2+v)}, \tag{2.20}$$

where $0 < \gamma \leq \beta \leq 1$, γ and β correspond to the z and y semi-axes of the ellipsoid, and λ satisfies $\phi(\boldsymbol{r}, \lambda) = 0$. The normalized principal moments of inertia are $I_{xx} = \frac{1}{5}(\beta^2 + \gamma^2)$, $I_{yy} = \frac{1}{5}(1 + \gamma^2)$, and $I_{zz} = \frac{1}{5}(1 + \beta^2)$. In the $\hat{\imath} - \hat{\jmath} - \hat{k}$ frame, Eqs. (2.16-2.17) become

$$\dot{\omega} = -\frac{\nu}{I_{zz}} \left(r_x \frac{\partial U}{\partial r_y} - r_y \frac{\partial U}{\partial r_x} \right), \tag{2.21}$$

$$\ddot{r_x} = \omega^2 r_x + 2\omega \dot{r_y} + \dot{\omega} r_y + \frac{\partial U}{\partial r_x}, \tag{2.22}$$

$$\ddot{r_y} = \omega^2 r_y - 2\omega \dot{r_x} - \dot{\omega} r_x + \frac{\partial U}{\partial r_y}, \tag{2.23}$$

and

$$\ddot{r_z} = \frac{\partial U}{\partial r_z}, \tag{2.24}$$

where U is given by Eqs. (2.18-2.20).

Although general motion can be studied, with the Coriolis and centripetal accelerations acting in the plane, the planar problem is a rich problem to study. When considering planar motion, the ellipsoid-sphere model also allows to write the

problem as a two degree of freedom Hamiltonian system. The position of the sphere relative to the ellipsoid in the plane is denoted as $\boldsymbol{q} = \boldsymbol{r}$, and the inertial velocity is, $\boldsymbol{p} = \dot{\boldsymbol{r}} + \boldsymbol{\omega} \times \boldsymbol{r}$. Using this set of coordinates, the energy and momentum integrals in normalized units can be written as

$$E = \frac{1}{2}\boldsymbol{p} \cdot \boldsymbol{p} + \frac{1}{2\nu} I_{zz}\omega^2 - U(\boldsymbol{q}) \tag{2.25}$$

and

$$K = \frac{1}{\nu} I_{zz}\omega + \hat{\boldsymbol{z}} \cdot (\boldsymbol{q} \times \boldsymbol{p}). \tag{2.26}$$

The rotation rate ω can be solved as function of K, $\boldsymbol{q}$ and $\boldsymbol{p}$, which gives

$$\omega = \frac{\nu}{I_{zz}} \left[K - \hat{\boldsymbol{z}} \cdot (\boldsymbol{q} \times \boldsymbol{p}) \right]. \tag{2.27}$$

Hence, for given values of K, $\boldsymbol{q}$ and $\boldsymbol{p}$, ω can be substituted for into the energy equation, Eq. (2.25),

$$E = \frac{1}{2}\boldsymbol{p} \cdot \boldsymbol{p} + \frac{\nu}{2I_{zz}} \left[K - \hat{\boldsymbol{z}} \cdot (\boldsymbol{q} \times \boldsymbol{p}) \right]^2 - U(\boldsymbol{q}). \tag{2.28}$$

Note that, in this case, the energy integral is the Hamiltonian, or $E = H(\boldsymbol{q}, \boldsymbol{p})$ with angular momentum K as a free parameter. For general three dimensional motion the angular momentum cannot be eliminated in the same way for the Hamiltonian form of the equations, as its elimination would couple the relative attitude of the body into the energy [80].

In explicit form for planar motion, Eq. (2.28) becomes

$$H(\boldsymbol{q}, \boldsymbol{p}) = \frac{1}{2}\boldsymbol{p} \cdot \boldsymbol{p} + \frac{\nu}{2I_{zz}} \left[K - \hat{\boldsymbol{z}} \cdot (\boldsymbol{q} \times \boldsymbol{p}) \right]^2 - U(\boldsymbol{q}). \tag{2.29}$$

Then, the dynamics can be computed from

$$\dot{\boldsymbol{q}} = H_p \tag{2.30}$$

and

$$\dot{\boldsymbol{p}} = -H_q, \tag{2.31}$$

or, in components,

$$\dot{q_x} = H_{p_x} = p_x + q_y \frac{\nu}{I_{zz}} \left[K - (q_x p_y - p_x q_y)\right], \tag{2.32}$$

$$\dot{q_y} = H_{p_y} = p_y - q_x \frac{\nu}{I_{zz}} \left[K - (q_x p_y - p_x q_y)\right], \tag{2.33}$$

$$\dot{p_x} = -H_{q_x} = p_y \frac{\nu}{I_{zz}} \left[K - (q_x p_y - p_x q_y)\right] + \frac{\partial U}{\partial q_x}, \tag{2.34}$$

and

$$\dot{p_y} = -H_{q_y} = -p_x \frac{\nu}{I_{zz}} \left[K - (q_x p_y - p_x q_y)\right] + \frac{\partial U}{\partial q_y}, \tag{2.35}$$

where the subscripts denote partial differentiation.

The first order derivatives of the ellipsoid potential were given by [79],

$$\frac{\partial U}{\partial q_x} = \frac{\partial U}{\partial r_x} = U_x = -\frac{3}{2} q_x \int_\lambda^\infty \frac{du}{(u+1)\triangle(u)}, \tag{2.36}$$

$$\frac{\partial U}{\partial q_y} = \frac{\partial U}{\partial r_y} = U_y = -\frac{3}{2} q_y \int_\lambda^\infty \frac{du}{(u+\beta^2)\triangle(u)}, \tag{2.37}$$

and

$$\frac{\partial U}{\partial q_z} = \frac{\partial U}{\partial r_z} = U_z = -\frac{3}{2} q_z \int_\lambda^\infty \frac{du}{(u+\gamma^2)\triangle(u)}. \tag{2.38}$$

Using the substitution $v = u + \lambda$, these derivatives can be solved using Carlson's standard integrals of the third kind. The algorithm wa taken from [19], giving the following expression for the three axis of the ellipsoid, α, β, and γ,

$$R_{j\alpha} = \frac{3}{2} \int_0^\infty \frac{du}{(u+\lambda+1)\triangle(u+\lambda)}, \tag{2.39}$$

$$R_{j\beta} = \frac{3}{2} \int_0^\infty \frac{du}{(u+\lambda+\beta^2)\triangle(u+\lambda)}, \tag{2.40}$$

$$R_{j\gamma} = \frac{3}{2} \int_0^\infty \frac{du}{(u+\lambda+\gamma^2)\triangle(u+\lambda)}, \tag{2.41}$$

and, the elliptic integral of the first kind is used to write the potential,

$$R_{j0} = \frac{1}{2}\int_0^\infty \frac{du}{\triangle(u+\lambda)}, \tag{2.42}$$

Therefore, using the notation above, the mutual potential is expressed as

$$U = \frac{3}{2}R_{j0} - \frac{1}{2}\left[q_x^2 R_{j\alpha} + q_y^2 R_{j\beta} + q_z^2 R_{j\gamma}\right], \tag{2.43}$$

and the first derivatives are expressed as,

$$U_x = -q_x R_{j\alpha}, \tag{2.44}$$

$$U_y = -q_y R_{j\beta}, \tag{2.45}$$

and

$$U_z = -q_z R_{j\gamma}. \tag{2.46}$$

2.4 Relative Equilibria of an Ellipsoid-Sphere System

A particular solution of the F2BP is for the two bodies to be in relative equilibrium. Relative equilibrium conditions are found by setting all velocities and accelerations to zero in Eqs. (2.16-2.17). Equation (2.16) shows that the gravitational acceleration must be perpendicular to the spin axis. Also, with the current symmetry assumption on the gravitational potential, the position and gravitational acceleration have to be parallel. With this constraint, Eq.(2.17) is satisfied if the ellipsoid spins about one of its other principal axes. Note that the spin is parallel to the inertia vector and it is independent of the principal axis the ellipsoid is rotating about [79, 84].

Hence, relative equilibria exist when one of the principal axes of the ellipsoid is pointed at the sphere. Then, as a general expression, given a solution along the "q" axis, from Eq.(2.16) and using Eqs. (2.18-2.20) due to the ellipsoid, the spin rate is

expressed as,

$$\omega^2 = \frac{3}{2}\int_{\lambda}^{\infty} \frac{dv}{({\alpha_q}^2 + v)\triangle(v)}. \tag{2.47}$$

For the present problem, α_q represents the ellipsoid radius along which the sphere is located. Note that here $\lambda = r^2 - {\alpha_q}^2$, where q is the distance between the primaries at a relative equilibrium, $q = \boldsymbol{r}$. Also note that for a general mass distributions, relative equilibria will not necessarily be along a principal axis. A more complete discussion can be found in [80].

For the case of an ellipsoid-sphere system, two configurations exist: with the minimum moment of inertia aligned with the axis joining the two bodies and where it is perpendicular to it. The two cases are shown in Figure 2.5. In the case of the short-axis configuration, the maximum radius of the ellipsoid, α, is aligned with the y-axis. Hence, from this perpendicular assumption, the R_j expressions to be used in this case are,

$$R_{j\alpha} = \frac{3}{2}\int_{0}^{\infty} \frac{du}{(u + \lambda + \beta^2)\triangle(u + \lambda)}, \tag{2.48}$$

$$R_{j\beta} = \frac{3}{2}\int_{0}^{\infty} \frac{du}{(u + \lambda + 1)\triangle(u + \lambda)}, \tag{2.49}$$

and

$$R_{j\gamma} = \frac{3}{2}\int_{0}^{\infty} \frac{du}{(u + \lambda + \gamma^2)\triangle(u + \lambda)}. \tag{2.50}$$

Note that for $\nu \approx 0$, the case of a point mass orbiting a general body is retrieved, in which solving for the equilibria gives rotations about the principal axes of inertia of the rigid body. The long-axis configuration in this case is always unstable. Now, on the other hand, $\nu \approx 1$ indicates a general body orbiting a point mass. In this case, the long-axis solution is stable whereas short-axis solutions are always unstable. In the present work, the long-axis case is usually the only one considered as only it can have energetically stable solutions [79], hence being more commonly found in space [30, 71, 96].

Now, for convenience, consider the Hamiltonian system as defined by Eqs.

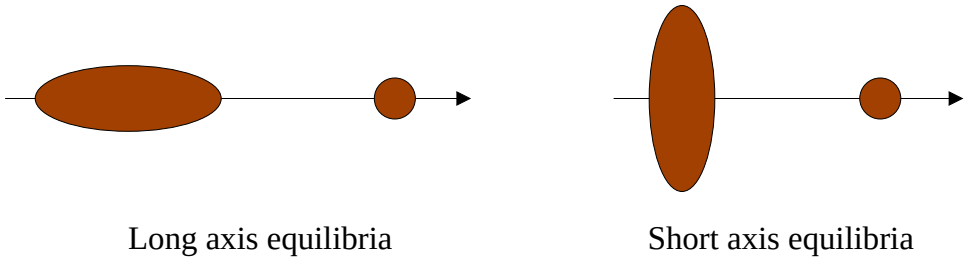

Figure 2.5: Configurations investigated for the Full Two-Body Problem

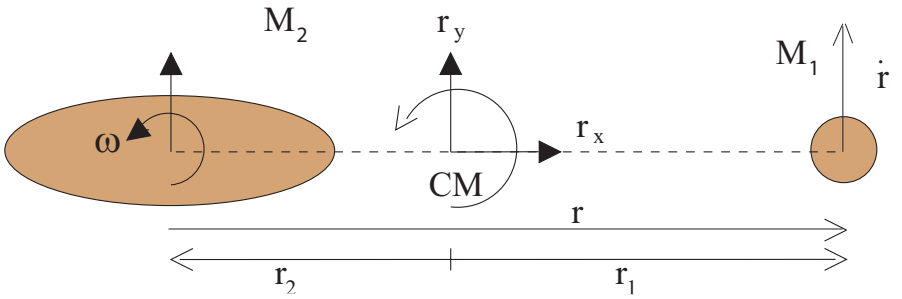

Figure 2.6: Geometry of the Full Two Body Problem under relative equilibrium. The system maintains this same configuration at all time, and the orbit rate is solved from Eq. (2.47).

(2.32-2.35), in which all time derivatives are zero, and where the two bodies are in equilibrium configuration, aligned along the x-axis, as pictured in Figure 2.6.

The solutions are given by

$$\boldsymbol{q} = [q, 0]^T \tag{2.51}$$

and

$$\boldsymbol{p} = [0, p]^T. \tag{2.52}$$

Note that the first derivatives of the mutual potential at a relative equilibrium gives

$$U_{q_x} = -q_x R_{j\alpha} = -qR_{j\alpha} = -qI(q), \tag{2.53}$$

$$U_{q_y} = 0, \tag{2.54}$$

and

$$U_{q_z} = 0. \tag{2.55}$$

Solving for q with $\dot{\boldsymbol{q}} = \dot{\boldsymbol{p}} = 0$ in Eqs. (2.33-2.34) gives

$$1 = \frac{\nu q}{I_{zz} p} \left[K - qp \right] \tag{2.56}$$

and

$$I(q) = \frac{\nu p}{I_{zz} q} \left[K - qp \right]. \tag{2.57}$$

Note that $\hat{\boldsymbol{z}} \cdot (\boldsymbol{q} \times \boldsymbol{p}) = qp$. From Eq. (2.56), the inertial velocity component p, is expressed as

$$p = \frac{(\nu q K / I_{zz})}{(1 + \nu q^2 / I_{zz})}, \tag{2.58}$$

and substituting p in Eq. (2.57) gives

$$I(q) = \frac{(\nu K / I_{zz})^2}{(1 + \nu q^2 / I_{zz})^2}. \tag{2.59}$$

Given values of angular momentum, mass ratio and ellipsoidal parameters, the possible distances between the bodies, q, for which the system is in relative equilibrium can be solved for. As a binary system will most likely lose energy through internal dissipation and conserve angular momentum (see [87] for a case study of 1999 KW4 or [55] for a more general discussion), it is of interest to study its dynamics under constant angular momentum. For a given value of angular momentum and a value for the system mass ratio in Eq. (2.59), one can solve for at most two relative equilibria, as shown by the C-shaped curve, or Locus of solutions, in Figure 2.7. Note that having a more pronounced ellipsoid flattened this C curve. There is one single solution, or bifurcation value, at the mass ratio, ν^*, and solution q^*, which is at the left end of the locus of solutions in Figure 2.7. For $\nu > \nu^*$, the system has two relative equilibrium solutions, one stable and one unstable, as described in the next section.

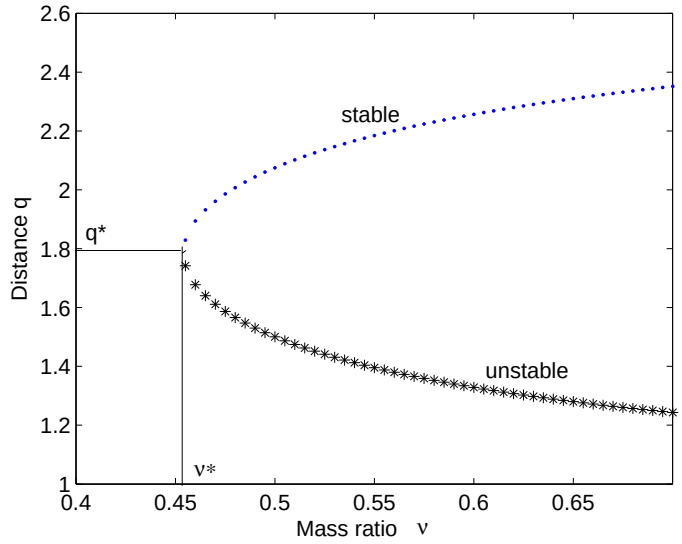

Figure 2.7: Locus of solutions q as function of the mass ratio, for a constant angular momentum. The upper and lower branches represent stable and unstable solutions, respectively. The system angular momentum is K=1.715 (nondimensional), and ellipsoidal parameters are $\beta = 0.5$ and $\gamma = 0.25$.

2.4.1 Stability of Relative Equilibria

Stability of relative equilibria is composed of two parts, spectral stability and energetic stability. Spectral stability is related to the system eigenvalues associated to an equilibrium solution while energetic stability is derived from the system's energy state. A system is energetically stable if there is no state at the same angular momentum with a lower energy value.

As mentioned in the previous section, in general it is possible to find two solutions for given values of angular momentum, mass ratio and ellipsoidal parameters. There is always one stable and one unstable solution, and we find that the spectral stability is tied with the energetic stability.

The conditions for spectral stability of a relative equilibrium of the F2BP were derived in [79]. In this case, for the planar problem, it is more convenient to write them in terms of the Hamiltonian form of the equations of motion.

Given Eqs. (2.32-2.35), a small perturbation to the nominal path is

$$\begin{bmatrix} \boldsymbol{\delta\dot{q}} \\ \boldsymbol{\delta\dot{p}} \end{bmatrix} = JH_{xx} \begin{bmatrix} \boldsymbol{\delta q} \\ \boldsymbol{\delta p} \end{bmatrix}, \tag{2.60}$$

where J has the form

$$J = \begin{bmatrix} 0_{2\times2} & I_{2\times2} \\ -I_{2\times2} & 0_{2\times2} \end{bmatrix}, \tag{2.61}$$

and $0_{2\times2}$ and $I_{2\times2}$ are the 2×2 zero and identity matrix, respectively.

For an ellipsoid-sphere, Eq.(2.60) can be used where H_{xx} represents the second derivatives of the Hamiltonian defined by Eq. (2.29),

$$H_{xx} = \begin{bmatrix} -\sigma\omega^2 + U_{q_xq_x} & 0 & 0 & \omega(1-\sigma) \\ 0 & U_{q_yq_y} & -\omega & 0 \\ 0 & -\omega & -1 & 0 \\ \omega(1-\sigma) & 0 & 0 & -(1+\sigma) \end{bmatrix}. \tag{2.62}$$

In these expressions, $\sigma = \nu {q_x}^2/I_{zz}$, and $\omega = \frac{(\nu K/I_{zz})}{(1+\sigma)} = \sqrt{I(q)}$, where $I(q)$ is given by Eq.(2.53).

The characteristic equation of JH_{xx} is found to be

$$\zeta^4 + a\zeta^2 + b = 0, \tag{2.63}$$

where

$$a = 2\omega^2(1-\sigma) + B - (1+\sigma)U_{q_yq_y}, \tag{2.64}$$

$$b = \omega^2(1-\sigma)^2(U_{q_yq_y} + \omega^2) - B(U_{q_yq_y} + \omega^2)(1+\sigma), \tag{2.65}$$

and $B = \sigma\omega^2 - U_{q_xq_x}$. For stability to hold, the conditions to satisfy are

$$a > 0, \tag{2.66}$$

$$b > 0, \tag{2.67}$$

and

$$a^2 - 4b > 0. \tag{2.68}$$

In the case of a stable equilibrium solution, the system only has a center manifold and two sets of imaginary eigenvalues can be computed. For an eigenvalue of the type $\zeta = \pm i\lambda$, the period of oscillation is computed using

$$T = \frac{2\pi}{\lambda}. \tag{2.69}$$

Hence, each stable solution has two frequencies associated with it.

An unstable solution will have one pair of imaginary and one pair of real eigenvalues. The real eigenvalues are associated with a hyperbolic manifold which make the solution unstable. Note that it is still possible to obtain the associated frequency of oscillation for the system. Reference [79] provides a more detailed derivation of these stability conditions.

Stability of a dynamical system can also be defined from its energy evaluation. In [80], the energetic stability conditions are derived for a general gravity field in the F2BP under constant angular momentum assumption. This corresponds to nonlinear stability. For energetic stability of the equilibrium states, one needs to investigate the second variation of the energy functional, which can be written in the following form

$$d^2H = d\boldsymbol{x} \cdot H_{xx} \cdot d\boldsymbol{x} > 0, \tag{2.70}$$

where H_{xx} is the matrix of the second derivatives of the Hamiltonian, and the $d\boldsymbol{x}$ are chosen arbitrarily. Thus the condition is that H_{xx} be positive definite.

The energetic stability conditions are found from Eq.(2.70) using the eigenvalues of H_{xx}. The characteristic equation is then

$$\eta^4 + \alpha_3\eta^3 + \alpha_2\eta^2 + \alpha_1\eta + \alpha_0 = 0, \tag{2.71}$$

where the coefficients are expressed as

$$\alpha_3 = \left(U_{q_yq_y} - 2 - \sigma - B\right), \tag{2.72}$$

$$\alpha_2 = B\left(-U_{q_yq_y} + (2+\sigma)\right) + 1 + \sigma - U_{q_yq_y}(2+\sigma) - \omega^2 - \omega^2(1-\sigma)^2, \tag{2.73}$$

$$\alpha_1 = B\left(U_{q_yq_y}(2+\sigma) + \omega^2 - (1+\sigma)\right) + \omega^2(-U_{q_yq_y}+1)(1-\sigma)^2 + (U_{q_yq_y}+\omega^2)(1+\sigma), \tag{2.74}$$

$$\alpha_0 = -B(U_{q_yq_y}+\omega^2)(1+\sigma) + \omega^2(U_{q_yq_y}+\omega^2)(1-\sigma)^2, \tag{2.75}$$

and $B = \sigma\omega^2 - U_{q_xq_x}$. Note that all the second order partial derivatives should be evaluated at the equilibrium points when investigating stability. When the system is in relative equilibrium, $U_{q_xq_x}$ and $U_{q_yq_y}$ are given by

$$U_{q_xq_x} = R_{j\beta} + R_{j\gamma} \tag{2.76}$$

and

$$U_{q_yq_y} = -R_{j\beta}. \tag{2.77}$$

For a system to be stable, the real part of the eigenvalues all need to be positive. In this case, the energy is at a local minimum and the system cannot decrease its energy without decreasing its angular momentum. The Routh criteria can be applied to find analytical conditions for energetic stability. The Routh criteria states that all roots of a polynomial of degree 4 have negative real parts if

$$\alpha_3 > 0, \tag{2.78}$$

$$\alpha_3\alpha_2 - \alpha_1 > 0, \tag{2.79}$$

$$\alpha_2\alpha_1 - \alpha_0\alpha_3 > 0, \tag{2.80}$$

$$\alpha_0 > 0. \tag{2.81}$$

There exists a relation that links the spectral and the energetic stability in the F2BP. By comparing Eq. (2.63) and Eq. (2.71), it is clear that the expression for b

and α_0 are equivalent. Also, it is found that spectral stability is lost as b transitions from $b > 0$ to $b < 0$. When the F2BP becomes spectrally unstable, $\alpha_0 < 0$, which places one root of Eq. (2.71) in the left half plane. Hence, the system also becomes energetically unstable since H_{xx} needs to be positive definite for stability. Conversely, when the system is spectrally stable it is energetically stable for the assumed configuration.

Figure 2.8 shows the corresponding energy of the relative equilibria under constant angular momentum, shown in Figure 2.7. For a given mass ratio, the two solutions don't have the same stability properties; they are either spectrally and energetically stable or unstable. The lower branch of Figure 2.8 corresponding to the upper branch of Figure 2.7 are stable points. Hence, closer relative equilibria are unstable and associated with a larger energy than the more distant relative equilibria, which are stable. For a system dissipating energy due to external perturbations, it could easily transition from a closer unstable configuration to a more distant stable one. Note that the stability of the bifurcation point is indeterminate.

The second order derivatives of U_e have the form,

$$U_{q_xq_x} = -\frac{3}{2}\int_\lambda^\infty \frac{du}{(u+1)\triangle(u)} + \frac{3{q_x}^2}{(1+\lambda)^2\triangle(\lambda)}C_L, \tag{2.82}$$

$$U_{q_yq_y} = -\frac{3}{2}\int_\lambda^\infty \frac{du}{(u+\beta^2)\triangle(u)} + \frac{3{q_y}^2}{(\beta^2+\lambda)^2\triangle(\lambda)}C_L, \tag{2.83}$$

$$U_{q_zq_z} = -\frac{3}{2}\int_\lambda^\infty \frac{du}{(u+\gamma^2)\triangle(u)} + \frac{3{q_z}^2}{(\gamma^2+\lambda)^2\triangle(\lambda)}C_L, \tag{2.84}$$

$$U_{q_xq_y} = \frac{3q_xq_y}{(1+\lambda)(\beta^2+\lambda)\triangle(\lambda)}C_L, \tag{2.85}$$

$$U_{q_xq_z} = \frac{3q_xq_z}{(1+\lambda)(\gamma^2+\lambda)\triangle(\lambda)}C_L, \tag{2.86}$$

and

$$U_{q_yq_z} = \frac{3q_yq_z}{(\gamma^2+\lambda)(\beta^2+\lambda)\triangle(\lambda)}C_L. \tag{2.87}$$

For the long-axis configuration, the second derivatives of the potential can be

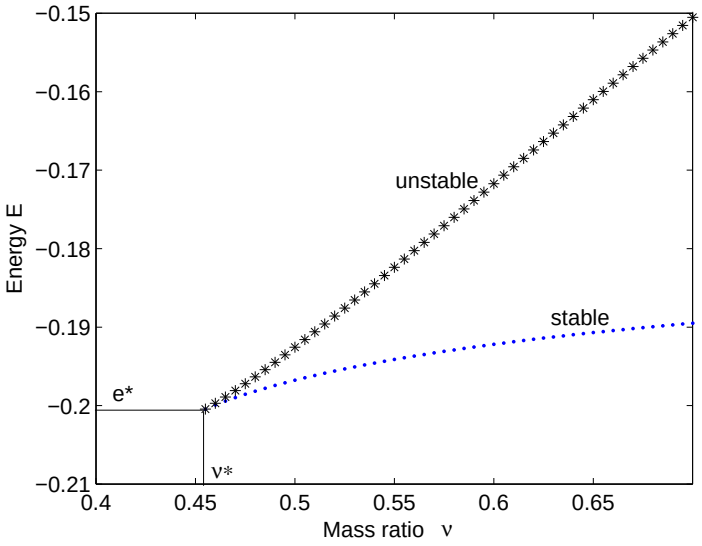

Figure 2.8: Energy plot of relative equilibrium solutions as function of the mass ratio ν, with constant angular momentum. The lower and upper branches represent unstable and stable solutions, respectively. The system angular momentum is K=1.715 (using the normalization introduced in section 2.3), and ellipsoidal shape parameters are $\beta = 0.5$ and $\gamma = 0.25$.

expressed as follows,

$$U_{q_xq_x} = -R_{j\alpha} + \frac{q_x^2}{(1+\lambda)^2}(R_{j\alpha} + R_{j\beta} + R_{j\gamma})C_L, \tag{2.88}$$

$$U_{q_yq_y} = -R_{j\beta} + \frac{q_y^2}{(\beta^2+\lambda)^2}(R_{j\alpha} + R_{j\beta} + R_{j\gamma})C_L, \tag{2.89}$$

$$U_{q_zq_z} = -R_{j\gamma} + \frac{q_z^2}{(\gamma^2+\lambda)^2}(R_{j\alpha} + R_{j\beta} + R_{j\gamma})C_L, \tag{2.90}$$

$$U_{q_xq_y} = \frac{q_xq_y}{(1+\lambda)(\beta^2+\lambda)}(R_{j\alpha} + R_{j\beta} + R_{j\gamma})C_L, \tag{2.91}$$

$$U_{q_xq_z} = \frac{q_xq_z}{(1+\lambda)(\gamma^2+\lambda)}(R_{j\alpha} + R_{j\beta} + R_{j\gamma})C_L, \tag{2.92}$$

and

$$U_{q_yq_z} = \frac{q_yq_z}{(\beta^2+\lambda)(\gamma^2+\lambda)}(R_{j\alpha} + R_{j\beta} + R_{j\gamma})C_L, \tag{2.93}$$

where $C_L = \left[\frac{1}{\frac{q_x^2}{(1+\lambda)^2} + \frac{q_y^2}{(\beta^2+\lambda)^2} + \frac{q_z^2}{(\gamma^2+\lambda)^2}}\right]$

For the short-axis configuration, the second derivatives now become,

$$U_{q_xq_x} = -R_{j\alpha} + \frac{q_x^2}{(\beta^2+\lambda)^2}(R_{j\alpha} + R_{j\beta} + R_{j\gamma})C_S, \tag{2.94}$$

$$U_{q_yq_y} = -R_{j\beta} + \frac{q_y^2}{(1+\lambda)^2}(R_{j\alpha} + R_{j\beta} + R_{j\gamma})C_S, \tag{2.95}$$

$$U_{q_zq_z} = -R_{j\gamma} + \frac{q_z^2}{(\gamma^2+\lambda)^2}(R_{j\alpha} + R_{j\beta} + R_{j\gamma})C_S, \tag{2.96}$$

$$U_{q_xq_y} = \frac{q_xq_y}{(1+\lambda)(\beta^2+\lambda)}(R_{j\alpha} + R_{j\beta} + R_{j\gamma})C_S, \tag{2.97}$$

$$U_{q_xq_z} = \frac{q_xq_z}{(\beta^2+\lambda)(\gamma^2+\lambda)}(R_{j\alpha} + R_{j\beta} + R_{j\gamma})C_S, \tag{2.98}$$

and

$$U_{q_yq_z} = \frac{q_yq_z}{(1+\lambda)(\gamma^2+\lambda)}(R_{j\alpha} + R_{j\beta} + R_{j\gamma})C_S, \tag{2.99}$$

where $C_S = \left[\frac{1}{\frac{q_x^2}{(\beta^2+\lambda)^2}+\frac{q_y^2}{(1+\lambda)^2}+\frac{q_z^2}{(\gamma^2+\lambda)^2}}\right]$

2.4.2 Energy vs Stability at a Relative Equilibrium

A binary system can be at a relative equilibrium solution associated with a positive energy or not. For this application, the energy is the Hamiltonian given by Eq. (2.29). For positive energy, the equilibria are found to always be unstable. Furthermore, a positive total energy indicates that the system can disrupt under its mutual dynamics [78]. For negative energy, the system is bound and the solutions can be stable or unstable.

Figure 2.8 showed clearly that a system in the closer equilibrium configuration has more energy. It was also shown that, at a given mass ratio ν, the closer equilibrium is always unstable while its conjugate solution is always stable. Hence, for a system dissipating energy, the "free energy" is defined by

$$\Delta E = E_{URE} - E_{SRE}, \tag{2.100}$$

where E_{URE} is the energy at the unstable configuration and E_{SRE} is the one at

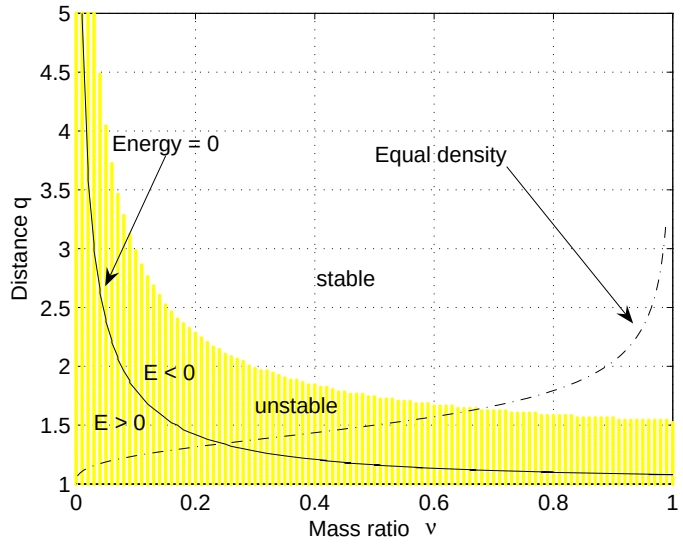

Figure 2.9: Stability diagram for planar motion, for the distance between the bodies as function of the system mass ratio. The clear region denotes spectral stability while the shaded one denotes spectral instability from a single hyperbolic manifold instability. The solid line indicates transition from positive to negative total energy of the system and the pointed dashed line assumes equal density of the binary bodies. Parameters are $\alpha = 1$, $\beta = 0.5$, $\gamma = 0.25$. [79]

the stable equilibrium, which is also the minimum energy state as described in the previous section. Eq. (2.100) gives a measure of the energy that must be dissipated to transition from an unstable to a stable state.

Previous work has mapped relative equilibria solutions as a function of the mass ratio, also characterizing their stability and energy properties [79]. Figure 2.9 shows results for an ellipsoid with semi-major axes of $\alpha = 1$, $\beta = 0.5$ and $\gamma = 0.25$. On this plot, every point is a relative equilibrium and the shaded region indicates the transition between stable and unstable equilibrium. The solid line represents the transition from negative to positive total energy of the system, i.e. $E = 0$. For $E > 0$, this indicates the capability of the binary system to evolve into an escaping system with sufficient perturbation. Finally the pointed dashed line indicates the distance between the bodies when resting on each other, assuming they have the same density. Note that each relative equilibrium in Figure 2.9 corresponds to a different value of angular momentum in general.

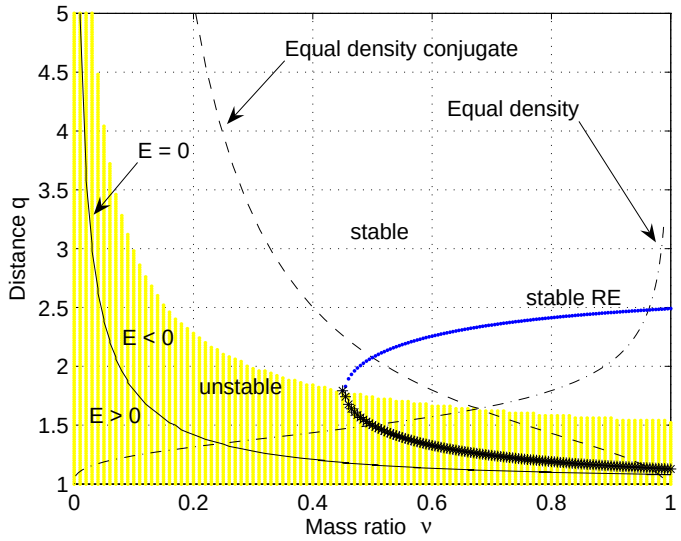

Figure 2.10: Stability diagram for planar motion, for the distance between the bodies as function of the system mass ratio. The clear region denotes spectral stability while the shaded one denotes spectral instability from a single hyperbolic manifold instability. The U-shape represents a locus of solutions q as function of the mass ratio, for a constant angular momentum; we can find at most two solutions given a value of angular momentum. The upper and lower branches are unstable and stable solutions, respectively. The dashed and pointed dashed lines are equal density solutions with their conjugate. Ellipsoidal parameters are $\alpha = 1$, $\beta = 0.5$, $\gamma = 0.25$.

Comparing Figure 2.9 to the case shown in Figure 2.7 where the angular moment was kept constant, the C-shaped curve, or Locus of solutions, has its tip sitting on the stability transition of the relative equilibria solutions. The resulting plot is shown in Figure 2.10. The lower branch is situated in the unstable shaded region of the plot while the upper branch is in the stable region. The C-shaped curve fits with the "far" solutions, or conjugate solutions; the dashed line in Figure 2.10 are the conjugate solutions to the equal density solutions (pointed dashed line). The intersections of the C-shaped curve with the dashed line correspond to two solutions for equal density and the same angular momentum, having mass ratios of $\nu = 0.5$ and $\nu = 0.96$ in this case.

In addition to energy and stability properties, an extension of Figures 2.7 and 2.8 gives further information on the system evolution in terms of energy and momentum exchange. Looking at Figure 2.11, the Locus of solutions shifts to the right as

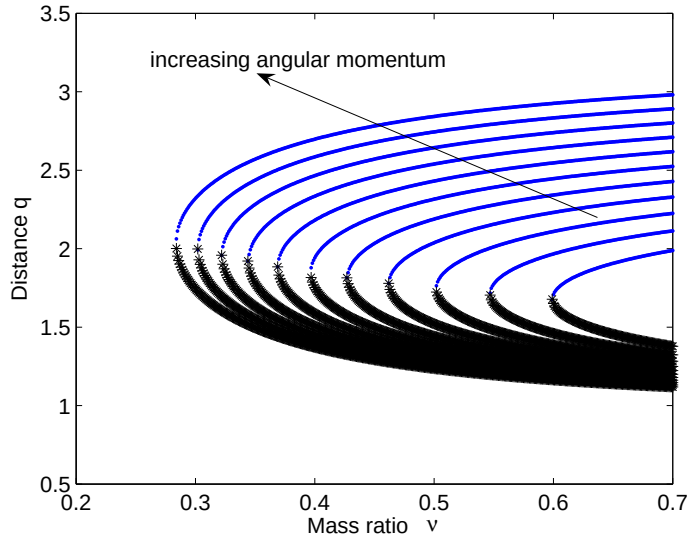

Figure 2.11: Bifurcation solution q as function of the mass ratio ν, and values of angular momentum K, from 1.65 to 1.85 (normalized) $\beta = 0.5$ and $\gamma = 0.25$. The lower and upper branches represent stable and unstable solutions, respectively.

the angular momentum is decreased. Thus, for a system in relative equilibrium at a solution located on the lower branch of a given C-shaped curve, that is, in an unstable configuration, losing angular momentum would make this solution move upwards. Hence the bodies become more distant when losing angular momentum while approaching more stable configurations. Finally, a system with a higher value of angular momentum may have a solution with its energy being positive. In this case, the system would first need to lose energy in order to become bound ($E < 0$) and then evolve towards a more stable configuration.

2.5 Non-Relative Equilibrium Dynamics for an Ellipsoid-Sphere System

2.5.1 Problem Definition

Non-equilibrium dynamics of the F2BP are more commonly found in nature since the asteroids of a binary system may not have formed together. Each of them may have their own velocities and angular momentum. In this case, the complete equations of

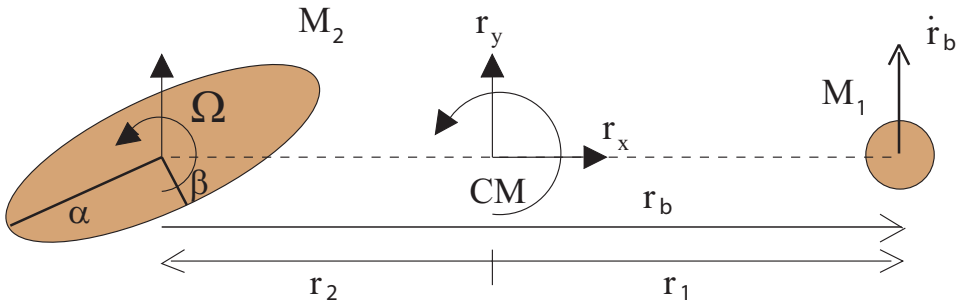

Figure 2.12: Geometry of the Full Two Body Problem.

motion defined by Eqs. (2.32-2.35) need to be solved. Again, the problem involves up to twelve degrees of freedom. With the ellipsoid-sphere system, the situation is now back to the ellipsoid having a different spin compared to the system orbit rate, which is shown again in Figure 2.12 for clarity. As a next step to the simplification using the relative equilibria assumption, the regions near these relative equilibria are investigated, especially for symmetric periodic orbits. The goal is to link this dynamics of small motion near the equilibrium states to possible evolutionary paths in the F2BP.

2.5.2 Periodic Orbits: Poincaré Map Reduction Method

The computation of periodic orbits is performed using a Poincaré map reduction method as discussed in [97]. For this work, a surface of section normal to the flow, denoted $S(\boldsymbol{q})$, is chosen in the vicinity of a given solution, which allows one to find symmetric periodic orbits. A convenient choice is a coordinate axis, or $q_i = 0$ in the Cartesian space. The Poincaré map is defined as the solution $\boldsymbol{q}(t)$ crosses the surface with the condition that $\boldsymbol{q}(t)|_{q_x=S} \cdot \nabla(S) > 0$. With this surface of section, it is possible to remove one dimension from consideration using $S(\boldsymbol{q}) = 0$. If the system has a conserved quantity, another dimension can be removed. The Poincaré map reduction method is pictured in Figure 2.13.

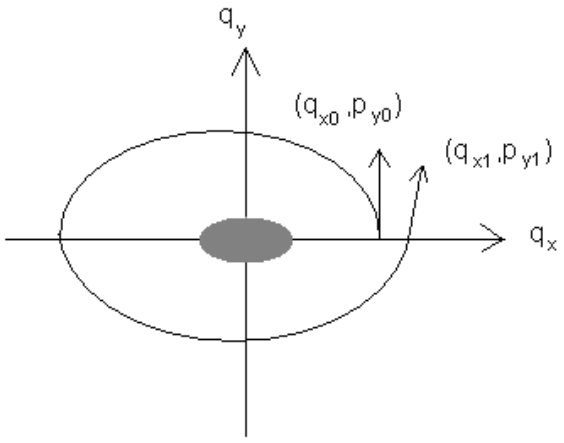

Figure 2.13: The Poincaré map reduction method.

In the planar problem, the full state is defined as

$$\boldsymbol{x} = \begin{bmatrix} q_x \\ q_y \\ p_x \\ p_y \end{bmatrix}, \tag{2.101}$$

and C is a vector of parameters. If the first return of the Poincaré map is

$$x_i^1 = Q(x_i^0, C),\ i \in 1, 2, \cdots \tag{2.102}$$

where x_i is a variable of the full state, then the n^{th} iterate is

$$x_i^n = Q^n(x_i, C). \tag{2.103}$$

A periodic orbit is defined as a point $\boldsymbol{x}^*$ such that

$$\boldsymbol{x}^* = Q(\boldsymbol{x}^*, C). \tag{2.104}$$

Since a given initial condition $\boldsymbol{x_0}$ would not necessary give a true periodic orbit, the correction to the state can be computed such that

$$\boldsymbol{x_0} + \Delta x = Q(\boldsymbol{x_0} + \Delta \boldsymbol{x}, C) = Q(\boldsymbol{x_0}) + \left.\frac{\partial Q}{\partial \boldsymbol{x}}\right|_{\boldsymbol{x_0}} \Delta \boldsymbol{x} + ... \tag{2.105}$$

Then,

$$\Delta \boldsymbol{x} = \left[I - \Phi(T)\right]^{-1} \left(Q(\boldsymbol{x_0}) - \boldsymbol{x_0}\right), \tag{2.106}$$

where $\Phi(T) = \left.\frac{\partial Q}{\partial \boldsymbol{x}}\right|_{\boldsymbol{x_0}}$. The method converges if started close enough to the fixed point, $\boldsymbol{x}^*$, and if the matrix in Eq. (2.106) is nonsingular (also see [19] for details on solutions of linear equations).

This method is used with the Hamiltonian form of the equations of motion. The surface of section is chosen to be the q_x axis, i.e. $q_y = 0$. To extend the map to its first linear variation, the four dimensional state transition matrix of the system is computed, denoted as $\Phi_{i,j}$, where $i, j = 1, 2..4$. Since in this time-invariant system, a closed trajectory has 2 unity eigenvalues, the state transition matrix is degenerate at the periodic orbit. Due to this, variations along the surface of section and the energy integral must be removed. In the following, the method described in [88] is applied.

With the surface of section and the energy integral, it is possible to remove two coordinate dimensions, q_y and p_y, leading to a two-dimensional monodromy matrix. In order to do so, the linear variation is constrained to lie on the Poincaré surface.

In the vicinity of a periodic orbit, the first return of q_y is not necessarily zero. It is expressed as

$$\Delta q_y(T) = \sum_{\substack{j=1 \\ j \neq 2}}^{4} \Phi_{2j}(T, 0) \Delta x_j(0), \tag{2.107}$$

where $i, j = 1, 3$ or 4, and T is the return time. To force $\Delta q_y(T)$ to be zero, a small

variation of return time ΔT is introduced such that

$$\Delta q_y(T+\Delta T) = \sum_{\substack{j=1 \\ j\neq 2}}^{4} \Phi_{2j}(T,0)\Delta x_j(0) + \dot{q_y}\Delta T = 0. \tag{2.108}$$

In solving for ΔT, the linear variation of the Poincaré map becomes

$$\Psi_{i,j} = \Phi_{i,j}(T) - \frac{\dot{x_i}}{\dot{q_y}}\Phi_{2j}(T). \tag{2.109}$$

Now using the energy integral, the p_y coordinate which is transverse to the surface of section can be solved for to remove one more dimension. This gives

$$\Delta p_y = -\frac{1}{E_{p_y}}(E_{q_x}\Delta q_x + E_{p_x}\Delta p_x), \tag{2.110}$$

where E is the energy integral given by Eq. (2.28). Applying this at the initial time, t=0, and substituting for Δp_y gives the final form of the 2×2 monodromy matrix, $\Psi(T)$,

$$\Psi_{i,j} = \Phi_{i,j}(T) - \frac{\dot{x_i}}{\dot{q_y}}\Phi_{2,j}(T) - \frac{1}{\dot{q_y}(0)}\left[\Phi_{i,4}(T) - \frac{\dot{x_i}}{\dot{q_y}}\Phi_{2,4}(T)\right]\frac{\partial E}{\partial x_j}(0), \tag{2.111}$$

where $i, j = 1, 3$.

Therefore, the dynamical system is integrated for until the condition $q_y = 0$ is met, then the monodromy matrix can be computed from the state transition matrix using Eq. (2.111). If the reduced state is defined as

$$\boldsymbol{y} = \begin{bmatrix} q_x \\ \\ p_x \end{bmatrix} \tag{2.112}$$

in the vicinity of a periodic orbit, the correction to the initial reduced state is calculated from

$$\Delta \boldsymbol{y} = (I - \Psi(T))^{-1}(Q(\boldsymbol{y_0}) - \boldsymbol{y_0}), \tag{2.113}$$

where $\Psi(T)$ is the 2×2 monodromy matrix, $Q(\boldsymbol{y_0})$ is the computed reduced state and $\boldsymbol{y_0}$ is the initial reduced state.

This procedure gives corrections to q_x and p_x as two degrees of freedom are removed from the map reduction method and energy integral. Correction to p_y is computed from conservation of the energy integral evaluated after one period,

$$\Delta p_y = -\frac{1}{H_{p_y}}(H_{q_x}\Delta q_x + H_{p_x}\Delta p_x) \tag{2.114}$$

or

$$\Delta p_y = -\frac{1}{\dot{q_y}}(-\dot{p_x}\Delta q_x + \dot{q_x}\Delta p_x). \tag{2.115}$$

Having obtained $\Delta \boldsymbol{y}$ and Δp_y, the new initial full state is then updated by $\boldsymbol{x_0} = \boldsymbol{x_0} + \Delta \boldsymbol{x}$, and the process is iterated until the difference between the computed state $Q(\boldsymbol{y_0})$ and the initial state $\boldsymbol{y_0}$ is comparable to numerical solver tolerances. In the following sections, for convenience the numerical values reported converge to within 1% after the first iteration. However, the simulations shown were carried to absolute tolerance of 1×10^{-8}.

2.5.3 Continuation Methods

Varying a parameter C may have show some interesting characteristics and effects on periodic orbits. It is possible to continue a periodic family with respect to one of the system parameters C. From the assumption that a periodic orbit is expressed as $\boldsymbol{y^*} = Q(\boldsymbol{y^*}, C)$, a nearby periodic orbit will satisfy

$$\boldsymbol{y^*} + \Delta \boldsymbol{y} = Q(\boldsymbol{y^*} + \Delta \boldsymbol{y}, C + \Delta C). \tag{2.116}$$

Expanding Eq. (2.116) gives

$$\boldsymbol{y_0} + \Delta \boldsymbol{y} = Q(\boldsymbol{y_0} + \Delta \boldsymbol{y}, C + \Delta C) = Q(\boldsymbol{y_0}, C) + \left.\frac{\partial Q}{\partial \boldsymbol{y}}\right|_{\boldsymbol{y_0}} \Delta \boldsymbol{y} + \left.\frac{\partial Q}{\partial C}\right|_{\boldsymbol{y_0}} \Delta C... \tag{2.117}$$

These results are now applied to continuation with respect to the system energy and period. Equation (2.117) can be re-written to express the new correction term,

$\Delta \boldsymbol{y_C}$, as a function of ΔC,

$$\Delta \boldsymbol{y_C} = [I - \Psi(T)]^{-1} \left. \frac{\partial Q}{\partial C} \right|_{\boldsymbol{y^*}} \Delta C. \tag{2.118}$$

In the current problem, the method was applied for variation of the energy, E, and for the period, T. In the case of energy, the new correction term, $\Delta \boldsymbol{y_E}$, is found by,

$$\Delta \boldsymbol{y_E} = [I - \Psi(T)]^{-1} \left. \frac{\partial \boldsymbol{y}}{\partial E} \right|_{\boldsymbol{y^*}} \Delta E. \tag{2.119}$$

The expression for $\frac{\partial \boldsymbol{y}}{\partial E}$ is given by,

$$\frac{\partial y_i}{\partial E} = \left[\Phi_{ie} - \frac{\Phi_{pe} \dot{y_i}}{\dot{q_y}} \right] \frac{1}{\frac{\partial E}{\partial p_y}}, \tag{2.120}$$

where i is either 1 ($y_1 = q_x$) or 3 ($y_3 = p_x$), p is the index of the Poincaré map reduction (2, for q_y), and e is the index of the removed variable (4, for p_y).

Since the period is related to the energy, continuation with respect to the period has a slightly different form to account for this,

$$\Delta \boldsymbol{y_T} = [I - \Psi(T)]^{-1} \left(+ \left. \frac{\partial \boldsymbol{y}}{\partial T} \right|_{\boldsymbol{y^*}} \Delta T + \left. \frac{\partial \boldsymbol{y}}{\partial E} \right|_{\boldsymbol{y^*}} \Delta E \right). \tag{2.121}$$

From the current Poincaré map definition, the variation in q_y is written as

$$q_y(T + \Delta T) = 0 = q_y(T) + \dot{q}_y \Delta T + \frac{\partial q_y}{\partial E} \Delta E. \tag{2.122}$$

Or,

$$\dot{q}_y \Delta T = -\frac{\partial q_y}{\partial p_y} \frac{\partial p_y}{\partial E} \Delta E. \tag{2.123}$$

A variation in the reduced state $\boldsymbol{y}$ can also be written as

$$\Delta \boldsymbol{y} = \dot{y}_i \Delta T + \frac{\partial y_i}{\partial p_y} \frac{\partial p_y}{\partial E} \Delta E, \tag{2.124}$$

where i takes value for q_x and p_x, i.e. i=1, 3. Hence, for a continuation using the period, substituting Eq. (2.123) into Eq. (2.124), the following final expression for

the correction term $\Delta \boldsymbol{y_T}$ is obtained from

$$\Delta \boldsymbol{y_T} = [I - \Psi(T)]^{-1} \left(\dot{y}_i - \dot{q}_y \frac{\partial y_i}{\partial p_y} \frac{\partial p_y}{\partial q_y} \right) \Bigg|_{y^*} \Delta T. \tag{2.125}$$

The corrected initial full state is then fed into the Poincaré map method to converge to a periodic orbit again. Note that for cases of singularity with respect to the energy and the period, the periodic orbit families are terminated by doing a linear analysis, such as is presented in the next section.

2.5.4 Stability Analysis of Periodic Orbits

The stability of periodic orbits is analyzed from investigating the eigenvalues of the monodromy matrix. In [26] and [76], an analytical procedure is described to characterize critical points of periodic orbits and periodic orbit families in the Restricted Three-Body Problem (R3BP) and for motion close to rings, respectively. These methods are applied for the current problem to find periodic orbits in the F2BP.

First, recall the general expression for the monodromy matrix in Eq. (2.111),

$$\Psi = \begin{bmatrix} \Psi_{11} & \Psi_{12} \\ \Psi_{21} & \Psi_{22} \end{bmatrix}. \tag{2.126}$$

The monodromy matrix is a linearization around the fixed point of the full (nonlinear) Poincaré map. Points on the surface of section are mapped according to

$$\begin{bmatrix} \Delta q_x \\ \Delta p_x \end{bmatrix} = \begin{bmatrix} \Psi_{11} & \Psi_{12} \\ \Psi_{21} & \Psi_{22} \end{bmatrix} \begin{bmatrix} \Delta q_{x0} \\ \Delta p_{x0} \end{bmatrix}. \tag{2.127}$$

Note that the entries of the monodromy matrix are evaluated at the initial conditions for a periodic orbit and its determinant is

$$\Psi_{11}\Psi_{22} - \Psi_{12}\Psi_{21} = 1. \tag{2.128}$$

Since the initial conditions are chosen to be $q_{y0} = 0$ and $p_{x0} = 0$, the symmetry of the periodic orbit in space and time implies that $q_x(t) = q_x(-t)$ and $p_x(t) = -p_x(-t)$. Hence, one can write,

$$\begin{bmatrix} \Delta q_{x0} \\ \Delta p_{x0} \end{bmatrix} = \begin{bmatrix} \Psi_{11} & -\Psi_{12} \\ -\Psi_{21} & \Psi_{22} \end{bmatrix} \begin{bmatrix} \Delta q_x \\ \Delta p_x \end{bmatrix}. \tag{2.129}$$

Now, inverting Eq. (2.129),

$$\begin{bmatrix} \Delta q_x \\ \Delta p_x \end{bmatrix} = \begin{bmatrix} \Psi_{22} & \Psi_{12} \\ \Psi_{21} & \Psi_{11} \end{bmatrix} \begin{bmatrix} \Delta q_{x0} \\ \Delta p_{x0} \end{bmatrix}. \tag{2.130}$$

Therefore, comparing Eqs. (2.127-2.130), the condition needed is $\Psi_{11} = \Psi_{22}$, or

$$\begin{bmatrix} \Delta q_x \\ \Delta p_x \end{bmatrix} = \begin{bmatrix} \Psi_{11} & \Psi_{12} \\ \Psi_{21} & \Psi_{11} \end{bmatrix} \begin{bmatrix} \Delta q_{x0} \\ \Delta p_{x0} \end{bmatrix}. \tag{2.131}$$

Note that the determinant of the monodromy matrix is then written as,

$$\Psi_{11}^2 - \Psi_{12}\Psi_{21} = 1. \tag{2.132}$$

The stability of the periodic orbit is investigated using the eigenvalues of the monodromy matrix, computed from Eq. (2.131),

$$\lambda^2 - 2\Psi_{11}\lambda + 1 = 0. \tag{2.133}$$

For the system to be stable, the only condition is on the first entry of the monodromy matrix, Ψ_{11}, stated as

$$-1 \leq \Psi_{11} \leq 1. \tag{2.134}$$

Providing Eq. (2.134), λ will have unit magnitude or $|\lambda| = 1$, resulting in stable periodic orbits. A change in stability happens as Ψ_{11} goes through ± 1.

Now let's look at the monodromy matrix as given by Eq. (2.126) and the

following expression for $\frac{\partial Q}{\partial C}\big|_{\boldsymbol{y_0}}$,

$$\frac{\partial Q}{\partial C} = [h_1, h_2]^T. \tag{2.135}$$

Using Eqs. (2.126-2.135) into Eq. (2.117), $\Delta \boldsymbol{y}$ can be expressed in the following form,

$$\begin{bmatrix} \Delta q_x \\ \Delta p_x \end{bmatrix} = \begin{bmatrix} \Psi_{11} & \Psi_{12} & h_1 \\ \Psi_{21} & \Psi_{11} & h_2 \end{bmatrix} \begin{bmatrix} \Delta q_x \\ \Delta p_x \\ \Delta C \end{bmatrix}. \tag{2.136}$$

From the symmetry property in space and time, a variation in p_x will have no effect on q_x or the system parameter C, as $p_{x_0} = 0$. Hence, this allows to decouple the system and re-write Eq. (2.136) as

$$\begin{bmatrix} 0 \\ 0 \end{bmatrix} = \begin{bmatrix} \Psi_{11} - 1 & h_1 \\ \Psi_{21} & h_2 \end{bmatrix} \begin{bmatrix} \Delta q_x \\ \Delta C \end{bmatrix} \tag{2.137}$$

and

$$\begin{bmatrix} 0 & 0 \end{bmatrix} = \begin{bmatrix} \Psi_{12} & \Psi_{11} - 1 \end{bmatrix} \Delta p_x. \tag{2.138}$$

For the system to have a non-trivial solution, from Eq. (2.137), the condition is

$$\begin{vmatrix} \Psi_{11} - 1 & h_1 \\ \Psi_{21} & h_2 \end{vmatrix} = 0, \tag{2.139}$$

giving

$$(\Psi_{11} - 1)h_2 - h_1\Psi_{21} = 0. \tag{2.140}$$

In investigating for possible singular values in Eqs. (2.132-2.140), three cases need to be considered, $\Psi_{11} = 1$, $\Psi_{11} = -1$ and $\Psi_{11} \neq 1$.

2.5.5 Properties of the Monodromy Matrix

In the case $\Psi_{11} = 1$, Eqs. (2.132-2.140) become,

$$\Psi_{12}\Psi_{21} = 0 \tag{2.141}$$

and

$$h_1\Psi_{21} = 0. \tag{2.142}$$

At this value, a stability transition can occur. First, if $\Psi_{21} \neq 0$ and $\Psi_{12} = 0$, an explicit relation is found between Δq_x and ΔC,

$$\Delta q_x = -\frac{h_2}{\Psi_{21}}\Delta C. \tag{2.143}$$

In addition, $h_1 = 0$ in order to satisfy Eq. (2.137). Then, from Eq. (2.138), Δp_x is found to be arbitrary, implying an intersection with a non-symmetric periodic orbit of the same period [97].

On the other hand, if $\Psi_{21} = 0$ and $\Psi_{12} \neq 0$, Eqs. (2.137) become

$$h_1\Delta C = 0 \tag{2.144}$$

and

$$h_2\Delta C = 0. \tag{2.145}$$

Also, from Eq. (2.138), a third condition is now

$$\Psi_{12}\Delta p_x = 0. \tag{2.146}$$

From these equations above, $\Delta p_x = 0$, implying that intersection with a non-symmetric family does not occur.

If $h_1 = h_2 = 0$, Δq_x and ΔC are arbitrary, not unique and free to vary, this indicates an intersection with another symmetric family of the same period. On the other hand, if h_1 or h_2 are not null, $\Delta C = 0$. In this case, there is no intersection

with another family and the periodic orbit family is at a local extremum of the system parameter C [97].

Now consider the case of $\Psi_{11} = -1$. Again, a stability transition can occur. Equations (2.132-2.140) become

$$\Psi_{12}\Psi_{21} = 0, \tag{2.147}$$

and

$$h_1\Psi_{21} = 2h_2. \tag{2.148}$$

Both situations can again be considered where $\Psi_{12} = 0$ and $\Psi_{21} = 0$. If $\Psi_{12} = 0$, Eqs. (2.137-2.138) become

$$-2\Delta q_x + h_1\Delta C = 0 \tag{2.149}$$

and

$$\Psi_{21}\Delta q_x + h_2\Delta C = 0, \tag{2.150}$$

with

$$\Delta p_x = 0 \tag{2.151}$$

and

$$-2\Delta p_x = 0. \tag{2.152}$$

This implies an intersection with a symmetric family of twice the period [97]. In this case, there is no condition on h_1 and h_2. A similar result is obtained when considering $\Psi_{21} = 0$. However, $h_2 = 0$ is needed to satisfy Eq. (2.148). From Eqs. (2.137-2.138), Δq_x is

$$\Delta q_x = \frac{h_1}{2}\Delta C. \tag{2.153}$$

Note that, in these cases, one can look at the nature of the double period family itself which should be consistent with the current monodromy matrix analysis. If Ψ is the monodromy matrix for the single period family, then at the intersection

point, the monodromy matrix of the double period family should have the form Ψ^2 . Hence, this should correspond to cases described at the beginning of this subsection where the double period family would most likely be at an extremum in one of its parameters.

Finally, let's consider the case of $\Psi_{11} \neq 1$. In this case, the general equations given by Eqs. (2.132-2.137-2.140) are considered. Since both of the Δp_x coefficients are non zero, $\Delta p_x = 0$ is the condition, which indicates that there is no intersection with a non-symmetric family.

Equation (2.137) define the tangent curves to the family

$$\Delta q_x = -\frac{h_1}{\Psi_{11} - 1}\Delta C \tag{2.154}$$

and

$$\Delta q_x = -\frac{h_2}{\Psi_{21}}\Delta C. \tag{2.155}$$

The case $h_1 = 0$ or $h_2 = 0$ implies $h_2 = 0$ or $h_1 = 0$, respectively. This leads to having a local extremum with respect to q_x. Otherwise there is a one-to-one relationship between the periodic family and parameter C. In general, two solutions can be found for Δq_x as shown in Figure 2.10.

Table 2.1 summarizes the cases mentioned. Notice that no cases lead to intersections with asymmetric periodic orbits, which explains why the methods and investigations were not extended to asymmetric periodic orbits.

2.5.6 Near Relative Equilibria Approximation

To simplify the analysis, an approximation method is also derived to model the dynamics in the F2BP near relative equilibria. The approach is to use the method of perturbations using eigenvalues and eigenvectors to generate the appropriate dynamics and solve for periodic orbits.

Cases	Ψ_{11}	Ψ_{12}	Ψ_{21}	h_1	h_2	Δq_x	Δp_x	ΔC	Remarks
a	1	0	$\neq 0$	0	$\neq 0$	$-\frac{h_2}{\Psi_{21}}\Delta C$	$\neq 0$	$\neq 0$	Intersection with a asymmetric periodic orbit family of the same period
b	1	$\neq 0$	0	$\neq 0$	$\neq 0$	$\neq 0$	0	0	No intersection with symmetric families, the periodic orbit family is at a local extremum of C
c	1	$\neq 0$	0	0	0	$\neq 0$	0	$\neq 0$	Intersection with another symmetric family of the same period
d	-1	0	$\neq 0$	$\neq 0$	$\neq 0$	$\neq 0$	0	$\neq 0$	Intersection with a symmetric family of twice the period
e	-1	$\neq 0$	0	$\neq 0$	0	$\frac{h_1}{2}\Delta C$	$\neq 0$	$\neq 0$	Intersection with an asymmetric family of twice the period
f	$\neq 1$	$\neq 0$	$\neq 0$	$\neq 0$	$\neq 0$	2 RE	0	$\neq 0$	No intersection
g	$\neq 1$	$\neq 0$	$\neq 0$	0	0	0	0	$\neq 0$	No intersection, local extremum in q_x

Table 2.1: Summary of stability conditions for a periodic orbit described in section 2.5.5. Ψ's are the components of the monodromy matrix while h's are derivatives with respect to a free parameter of the system, like the energy, denoted C. q_x and p_x are x-component of the position and inertial velocity. The notation "2 RE" indicates two relative equilibrium solutions.

Given Eqs.(2.30,4.23), a small perturbation to the nominal path is,

$$\begin{bmatrix} \boldsymbol{\delta\dot{q}} \\ \boldsymbol{\delta\dot{p}} \end{bmatrix} = JH_{xx} \begin{bmatrix} \boldsymbol{\delta q} \\ \boldsymbol{\delta p} \end{bmatrix}, \tag{2.156}$$

where J has the form

$$J = \begin{bmatrix} 0 & I \\ -I & 0 \end{bmatrix}, \tag{2.157}$$

and H_{xx} represents the second derivatives of the Hamiltonian defined by Eq.(2.28). Using the eigenvalues and eigenvectors of the system given by Eqs. (2.60-2.62), a solution is given by

$$\begin{bmatrix} \boldsymbol{\delta q} \\ \boldsymbol{\delta p} \end{bmatrix} = e^{\lambda_a t} \begin{bmatrix} \boldsymbol{u} \\ \boldsymbol{v} \end{bmatrix}, \tag{2.158}$$

where λ_a is an eigenvalue and $\boldsymbol{u}$ and $\boldsymbol{v}$ are the corresponding eigenvectors.

For stable motion, $\lambda_a = \pm i\omega_a$. And the general orbit is described by the corresponding set of eigenvectors, $\boldsymbol{u} = \boldsymbol{\alpha} \pm i\boldsymbol{\beta}$. Therefore, the periodic perturbation can be written as

$$\begin{bmatrix} \boldsymbol{\delta q} \\ \boldsymbol{\delta p} \end{bmatrix} = \frac{1}{2}(a\boldsymbol{\alpha} - b\boldsymbol{\beta}) \left[e^{i\omega_a t} + e^{-i\omega_a t}\right] - \frac{1}{2}(b\boldsymbol{\alpha} + a\boldsymbol{\beta}) \left[e^{i\omega_a t} - e^{-i\omega_a t}\right]. \tag{2.159}$$

Note that the constants $(a \pm ib)$ satisfy the condition for a real solution.

Using trigonometric identities, Eq. (2.159) is written as

$$\begin{bmatrix} \boldsymbol{\delta q} \\ \boldsymbol{\delta p} \end{bmatrix} = (a\boldsymbol{\alpha} - b\boldsymbol{\beta})\cos(\omega_a t) - (b\boldsymbol{\alpha} + a\boldsymbol{\beta})\sin(\omega_a t). \tag{2.160}$$

In order to solve for the constant and initial conditions, first assume

$$\begin{bmatrix} \delta q_{x0} \\ \delta q_{y0} \end{bmatrix} = \begin{bmatrix} a\alpha_{qx} - b\beta_{qx} \\ a\alpha_{qy} - b\beta_{qy} \end{bmatrix} = \begin{bmatrix} \delta q_0 \\ 0 \end{bmatrix}. \tag{2.161}$$

Then, solving for a and b from

$$\begin{bmatrix} a \\ b \end{bmatrix} = \frac{1}{\alpha_{qy}\beta_{qx} - \alpha_{qx}\beta_{qy}} \begin{bmatrix} -\beta_{qy}\delta q_0 \\ -\alpha_{qy}\delta q_0 \end{bmatrix}, \tag{2.162}$$

initial conditions on $\boldsymbol{\delta p}$ can then be solved,

$$\begin{bmatrix} \delta p_{x0} \\ \delta p_{y0} \end{bmatrix} = \frac{\delta q_0}{\alpha_{qy}\beta_{qx} - \alpha_{qx}\beta_{qy}} \begin{bmatrix} 0 \\ \alpha_{qy}\beta_{py} - \alpha_{py}\beta_{qy} \end{bmatrix}. \tag{2.163}$$

Hence, to first order approximation, a periodic orbit near a relative equilibrium is described by

$$\begin{bmatrix} \boldsymbol{q_{RE}} + \boldsymbol{\delta q} \\ \boldsymbol{p_{RE}} + \boldsymbol{\delta p} \end{bmatrix}, \tag{2.164}$$

where $\boldsymbol{q_{RE}}$ and $\boldsymbol{p_{RE}}$ are values at relative equilibrium, $\boldsymbol{\delta q}$, $\boldsymbol{\delta p}$, a and b are given by Eq. (2.160) and Eq. (2.162) respectively. The initial conditions are written as follows,

$$\begin{bmatrix} q_{x0} \\ q_{y0} \\ p_{x0} \\ p_{y0} \end{bmatrix} = \begin{bmatrix} q_{xRE} + \delta q_0 \\ 0 \\ 0 \\ p_{yRE} + \left(\frac{\alpha_{qy}\beta_{py} - \alpha_{py}\beta_{qy}}{\alpha_{qy}\beta_{qx} - \alpha_{qx}\beta_{qy}}\right)\delta q_0 \end{bmatrix}. \tag{2.165}$$

The method of eigenvalues gives a good approximation to the results obtained using the Poincaré map method in the vicinity of the relative equilibria. Figure 2.14 shows a periodic orbit using the approximation, which can be compared to periodic orbits in the next section. The periodic orbit is computed in the vicinity of a stable equilibrium solution, with $\nu = 0.5$, $r = 2.0749$, $\beta = 0.5$, and $\gamma = 0.25$.

It is important to note that the two methods developed to find periodic orbits in the F2BP can complement each other. The computations and initial guesses to converge to a periodic orbit using the Poincaré map can be tedious. By using the approximation method to generate the initial conditions, one can then use these

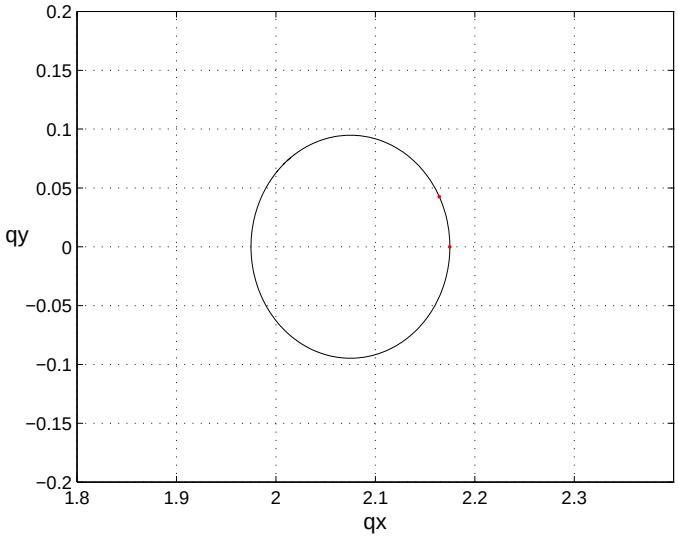

Figure 2.14: Periodic orbit using approximations in the vicinity of the stable relative equilibrium solution, $\nu = 0.5$, $r = 2.0749$, $\gamma = 0.5\beta = 0.5$.

values as initial guesses to start the Poincaré map method. The procedure is very useful to compute periodic orbits close to each other but from different families and to converge on unstable periodic orbits.

2.5.7 Periodic Orbits near Relative Equilibria for an Ellipsoid-Sphere System

Applying the method described in the previous sections, a family of periodic orbits in the neighborhood of a given relative equilibrium is investigated. A simple assumption is for the bodies to have equal density, and the system parameter space is investigated with this particular constraint. The second solution found for this same angular momentum defines the "conjugate" relative equilibrium. As shown in Figure 2.15, cases of mass ratio, $\nu = 0.15$, $\nu = 0.5$, and $\nu = 0.85$, were studied.

Let's first concentrate on an equal mass ratio, $\nu = 0.5$, with equal density of the bodies. Using Eq. (2.27), the spin rate, ω, and the corresponding value of the angular momentum, K, are computed. Then all solutions of the distance, q, between the bodies are solved for from Eq. (2.59). For this specific case, there exists two

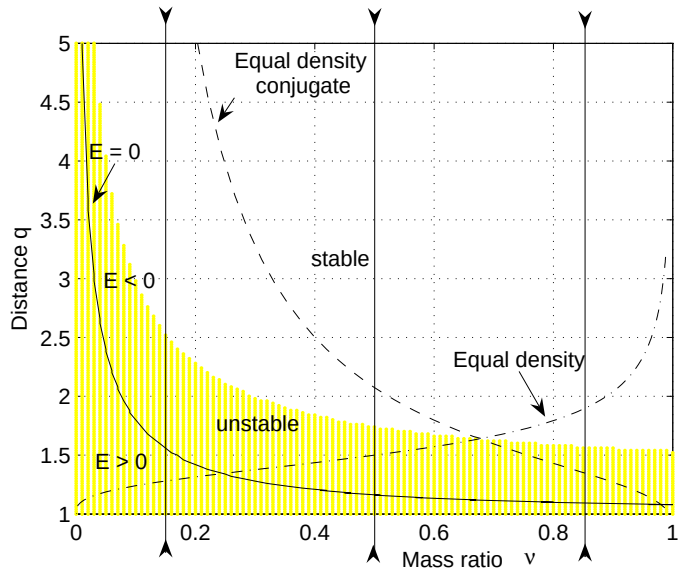

Figure 2.15: Stability diagram for planar motion in the long-axis solution. We investigate families of periodic orbits and the general dynamics near $\nu = 0.15$, $\nu = 0.5$ and $\nu = 0.85$. Ellipsoid parameters are $\alpha = 1$, $\beta = 0.5$, and $\gamma = 0.25$.

relative equilibrium at $q = 1.500$ and $q = 2.075$, which are the unstable and stable solutions, respectively (also shown in Figure 2.10). Note that at $q = 1.500$ the two bodies are sitting on each other.

For this specific value of the angular momentum, at $q = 1.500$ it is possible to compute one pair of imaginary eigenvalues and two sets of stable eigenvalues for $q = 2.075$. This allows to find one family of periodic orbit for the unstable point and two for the stable one. The absolute minimum energy state, at $q = 2.075$, is the stable relative equilibrium point itself. Figures 2.16a-b show the evolution of one of the periodic orbits as they get closer to the equilibrium point; these periodic orbits usually enclose the equilibrium point and shrink in size as the energy is decreased. At the limit, the periodic orbit becomes a single point where the period of the periodic orbit matches the period of oscillation of the relative equilibrium. For the unstable family, for the unstable equilibrium, the period is $T_{URE} = 6.852$. For the stable equilibrium, the period is found to be $T_{SRE} = 13.558$ or 38.336 in normalized time units.

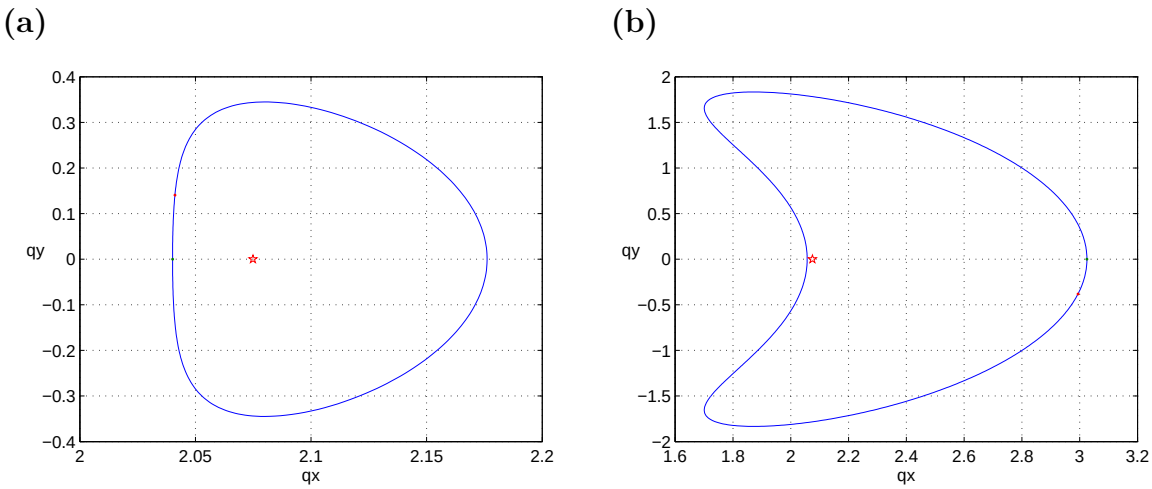

Figure 2.16: Periodic orbit families for $\nu = 0.5$, $K = 1.715$ and ellipsoid parameters, $\alpha = 1$, $\beta = 0.5$ and $\gamma = 0.25$. Evolution of periodic orbits in a q_x-q_y coordinate frame near the $q = 2.075$ relative equilibrium having a period $T_{SRE} = 13.558$. a - Periodic orbit: $q_{x0} = 2.182$ and $p_{y0} = 0.698$ with $E = -0.195$. b - Periodic orbit: $q_{x0} = 3.021$ and $p_{y0} = 0.507$ with $E = -0.176$. The energy of the equilibrium solution, indicated by the starred point, is $E = -0.197$.

From using the continuation method, Figure 2.17 shows the unstable family near $q = 1.500$ and the two families of periodic orbits, converging to $q = 2.075$. Note that these families have the same particular value of angular momentum but different energy. On this plot, the distance between the primary, q_{x0} is plotted as a function of the energy of the system, E. The star point represents the relative equilibrium or minimum energy point for this value of angular momentum. From this point, the upper and lower branches of each family are the two values of q_{x0} at which orbits of the family cross the q_y axis.

In Figure 2.17, a change in stability is marked at the "o" point. In the region closer to the equilibrium point, the periodic orbits are stable. Otherwise, they are unstable. This critical point is found from investigating the eigenvalues of the monodromy matrix but can also be analyzed from entries of the monodromy matrix itself as described in the section on stability and continuation properties and shown on Table 1. In the present case, the critical point in Figure 2.17 for which the stability changes has energy $E = -0.186$. This point intersects with a

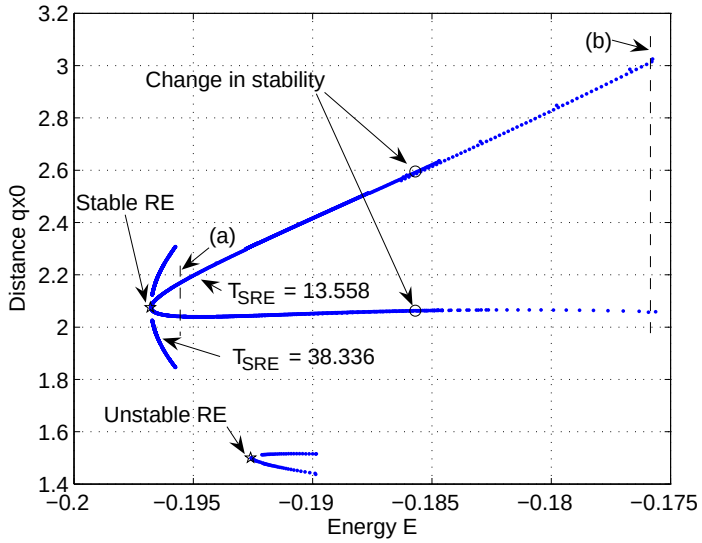

Figure 2.17: Periodic orbit families for $\nu = 0.5$, $K = 1.715$ and ellipsoid parameters, $\alpha = 1$, $\beta = 0.5$ and $\gamma = 0.25$. Continuation for all three families of periodic orbits: q_{x0} vs E. The two vertical dashed lines indicate the location of the two periodic orbits shown in Figures 2.16a-b. Note that for the unstable RE at q_{x0}, the bodies are sitting on each other.

space-symmetric family of twice the period and conditions as specified by case e on Table 2.1 are retrieved.

The previous analysis was obtained for an equally divided binary system. Having a dominant ellipsoid or a dominant sphere also affects these periodic orbit families. In Figures 2.18-2.19 periodic orbits and family continuations are plotted for cases of equal density binary systems with mass ratios of 0.15 and 0.85, respectively, in the vicinity of the stable relative equilibrium (see Figure 2.15). For $\nu = 0.15$, stable and unstable equilibria are $q = 6.913$ and $q = 1.285$, respectively, where the periods of the stable equilibrium are $T_{SRE} = 230.431$ and 112.000, labeled in Figure 2.18b. Note that only the shorter period family is shown for $\nu = 0.85$ in Figure 2.19b, where $T_{SRE} = 9.814$ for its stable equilibrium at $q = 1.893$. This stable equilibrium has a long period $T_{SRE} = 27.988$. One can see that the periodic orbits are reduced in size for small mass ratio; for similar wideness on the q_x axis, the orbits become taller as the mass ratio increases. Periodic orbits can also have the relative equilibrium

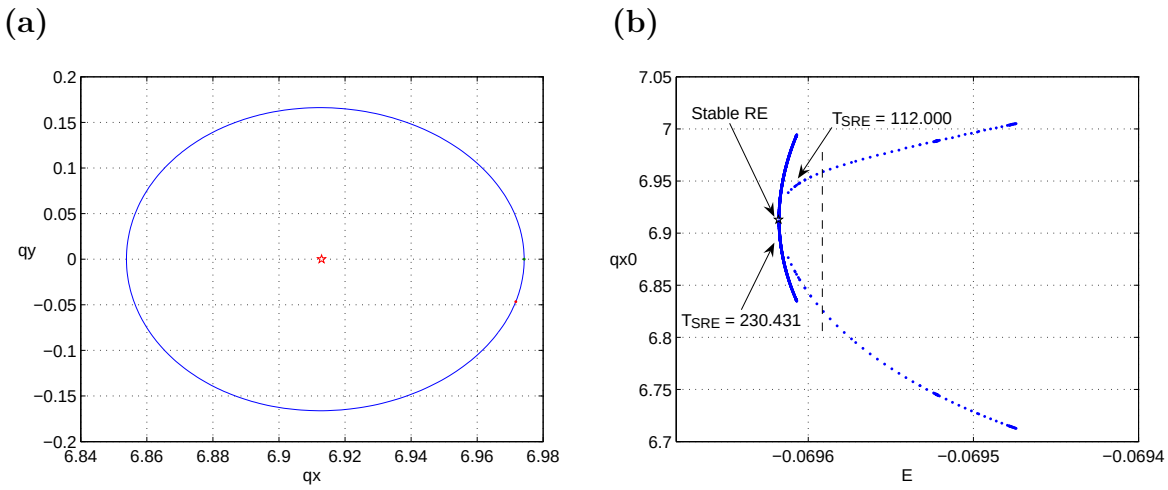

Figure 2.18: a) Periodic orbit: $q_{x0} = 6.974$ and $p_{y0} = 0.379$ with $E = -0.069625$. b) Periodic orbit families for $\nu = 0.15$, shown as q_{x0} vs E. Note that the unstable family exists but is not shown. In a) and b), the ellipsoidal parameters are $[\alpha : \beta : \gamma] = [1 : 0.5 : 0.25]$. The vertical dashed line indicates the location of the periodic orbit shown in a). The starred point is the stable relative equilibrium state, which has $E = -0.0696$.

solution outside of the orbit for large mass ratio.

Also note that periodic orbits can be found in the vicinity of the bifurcation point where stable and unstable relative equilibria meet (see Figure 2.10) for all values of the mass ratio. Looking at the 2×2 monodromy matrix, these points can be linked to the minimum energy case in Table 1, i.e. case b. Finally, case c is retrieved for $\nu = 0.68$ and $q = 1.641$, associated with an energy $E = -0.223$, which corresponds to the meeting point of the equal density solution and its conjugate solution.

The results on periodic orbits in the F2BP are an important contribution, linking periodic perturbations to the relative equilibrium solutions and their stability. The techniques and models used to compute these periodic orbits will also serve as a basis in the analysis of spacecraft dynamics in this environment, introduced in the next chapter. However, a natural extension is to investigate the possible transition of a binary system evolving from an unstable to a stable state, which is discussed in the following last section.

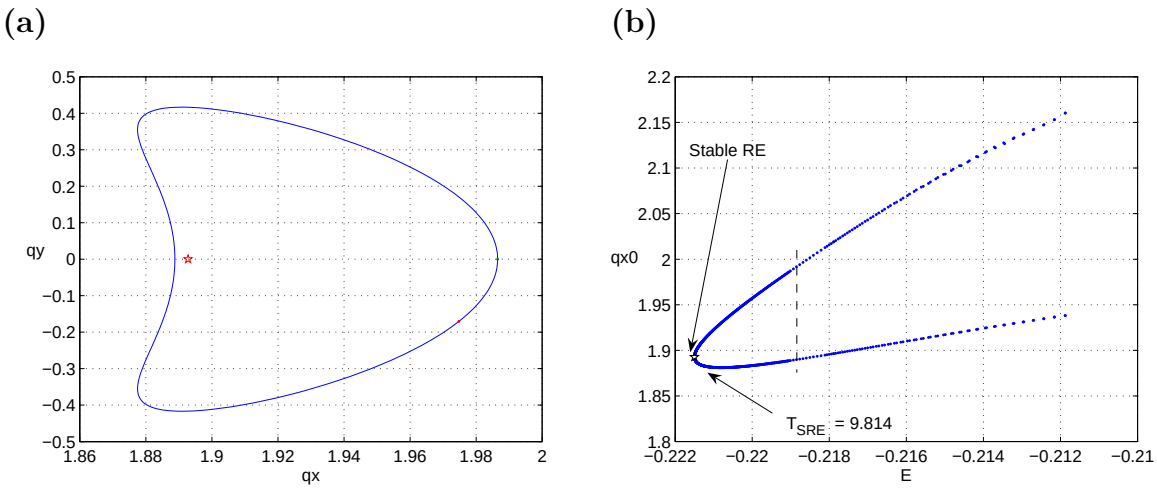

Figure 2.19: a) Periodic orbit: $q_{x0} = 1.985$ and $p_{y0} = 0.795$ with $E = -0.219$. b) Periodic orbit families for $\nu = 0.85$, shown as q_{x0} vs E. In a) and b), the ellipsoidal parameters are $[\alpha : \beta : \gamma] = [1 : 0.5 : 0.25]$. The vertical dashed line indicates the location of the periodic orbit shown in a). The starred point is the stable relative equilibrium state, which has $E = -0.222$.

2.6 Evolutionary Scenarios for an Ellipsoid-Sphere System

The results obtained on the relative equilibria and the periodic orbits give insights on the possible evolution scenarios of a binary system. Theories of binary systems formation include ones where a system may have dissociated from a single body [82]. Since a closer equilibrium configuration is unstable and the system may dissipate energy, it is natural to investigate possible transition of the system to reach a more stable orbit. Figures 2.20-2.22 show simulations for mass ratios of $\nu = 0.15$, $\nu = 0.25$ and $\nu = 0.5$ when the equal density binary system starts near an unstable relative equilibrium, with the bodies sitting on each other. In Figure 2.20, since the system starts with a positive energy, that is $E = 0.265$, the bodies may escape from each other. However, one can see that the trajectories following the unstable manifold may cross the stable trajectories. Under energy dissipation, the system may eventually reach stable periodic orbits or even arrive at a stable equilibrium configuration at the minimum energy state, $E = -0.070$. Figure 2.21 shows the same

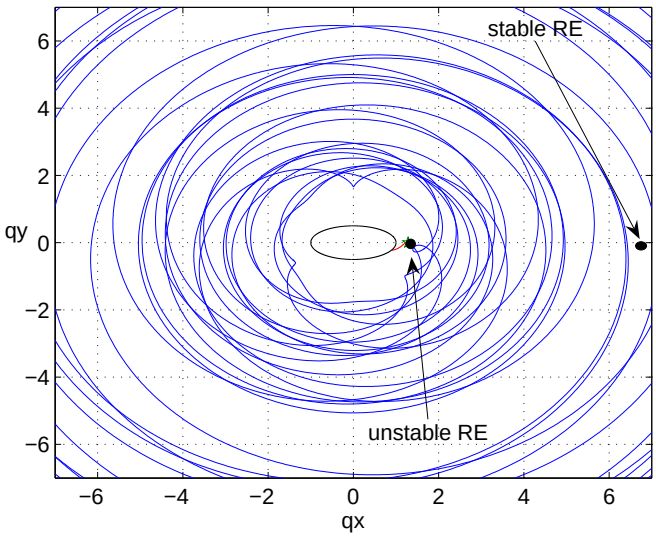

Figure 2.20: Dynamics in the F2BP when the bodies are close to being at the closer unstable relative equilibrium. The trajectories following the unstable manifold cross the stable trajectories. Under energy dissipation, transition from an unstable to a stable state may be possible. The system mass ratio is $\nu = 0.15$ with a "free energy" $\Delta E = 0.335$. Ellipsoidal parameters are $[\alpha : \beta : \gamma] = [1 : 0.5 : 0.25]$.

simulation for $\nu = 0.25$. In this case, the system starts at the unstable configuration with a negative energy, $E = -0.016$. In this case, the orbit is bounded and the bodies do not escape. Reaching $E = -0.119$ from energy dissipation, the system could achieve a stable configuration. The case of $\nu = 0.5$ is described in Figure 2.22 where the two equilibria are much closer to each other, starting with $E = -0.192$, and with a stable configuration at $E = -0.196$.

This possible transition between an unstable and a stable configuration can be quantified from values of energy at the two relative equilibria, defined earlier by the "free energy" of the system ΔE in Eq. (2.100). For the dynamics in Figure 2.20, the system has $\Delta E = 0.335$ starting near the unstable point with a positive energy. It needs to dissipate 80% of its free energy before getting bound, with $E = 0$. For $\nu = 0.25$, the system is already bound and has a free energy of $\Delta E = 0.135$. In Figure 2.22, with a mass ratio of $\nu = 0.5$, the system's free energy is low, $\Delta E = 0.004$, making the trajectories near the unstable point stay close to the stable

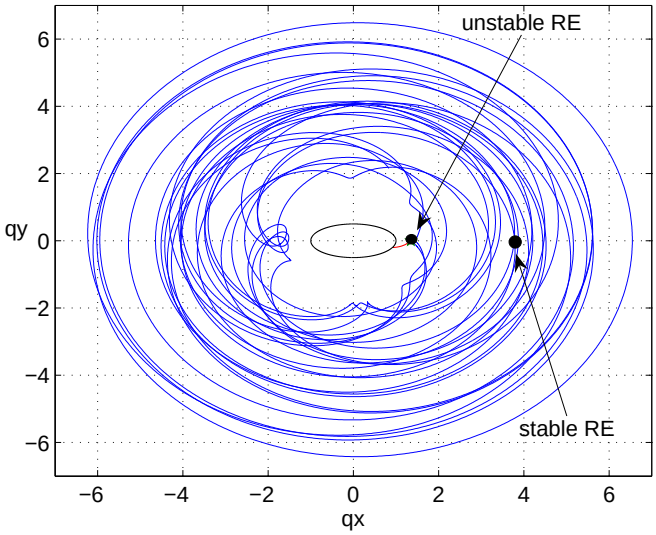

Figure 2.21: Dynamics in the F2BP when the bodies are close to being at the closer unstable relative equilibrium. The trajectories following the unstable manifold cross the stable trajectories. Under energy dissipation, transition from an unstable to a stable state may be possible. The system mass ratio is $\nu = 0.25$ with a "free energy" $\Delta E = 0.135$. Ellipsoidal parameters are $[\alpha : \beta : \gamma] = [1 : 0.5 : 0.25]$.

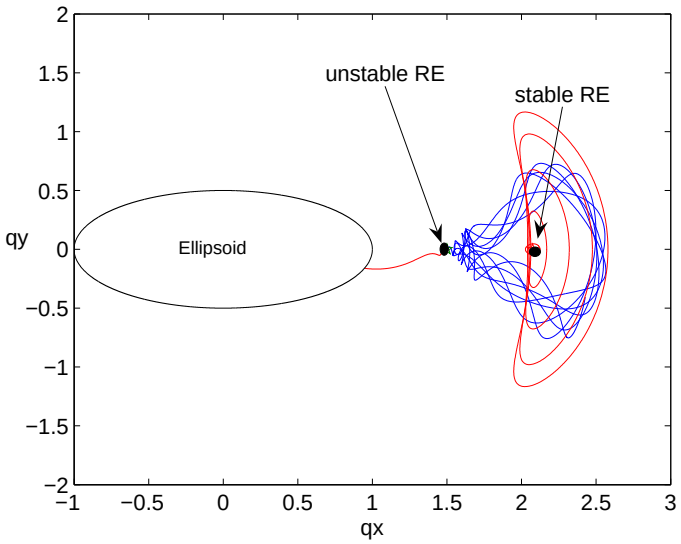

Figure 2.22: Dynamics in the F2BP when the bodies are close to being at the closer unstable relative equilibrium. The trajectories following the unstable manifold cross the stable trajectories. Under energy dissipation, transition from an unstable to a stable state may be possible. The system mass ratio is $\nu = 0.5$ with a "free energy" $\Delta E = 0.004$. Ellipsoidal parameters are $[\alpha : \beta : \gamma] = [1 : 0.5 : 0.25]$.

orbits. At $\nu = 0.85$, in this case there is no "free energy" at the unstable resting equilibrium point since this point lies inside the ellipsoid. Hence, at $q = 1.893$, the system is already at its lowest energetic point.

As mentioned, these simulations provide insights on the system evolution, which can be studied in much more detail. However, having knowledge of this possible transition path may be of use when sending a science mission, and depending on the astronomical data of a binary system. On a much smaller time scale, the models and results on relative equilibria and periodic orbits will be used as underlying dynamics when studying the motion of a particle or spacecraft in this gravitational environment, which is introduced next.

CHAPTER 3

THE RESTRICTED FULL THREE-BODY PROBLEM

3.1 Equations of Motion

Having defined the dynamics of the Full Two-Body Problem (F2BP), let's now consider a point mass particle, or spacecraft, in the gravitational field of the binary system. Since the particle does not affect the motion of the primaries and the mass distribution of one of the primaries is taken into account, the problem is referred as the Restricted Full Three Body Problem (RF3BP). As for the F2BP, the sphere restriction is used in order to reduce the complexity of the problem. And again, as for the F2BP, the equations of motion can be developed in a few different ways using either an inertial coordinate frame, a frame rotating with the orbit, or a frame rotating with the non-spherical body. As mentioned in Chapter 2, a frame fixed to the non-spherical body is more convenient to work with as it allows to eliminate its attitude from the equations of motion. In addition, the rotating frame is chosen to be fixed at the binary system's center of mass. In this frame, the two binary bodies may not have a synchronized motion. However, the normalization introduced for the F2BP can also be used for the RF3BP.

As for the F2BP, the symmetry of a tri-axial ellipsoid is used to model the general body in order to simplify the problem while keeping the interesting dynamical features. The RF3BP is shown in Figure 3.1 where a spacecraft, treated as a point mass particle, is added to the binary system studied in Chapter 2. In this figure, the

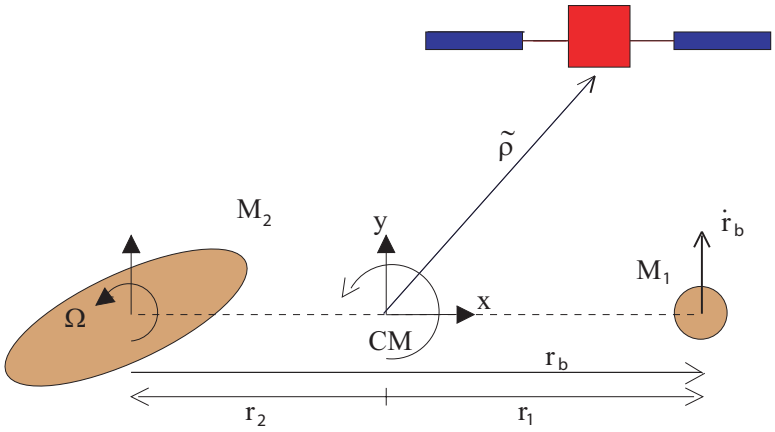

Figure 3.1: The Restricted Full Three-Body Problem

added variable, $\tilde{\boldsymbol{\rho}}$, is the position vector of the spacecraft relative to the center of mass of the system.

The equations of motion for the RF3BP were originally derived in [84]. The dynamics are expressed as,

$$\ddot{\tilde{\boldsymbol{\rho}}} + 2\boldsymbol{\Omega} \times \dot{\tilde{\boldsymbol{\rho}}} + \dot{\boldsymbol{\Omega}} \times \tilde{\boldsymbol{\rho}} + \boldsymbol{\Omega} \times (\boldsymbol{\Omega} \times \tilde{\boldsymbol{\rho}}) = \frac{\partial \tilde{U}_{12}}{\partial \tilde{\boldsymbol{\rho}}}, \tag{3.1}$$

with the potential having contributions from the sphere and the ellipsoid, expressed as

$$\tilde{U}_{12} = \frac{GM_1}{|\tilde{\boldsymbol{\rho}} - (1-\nu)\boldsymbol{r_b}|} + GM_2\tilde{U}_e(\tilde{\boldsymbol{\rho}} + \nu\boldsymbol{r_b}), \tag{3.2}$$

and where Ω is the general body angular velocity and U_e is given by Eqs. (2.18-2.20).

It is possible to look at two different cases for the RF3BP by using the dynamics defined in the F2BP. First, the bodies can be in relative equilibrium, keeping the same configuration as they orbit each other. The first section looks at the dynamics of particles under this assumption. In this case, one can investigate the energy constraints on the motion of spacecraft or particles from the integral of motion, zero-velocity curves, and analogue Lagrangian points. Other trajectories such as periodic orbits can also be computed under this assumption.

When the relative equilibrium assumption is dropped, the problem becomes time dependent, and in general the system no longer has an integral of motion nor equilibrium points. For example, in such cases, the analogue Lagrangian points are not points anymore but become periodic orbits synchronized with the ellipsoid spin or with the period of the binary system. These dynamics are investigated in the second half of this chapter.

3.2 Dynamics of the Restricted Full Three Body Problem (RF3BP) under Relative Equilibria in the Full Two Body Problem (F2BP)

As a start, it is assumed that the binary system is in the long-axis locked relative equilibrium discussed in the first half of Chapter 2. As shown in Figure 3.2, the same geometry as defined in Figure 2.6 is kept for the F2BP and the position of a particle is expressed as $\boldsymbol{\rho} = x\hat{\imath} + y\hat{\jmath} + z\hat{k}$ relative to the center of mass of the system.

For convenience and consistency with the work developed in Chapter 2, the maximum radius of the ellipsoid, α, and the mean motion of the system at this radius, $n = \sqrt{G(M_1 + M_2)/\alpha^3}$, are again chosen as length and time scales again, respectively. In normalized units, Eq.(3.1) becomes

$$\ddot{\boldsymbol{\rho}} + 2\boldsymbol{\omega} \times \dot{\boldsymbol{\rho}} + \boldsymbol{\omega} \times (\boldsymbol{\omega} \times \boldsymbol{\rho}) = \frac{\partial U_{12}}{\partial \boldsymbol{\rho}}, \tag{3.3}$$

where $\boldsymbol{\rho} = \frac{\tilde{\boldsymbol{\rho}}}{\alpha}$ is the normalized distance of the particle with respect to the system's center of mass. The potential U_{12} is given by

$$U_{12} = \frac{\nu}{|\boldsymbol{\rho} - (1-\nu)\boldsymbol{r}|} + (1-\nu)U_e(\boldsymbol{\rho} + \nu\boldsymbol{r}), \tag{3.4}$$

where U_e is the normalized ellipsoid potential, as given by Eqs. (2.18-2.20), and $\boldsymbol{r}$ is the normalized distance between the primaries. With the ellipsoid-sphere system in relative equilibrium, and having a coordinate frame fixed to the ellipsoid, U_{12} is a

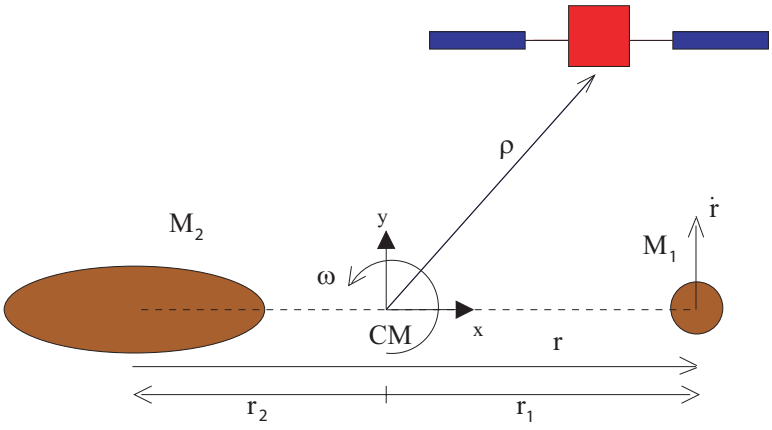

Figure 3.2: The Restricted Full Three-Body Problem under relative equilibrium of the F2BP.

time-invariant potential energy expression.

The free parameters of this system are the mass ratio, ν, the distance between the two bodies, $r = |\boldsymbol{r}|$, and the size parameters of the ellipsoid, β and γ. Given these parameters, the spin rate ω is given by Eq.(2.27). The equations of motion in the $\hat{\imath} - \hat{\jmath} - \hat{k}$ plane are written as

$$\ddot{x} - 2\omega\dot{y} - \omega^2 x = \frac{-\nu(x - (1-\nu)r)}{\left[(x-(1-\nu)r)^2 + y^2 + z^2\right]^{\frac{3}{2}}} - (1-\nu)(x+\nu r)R_{j\alpha}, \tag{3.5}$$

$$\ddot{y} + 2\omega\dot{x} - \omega^2 y = \frac{-\nu y}{\left[(x-(1-\nu)r)^2 + y^2 + z^2\right]^{\frac{3}{2}}} - (1-\nu)(y)R_{j\beta}, \tag{3.6}$$

and

$$\ddot{z} = \frac{-\nu z}{\left[(x-(1-\nu)r)^2 + y^2 + z^2\right]^{\frac{3}{2}}} - (1-\nu)(z)R_{j\gamma}. \tag{3.7}$$

The R_j expressions are elliptic integrals taking into account the mass distribution of the ellipsoid, given in Chapter 2.

3.2.1 Jacobi Integral

With the two bodies being in relative equilibrium, this system allows for one integral of motion, the Jacobi integral. For a spacecraft navigating in this system, the Jacobi integral gives a measure of the spacecraft energy. In order to compute the integral,

let's re-write Eqs.(3.5-3.6) in the following form,

$$\ddot{x} - 2\omega\dot{y} = \frac{\partial V}{\partial x}, \tag{3.8}$$

$$\ddot{y} + 2\omega\dot{x} = \frac{\partial V}{\partial y}, \tag{3.9}$$

and

$$\ddot{z} = \frac{\partial V}{\partial z}, \tag{3.10}$$

where

$$V = -\frac{\nu}{|\boldsymbol{\rho} - \boldsymbol{r_s}|} - U_e(\boldsymbol{\rho} - \boldsymbol{r_e}) + \frac{1}{2}\omega^2(x^2 + y^2) \tag{3.11}$$

with $r_1 = \sqrt{(x - (1-\nu)r)^2 + y^2 + z^2}$ and $r_2 = \sqrt{(x + \nu r)^2 + y^2 + z^2}$.

To derive the Jacobi integral, each equation above is multiplied by $\dot{x}$, $\dot{y}$, and $\dot{(z)}$, respectively, and added to find

$$\ddot{x}\dot{x} + \ddot{y}\dot{y} + \ddot{z}\dot{z} - \omega^2(\dot{x}x + \dot{y}y) = \frac{\partial V}{\partial x}\dot{x} + \frac{\partial V}{\partial y}\dot{y} + \frac{\partial V}{\partial z}\dot{z}. \tag{3.12}$$

Substituting $\ddot{x} = \frac{d\dot{x}}{dt} = \frac{d\dot{x}}{dx}\frac{dx}{dt}$, and integrating with respect to time, Eq.(3.12) becomes,

$$C = \frac{1}{2}(\dot{x}^2 + \dot{y}^2 + \dot{z}^2) - V, \tag{3.13}$$

where C is called the Jacobi constant, the integral value of this system. Or, more generally,

$$C = \frac{1}{2}v_R^2 - V, \tag{3.14}$$

where v_R is the speed of a particle or a spacecraft relative to the rotating frame.

Relating the relative velocity to inertial velocity, the Jacobi constant is then written as,

$$C = \frac{1}{2}v_I^2 - (\boldsymbol{\omega} \times \boldsymbol{r}) \cdot \boldsymbol{v_I} - U_{12}, \tag{3.15}$$

where we have

$$\boldsymbol{v_I} = \boldsymbol{v_R} + \boldsymbol{\omega} \times \boldsymbol{r}. \tag{3.16}$$

And v_R^2 can be substituted using

$$\boldsymbol{v_R} \cdot \boldsymbol{v_R} = v_I^2 - 2(\boldsymbol{\omega} \times \boldsymbol{r}) \cdot \boldsymbol{v_I} + \omega^2(x^2 + y^2). \tag{3.17}$$

In either form, given values of the Jacobi constants, there exist constraints on the motion of a particle, starting with a study of the zero-velocity curves.

3.2.2 Zero-Velocity Curves

Computing the Jacobi integral value is also important as it can be used to indicate the regions where the spacecraft can move and provides necessary conditions for when it may escape the system. In Eq.(3.14), the solutions of $C = -V$ delineate between the allowable and non-allowable motion of a spacecraft in this gravitational field, or the zero-velocity curves. If $C \ll -1$, then $V \gg 1$, meaning x and y can be either large or very small to satisfy the relation. This restricts the motion of the spacecraft to be either far away from the bodies or very close to them. In Figure 3.3, these two cases correspond to the regions exterior to the large circular line around the bodies, referred to as the outer region, and the small circle near the bodies. Note that the small darker circle and ellipse represent the two components of the binary system. In the outer region, a spacecraft can escape from the system while in the interior region it cannot. Note also that with "mass distributions" it becomes necessary to account for impact on the surface.

Increasing the value of C allows one to define the three collinear Lagrangian points. First, the two zero-velocity curves close to each body will meet at one point on the x axis, between the bodies. This defines the L_1 Lagrangian point with its Jacobi constant, C_1, associated with it.

Then, increasing C again allows the inner region to meet with the outer region of allowable motion, on one side of the binary system and then on the other side, defining the L_2 and L_3 Lagrangian points. The point where the two regions meet

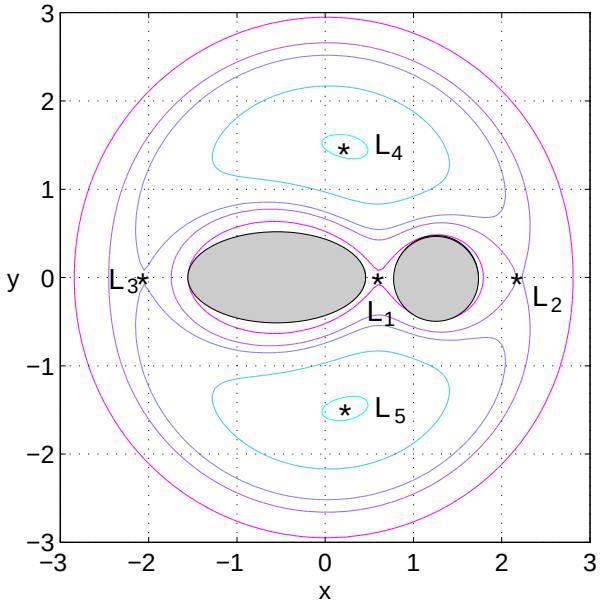

Figure 3.3: Zero-velocity curves in the x, y coordinate frame for an ellipsoid-sphere system with distance between the bodies of $r = 1.8$, ellipsoid parameters, $\alpha = 1$, $\beta = 0.5$ and $\gamma = 0.5$, and mass ratio of $\nu = 0.3$. The small darker circle and ellipse represent the bodies themselves.

first depends on the free parameters of the system. Generally, the L_2 point appears on the outer side of the smallest body. In the R3BP, the two points will appear at the same time for a mass ratio of $\nu = 0.5$. In the RF3BP, this transition depends on the distance between the bodies and the ellipsoid parameters, which is investigated in the next section. Note that the same notation on the Lagrangian points is kept throughout the text, independently of the point L_2 or L_3 appearing first. The convention on Lagrangian points is introduced in Figure 3.4.

Finally, as for the R3BP, L_4 and L_5 are defined as being the two points forming in the vicinity of the equilateral triangle points in the R3BP. Note that these two Lagrangian points are mirrors of each other about the x-axis. In general, they are stable only for very small or very large mass ratios.

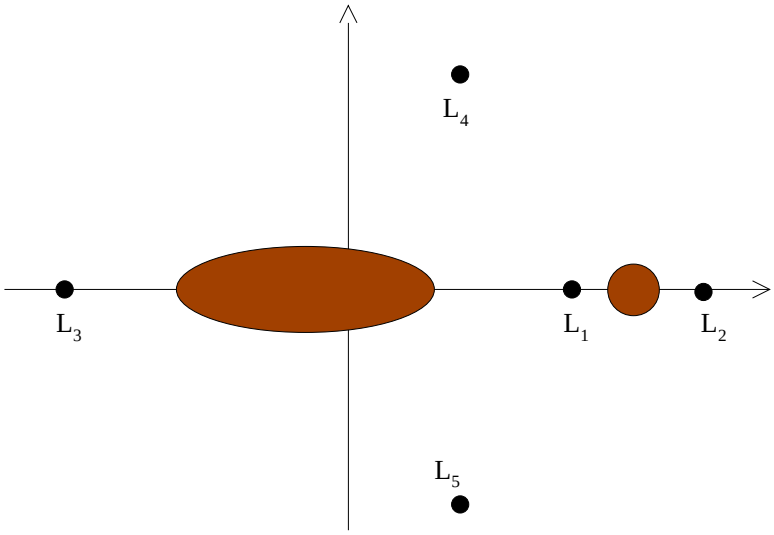

Figure 3.4: The Analogue Lagrangian Points

3.2.3 Equilibrium Solutions

As outlined in section 3.2.2, investigating the Jacobi integral allows one to find equilibrium solutions of the RF3BP, which are analogs to the Restricted Three Body Problem (R3BP). These five locations are shown qualitatively in Figure 3.4 above. These five equilibrium solutions can also be computed from the RF3BP equations of motion. Hence, when velocities and accelerations are set to zero in Eq. (3.3), the solutions are computed from

$$\boldsymbol{\omega} \times (\boldsymbol{\omega} \times \boldsymbol{\rho}) = \frac{\partial U_{12}}{\partial \boldsymbol{\rho}}. \tag{3.18}$$

In components, the equilibrium solutions are then computed from,

$$\omega^2 x = \frac{\nu(x-(1-\nu)r)}{[(x-(1-\nu)r)^2+y^2+z^2]^{\frac{3}{2}}} + (1-\nu)(x+\nu r)R_{j\alpha}, \tag{3.19}$$

$$\omega^2 y = \frac{\nu y}{[(x-(1-\nu)r)^2+y^2+z^2]^{\frac{3}{2}}} + (1-\nu)yR_{j\beta}, \tag{3.20}$$

$$0 = \frac{\nu z}{[(x-(1-\nu)r)^2+y^2+z^2]^{\frac{3}{2}}} + (1-\nu)(z)R_{j\gamma}, \tag{3.21}$$

where ω is given by Eq. (2.27). By setting $z = 0$ and $y = 0$, the solutions for x correspond to the three collinear points. As for the R3BP, these points remain unstable as the potential will be a saddle at each point. However, for the purpose of surface exploration and mission design, there are some key observations that can be made.

First, the ellipsoid having a finite size adds one interesting constraint on the location of the L_1 point. The L_1 point defines the limit between the two gravitational fields for the binary system, also called the Roche limit. The region around each body is defined as the Roche lobe. Section 3.2.8 discusses possible exchange of material through depending on the location of L_1 (for an illustrative example see [20]). The limiting case is when L_1 sits on the ellipsoid, facing the sphere. Figure 3.5 provides a closer view of this situation. In this case, the location of L_1 can be written as

$$x_{L_1} = 1 - \nu r. \tag{3.22}$$

Substituting x_{L_1} with $y = z = 0$ into Eq. (3.19) and solving for the mass ratio as a function of the distance between the bodies, r give

$$\nu = \frac{\omega^2 - I(q)}{(\omega^2 r - \frac{1}{(r-1)^2} - I(q))}. \tag{3.23}$$

Note that the spin rate ω is given by the F2BP, Eq. (2.27).

Hence, given a value of the distance between the bodies, Eq. (3.23) gives the corresponding mass ratio in order to have L_1 sitting on the edge of the ellipsoid, facing the sphere. Depending on the system parameters, L_1 can be either inside or outside of the ellipsoidal body. Figure 3.6 shows the mass ratio as a function of the distance between the primaries satisfying Eq. (3.23). The upper region of the curve defines the parameters for which L_1 is outside of the ellipsoid; the lower region represents cases of L_1 being inside the ellipsoid. A variety of trajectories can be computed for motion in the vicinity of L_1, and they are addressed in the following

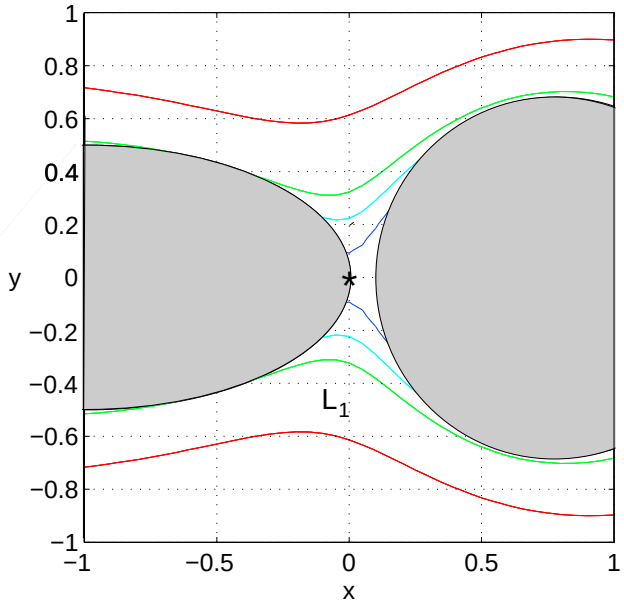

Figure 3.5: Close view of the zero-velocity curves for an ellipsoid-sphere system where L_1 is sitting on the ellipsoid surface, facing the sphere. The system parameters is at $r = 1.8$, with $\nu = 0.5586$, and $\beta = \gamma = 0.5$ for the ellipsoid. The shaded regions represent the bodies themselves.

section.

The primary interest in L_2 and L_3 is to investigate the free parameters that give a transition between the point opening first. Since the R3BP is modeled with two spherical primaries, the L_2-L_3 transition happens at $\nu = 0.5$ always. In the RF3BP, for given values of the distance between the primaries and ellipsoid parameters, varying the mass ratio from having a large ellipsoid to a small one, the L_2-L_3 transition shifts towards smaller mass ratios. Figure 3.7 gives an example for $r = 2$ and $\beta = 2\gamma = 0.5$, where the Jacobi values of L_2 and L_3 are plotted as a function of the mass ratio. In this case, at $\nu = 0.42$, L_3 has a smaller Jacobi constant making it appear first over L_2. Varying the other free parameters, it is found that this transition point gets even lower as either the ellipsoid parameters or the distance between the primaries are reduced. At a close distance, say $r = 1.5$, L_2-L_3 transitions at $\nu = 0.36$. This indicates that, preserving the Lagrangian point notation as defined in Figure 3.4, L_3 opens first for small ellipsoid, or large mass

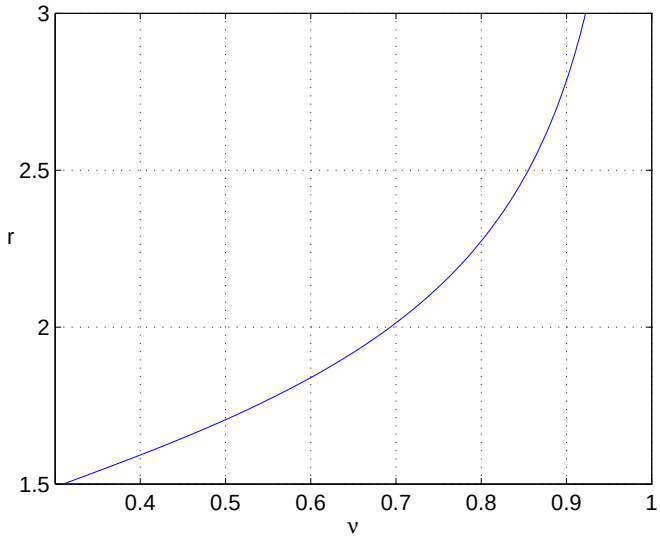

Figure 3.6: Values of the distance between the bodies, r, as a function of the mass ratio ν to have the L_1 Lagrangian point sitting on the ellipsoid body, facing the sphere. The ellipsoid parameters are $[\alpha : \beta : \gamma] = [1 : 0.5 : 0.5]$.

ratio, for up to 20% more compared to the R3BP. As some of the binary systems are made of a small ellipsoidal body and a large sphere, L_3 on the outer side of the ellipsoid can be the unique entry and exit point for particles or spacecraft, which may make it an interesting scientific location to investigate first.

The two "equilateral points" L_4 and L_5 are of interest as they can potentially be used for observation and scientific purposes. Their stability will be affected by the properties of the general body and the system parameters such as the mass ratio and the distance between the bodies. For the long-axis configuration, Figure 3.8 shows the locations of the analogue equilateral points and their stability as the ellipsoid goes from being spherical to highly oblate and as it becomes massively dominant. The normalized distance is $r = 2$. In this figure, the mass ratio ν varies from 0 to 1 horizontally from left to right and $\gamma = \beta$ varies from 0 to 1 vertically from bottom to top. These plots have been shifted by $r\nu$ and scaled by $1/r$ so that the ellipsoid is located at the origin and the sphere at a distance of 1 from it. Starred points are stable while dotted ones are unstable. Note that the stability methods used are

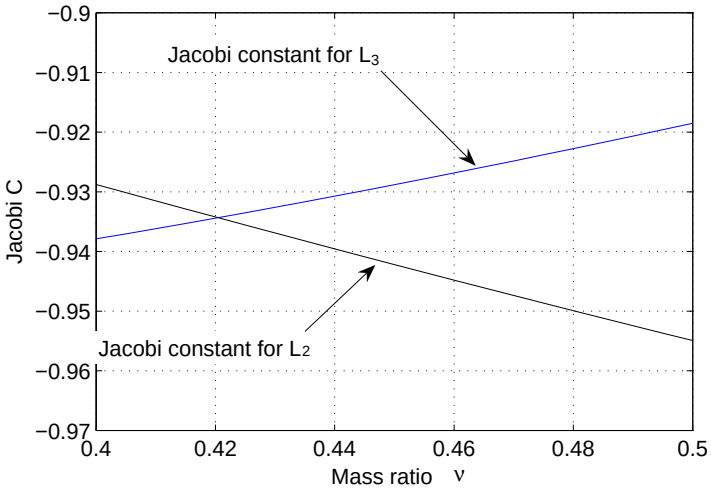

Figure 3.7: Jacobi constant for L_2 and L_3 as function of the mass ratio ν for $r = 2$ and $[\alpha : \beta : \gamma] = [1 : 0.5 : 0.5]$. The L_2-L_3 transition happens at $\nu = 0.42$.

further explained in the next section.

The effect of the ellipsoid is easily noticed by considering $\nu = 0$ (when the ellipsoid is the sole attractor) and $\nu = 1$ (when the sphere has all the mass). In the first case, we find the equilibrium solutions lie along the intermediate axis of the ellipsoid. For $\nu = 1$ and $\gamma = \beta = 1$, the ellipsoid has no effect and, as for the ideal solutions of the R3BP, all points are located at $x = 0.5$ and $y = \sqrt{3}/2$ as expected for this shifted system. For $\gamma = \beta < 1$, they are not located at the known Lagrangian points as the rotation rate is different than the normal Keplerian rotation rate of the R3BP, due to the non-spherical body.

Similar results were found for the short-axis configuration (see Figure 2.5). They are shown in Figure 3.9 for $r = 2$ with the same normalization as for the long-axis configuration. However, as opposed to this case, the mass ratio ν varies from 0 to 1 horizontally from right to left and $\gamma = \beta$ varies from 0 to 1 vertically from top to bottom. For $\nu = 0$ and smaller β, the equilibrium points are unstable on the y axis. Note that the distribution of the equilibrium points is markedly different for

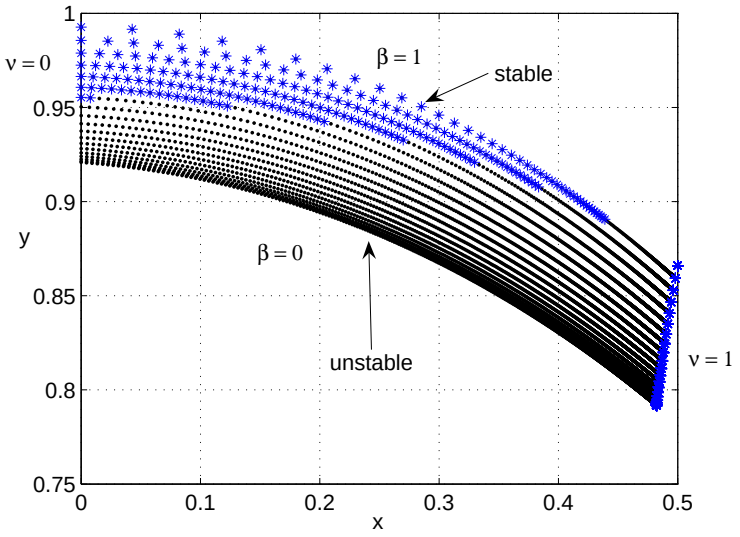

Figure 3.8: Locations of the analogue equilibrium points for $r = 2$ in the x-y coordinate space for the long-axis configuration. The mass ratio ν varies from 0 to 1 horizontally from left to right and $\gamma = \beta$ varies from 0 to 1 vertically from bottom to top. Starred points are stable while dotted ones are unstable.

this case, and that the stability intervals are highly constrained. However, as for the long-axis configuration, for $\nu = 1$ and $\gamma = \beta = 1$, the solutions agree with those of the R3BP.

3.2.4 Stability of the Equilibrium Solutions

As for the R3BP, for all values of the free parameters, L_1, L_2 and L_3 are unstable while $L_{4,5}$ may be stable. Looking at small deviations from the equilateral position, we can investigate their stability. In the R3BP, the stability criteria for $L_{4,5}$ is usually given by the Routh criteria and is only function of the mass ratio,

$$\nu < \frac{1}{2}\left[1 - \sqrt{\frac{23}{27}}\right] = 0.0385... \tag{3.24}$$

Since the mass distribution of the general body is now taken into account, the stability of some of the equilibrium solutions are expected to deviate from the R3BP. Using perturbations to x and y, $x = \tilde{x} + dx$ and $y = \tilde{y} + dy$, the potential energy

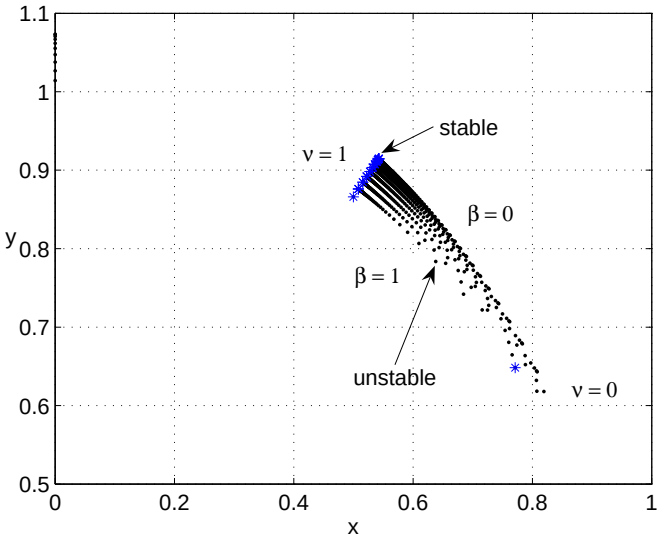

Figure 3.9: Locations of the analogue equilibrium points for $r = 2$ in the x-y coordinate space for the short-axis configuration. The mass ratio ν varies from 0 to 1 horizontally from right to left and $\gamma = \beta$ varies from 0 to 1 vertically from top to bottom. Starred points are stable while dotted ones are unstable.

expression is expanded giving the following equations,

$$\ddot{\tilde{x}} - 2\omega\dot{\tilde{y}} - \omega^2\tilde{x} = \tilde{x}(U_{xxs} + U_{xxe}) + \tilde{y}(U_{xys} + U_{xye}) \tag{3.25}$$

and

$$\ddot{\tilde{y}} + 2\omega\dot{\tilde{x}} - \omega^2\tilde{y} = \tilde{y}(U_{yys} + U_{yye}) + \tilde{x}(U_{yxs} + U_{yxe}). \tag{3.26}$$

The second order partial derivatives for the ellipsoid potential were given in Chapter 2. The characteristic equation for the system is found from,

$$\begin{vmatrix} \lambda^2 - \omega^2 - U_{xx} & -2\omega\lambda - U_{xy} \\ 2\omega\lambda - U_{xy} & \lambda^2 - \omega^2 - U_{yy} \end{vmatrix} = 0, \tag{3.27}$$

where $U_{xx} = U_{xxs} + U_{xxe}$, $U_{yy} = U_{yys} + U_{yye}$ and $U_{xy} = U_{xys} + U_{xye}$. Expanding the determinant, the characteristic equation can also be written in the form,

$$\lambda^4 + A\lambda^2 + B = 0, \tag{3.28}$$

where

$$A = 2\omega^2 - U_{xx} - U_{yy} \tag{3.29}$$

and

$$B = \omega^4 + \omega^2(U_{xx} + U_{yy}) + U_{xx}U_{yy} - {U_{xy}}^2. \tag{3.30}$$

For the system to be linearly stable, the following conditions must be satisfied,

$$A > 0 \tag{3.31}$$

$$B > 0 \tag{3.32}$$

$$A^2 - 4B > 0. \tag{3.33}$$

The long-axis case is shown in Figure 3.10, for a distance between the two bodies set as $r = 2$ while varying the ellipsoid parameters α and β. The stability was found to be decreased from the known R3BP. In Figure 3.10, each line corresponds to different values of γ/β, and equal 0.25, 0.5, 0.75 and 1.0. Stable regions lie above the lines in the upper figure and below the lines in the lower figure. The horizontal dotted line corresponds to the Routh criterion. It is easy to see that the stability region is reduced from the R3BP although exceptions exist for small mass ratios. In the case of a short-axis configuration, the stability region is even further reduced, as shown in Figure 3.11. Note that $r = 2$ also in this figure.

Finally, as the distance between the two binary bodies is increased, the stability of the RF3BP merges with the one for the known R3BP, as shown in Figures 3.12 and 3.13, for the long and short-axis configurations, respectively.

Note on the stability in the F2BP and the RF3BP

It is interesting to compare the results from the RF3BP with the stability in the F2BP. For the long-axis configuration, as the distance r between the bodies increases, the F2BP becomes more and more stable. For the short-axis configuration, it was shown in [79] that the F2BP is usually unstable with some exceptions for small ν

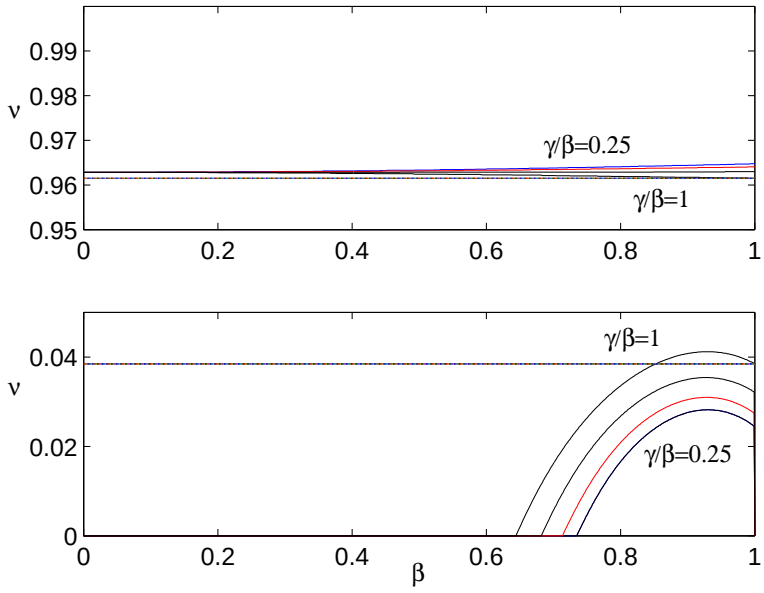

Figure 3.10: Stability regions of the long-axis configuration for $r = 2$ as a function of β and ν. Each line corresponds to different values of γ/β, and equal 0.25, 0.5, 0.75 and 1.0. Stable regions lie above the lines in the upper figure and below the lines in the lower figure. The horizontal dotted line corresponds to the Routh criterion.

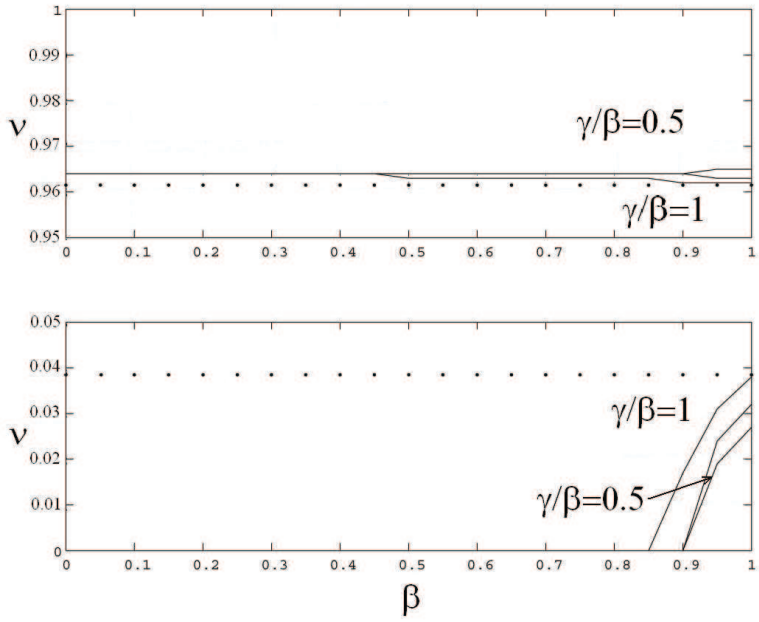

Figure 3.11: Stability regions of the short-axis configuration for $r = 2$ as a function of β and ν. Each line corresponds to different values of γ/β, and equal 0.5, 0.75 and 1.0. Stable regions lie above the lines in the upper figure and below the lines in the lower figure. The horizontal dotted line corresponds to the Routh criterion.

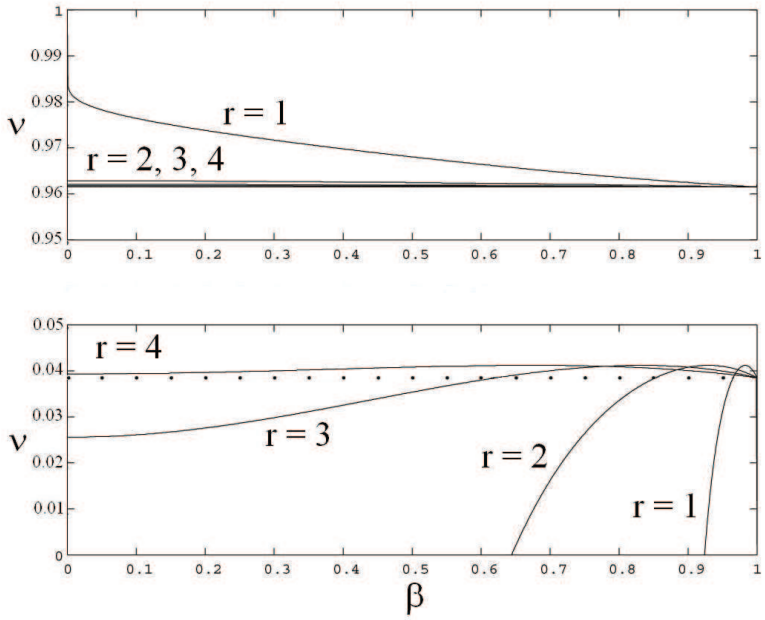

Figure 3.12: Stability regions of the long-axis configuration for $\gamma/\beta = 1$ as a function of β and ν. The lines correspond to different values of r, and equal 2, 3, and 4. Stable regions lie above the lines in the upper figure and below the lines in the lower figure. The horizontal dotted line corresponds to the Routh criterion.

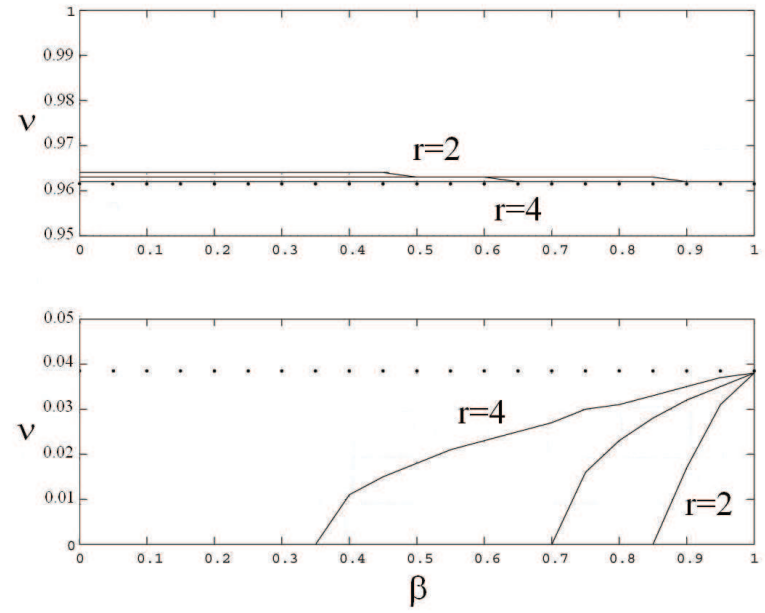

Figure 3.13: Stability regions of the short-axis configuration for $\gamma/\beta = 1$ as a function of β and ν. The lines correspond to different values of r, and equal 2, 3, and 4. Stable regions lie above the lines in the upper figure and below the lines in the lower figure. The horizontal dotted line corresponds to the Routh criterion.

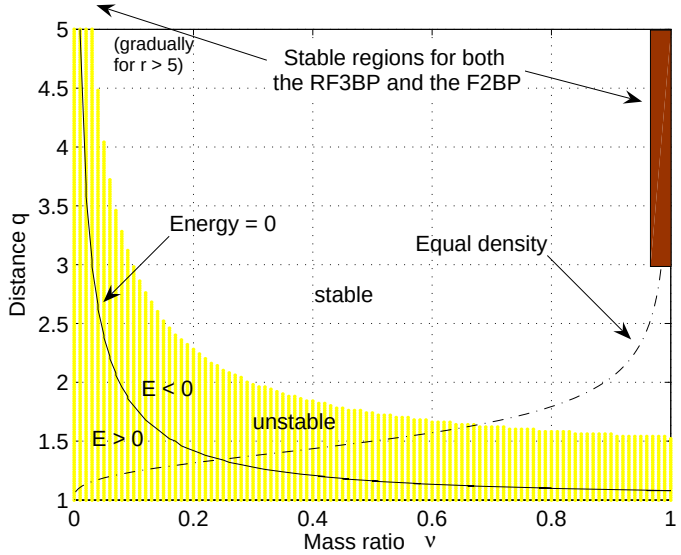

Figure 3.14: Stability diagram for planar motion in the long-axis configuration, showing common regions of stability in the F2BP and in the RF3BP, where the distance between the bodies is plotted as function of the system mass ratio. The clear region denotes spectral stability while the shaded one denotes spectral instability. The solid line indicates transition from positive to negative total energy of the system and the pointed dashed line assumes equal density of the binary bodies. Parameters are $\alpha = 1$, $\beta = 0.5$, $\gamma = 0.25$.

and large r.

Now, in the RF3BP, for the long-axis configuration, the standard R3BP Routh criteria is recovered for r larger than 3 and large mass ratio, ν, that is, the system having a massive sphere. In this case, the F2BP is generally stable. When the primary is of an ellipsoidal shape, i.e., for small ν, r needs to be larger than 5 to have both systems stable. The common regions for both the F2BP and the RF3BP are shown in Figure 3.14. Although not shown, for the short-axis case, interestingly, stability of both the F2BP and the RF3BP is only possible for small ν and r larger than 5.

An extension to this is to investigate the transfer properties and stability of the ellipsoid-sphere system when L_1 sits on the ellipsoid. This topic is introduced in the following sections, 3.2.5-3.2.8.

3.2.5 Transition Trajectory near L_1

Motivational Background

A future mission to a binary system may want to carry out surface motion for scientific investigations or sample return objectives. Other than surface and gravity constraints, situations such as the body spin rates need to be taken into account. In terms of mission design, for a small ellipsoid case, it would be interesting to have a vehicle approaching a binary system from the small ellipsoid body, through L_3, as the primary is often spinning more rapidly than the orbit rate[87]. Given a value of the Jacobi integral, the spacecraft would have enough energy to travel close to the system, visiting both bodies, without escaping through the L_3 region. Hence, it is important to look into possible mission scenarios and to characterize the surface conditions and requirements for possible transit trajectories between the bodies.

For certain parameters of the system, L_1 is on the outside of the ellipsoid, providing a channel for possible transit trajectories. However, due to the instability of L_1, only certain conditions on the position and velocity of a spacecraft can lead to transit. Moreover, certain velocity limits are required in order to prevent a vehicle from escaping the system.

Linearization at L_1

Different trajectories such as transit and non-transit trajectories between the bodies can be analyzed from linearizing near L_1 and computing its manifolds. In the following the methodology of Conley [14] is applied to the current problem. This is possible by investigating the eigenvalues and eigenvectors of the state transition matrix evaluated about L_1. The L_1 equilibrium point has one pair of real and one pair of imaginary conjugate eigenvalues. The corresponding eigenvectors, one pair of hyperbolic manifolds and one center manifold, respectively, make L_1 unstable.

To find the manifolds at L_1, it is necessary to first compute the eigenvalues of the

linearized dynamics. For a system of the form $\dot{x} = F(x,t)$, the linearized equations are computed using the first derivative of $F(x,t)$, that is $\frac{\partial F}{\partial x}$. For the dynamics defined by Eqs. (3.5,3.6), $\frac{\partial F}{\partial x}$ is expressed as

$$\frac{\partial F}{\partial x} = \begin{bmatrix} 0 & 0 & 1 & 0 \\ 0 & 0 & 0 & 1 \\ \omega^2 + (U_{xxs} + U_{xxe}) & (U_{xys} + U_{xye}) & 0 & 2\omega \\ (U_{xys} + U_{xye}) & \omega^2 + (U_{yys} + U_{yye}) & -2\omega & 0 \end{bmatrix}. \tag{3.34}$$

Note that the second order derivatives for the sphere and ellipsoid potential are given in Chapter 2.

Because of the nature of L_1, the eigenvalues can be written as $\pm\lambda_1$ and $\pm\lambda_2$, where λ_1 is real and λ_2 is imaginary. The associated eigenvectors are $\boldsymbol{\mu_1}^{\pm}$ and $\boldsymbol{\mu_2} = \boldsymbol{\mu_2}^{\boldsymbol{RE}} + \mathrm{i}\boldsymbol{\mu_2}^{\boldsymbol{I}}$. The solution for the particle dynamics can be written as a superposition of the eigenvectors,

$$\boldsymbol{q} = \alpha^{+}\boldsymbol{\mu_1}^{+}e^{(\lambda_1 t)} + \alpha^{-}\boldsymbol{\mu_1}^{-}e^{(-\lambda_1 t)} + 2Re(\beta\boldsymbol{\mu_2}e^{(i\lambda_2 t)}), \tag{3.35}$$

where α^{+}, α^{-} and β are constants.

Now, let's substitute

$$\beta = \beta^{Re} + i\beta^{I} \tag{3.36}$$

and

$$e^{(i\lambda_2 t)} = \cos(\lambda_2 t) + i\sin(\lambda_2 t). \tag{3.37}$$

Equation (3.35) then becomes

$$\begin{aligned} \boldsymbol{q} =& \alpha^{+}\boldsymbol{\mu_1}^{+}e^{(\lambda_1 t)} + \alpha^{-}\boldsymbol{\mu_1}^{-}e^{(-\lambda_1 t)} \\ &+ 2\beta^{Re}(\boldsymbol{\mu_2}^{\boldsymbol{Re}}\cos(\lambda_2 t) - \boldsymbol{\mu_2}^{\boldsymbol{I}}\sin(\lambda_2 t)) - 2\beta^{I}(\boldsymbol{\mu_2}^{\boldsymbol{Re}}\sin(\lambda_2 t) + \boldsymbol{\mu_2}^{\boldsymbol{I}}\cos(\lambda_2 t)). \end{aligned} \tag{3.38}$$

Subsituting $t = 0$ in Eq.(3.38) gives

$$\boldsymbol{q} = [\boldsymbol{\mu_1^+}, \boldsymbol{\mu_1^-}, \boldsymbol{2\mu_2^{Re}}, \boldsymbol{-2\mu_2^I}] \begin{bmatrix} \alpha^+ \\ \alpha^- \\ \beta^{Re} \\ \beta^I \end{bmatrix}. \tag{3.39}$$

Then, writing Eq.(3.39) in the form $\boldsymbol{q} = [\boldsymbol{\mu}]\boldsymbol{\alpha_\mu}$, the components of $\boldsymbol{\alpha_\mu}$ are found from,

$$\boldsymbol{\alpha_\mu} = [\boldsymbol{\mu}]^{-1}\boldsymbol{q}. \tag{3.40}$$

Having the constant α^+, α^-, β^{Re} and β^I, trajectories of a particle near the L_1 Lagrangian point can be investigated from its linear dynamics. Depending on the value of α^+ and α^-, the system will excite different manifolds, leading to different types of trajectories. As shown in Figure 3.15, there are three cases to consider, transit trajectories, non-transit trajectories and asymptotic trajectories, respectively, with

$$\alpha^+\alpha^- < 0, \tag{3.41}$$

$$\alpha^+\alpha^- > 0, \tag{3.42}$$

and

$$\alpha^+\alpha^- = 0 \tag{3.43}$$

In order to find regions allowing transit and non-transit trajectories, the α constants were computed along the y-axis of the L_1 point with varying the direction of the velocity vector. The geometry is sketched in Figure 3.16. Results on the trajectories are shown in Figure 3.17. The dark and white region represents non-transit and transit trajectories, respectively, for a system with $r = 2$, $\beta = \gamma = 0.5$ and $\nu = 0.3$, and for an interval on the y axis of $[-0.5, 0.5]$.

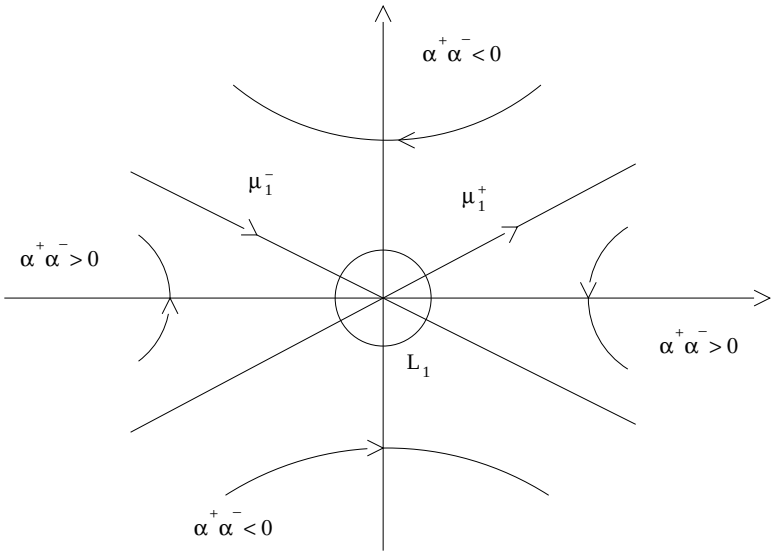

Figure 3.15: Transit and non-transit trajectory regions at L_1.

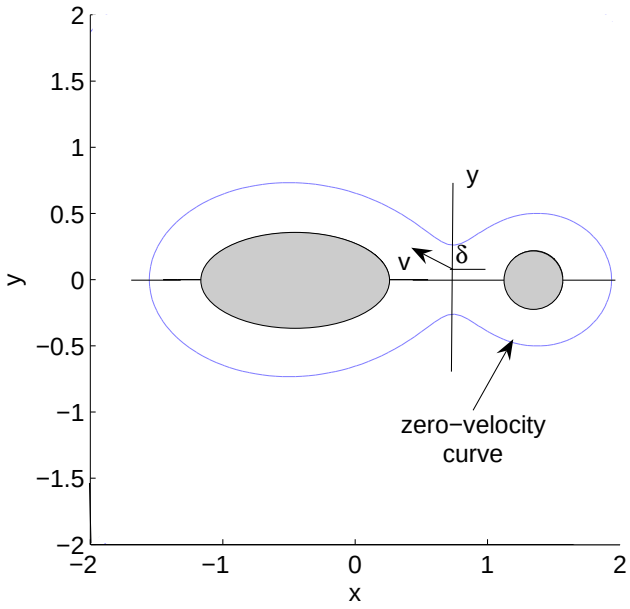

Figure 3.16: Geometry of the transit/non-transit trajectories investigation at L_1 when it is outside of the ellipsoid body.

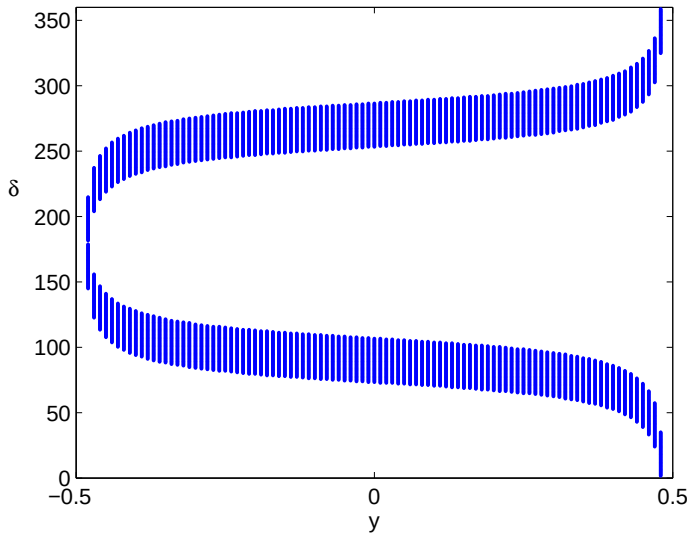

Figure 3.17: Results on transit and non-transit trajectories at L_1 for $r = 2$, $\beta = \gamma = 0.5$ and $\nu = 0.3$ across $y = [-0.5 : 0.5]$. The dark region indicates non-transit trajectories.

Finally, note that the condition

$$\alpha^+ \alpha^- = 0 \tag{3.44}$$

gives small unstable periodic orbits around L_1, shown in Figure 3.18. In this figure, $r = 1.8$, $\beta = \gamma = 0.5$ and $\nu = 0.3$ in nondimensional units.

3.2.6 Surface Conditions Leading to Transit and Non-Transit Trajectories

Knowing the conditions giving transit and non-transit trajectories from linear investigation at L_1, the system can be integrated backward and forward in time to find initial and final conditions of the particle dynamics on the surface of either body. From the results on transit and non-transit trajectories shown in Figure 3.17, the surface conditions for transit trajectories were studied. Figure 3.19 shows a typical non-transit trajectory for parameter $r = 2$, $\beta = \gamma = 0.5$ and $\nu = 0.3$ and two transit trajectories in the center and outer regions of the surface of the bodies. The small arrows show the locus of transit trajectory surface conditions; the region facing the

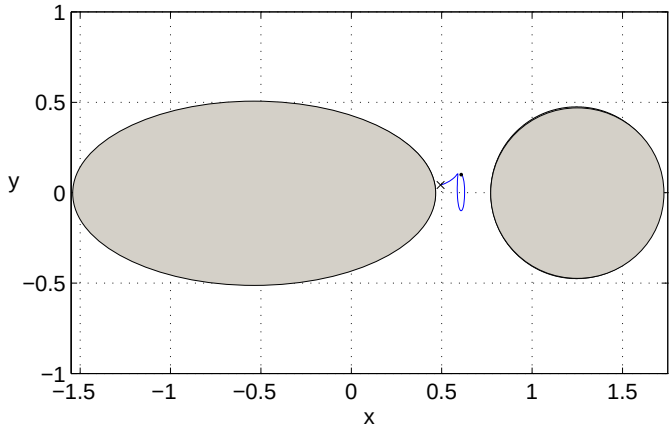

Figure 3.18: Unstable periodic orbit around L_1 due to the hyperbolic manifold at L_1, satisfying the asymptotic condition. Parameters are $r = 1.8$, $\beta = \gamma = 0.5$ and $\nu = 0.3$. The shaded regions represent the bodies themselves.

bodies gives more transfer options while the conditions need to be more precise for the outer regions on the surface.

Different conditions were investigated for transit and non-transit trajectories crossing the L_1 region. The point **A** in Figure 3.20a represents a fixed value on the y axis at L_1 through which trajectories are crossing with varying directions δ defined in Figure 3.16. We see that the corresponding surface conditions and nature of the trajectories differ widely while attempting to cross the L_1 region. Figure 3.20b shows different initial velocity vectors for a vehicle leaving from the surface of the ellipsoid at **B**. In this case, the direction of the launching velocity at the surface was varied while the initial surface location and the velocity magnitude were fixed. It can be seen that small differences in angle could lead to transfer or not. We also note that some initial conditions may lead to transfer to the back side of the spherical body.

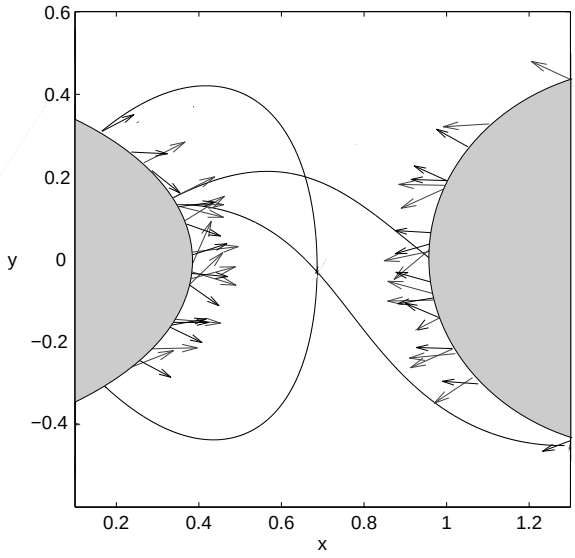

Figure 3.19: Transit and non-transit trajectories for a binary system with $r = 2$, $\nu = 0.3$ and ellipsoid parameters $\beta = \gamma = 0.5$. The arrows are initial and final conditions on the surface of the bodies leading to transit trajectories.

3.2.7 Bounds on Transfer Velocity

To keep the spacecraft close to the bodies, attention is needed to monitor the velocity involved in transferring from the ellipsoid to the sphere. Getting to an large orbit encircling the binary system would make a spacecraft more susceptible to escape. Given a Jacobi integral value, conditions on the velocity can be computed to make sure a spacecraft would not be able to escape from the system. Using these conditions, it is possible then to perform the necessary maneuvers in order to satisfy the surface conditions leading to transit without possibilities of escaping.

Knowing that a spacecraft with enough energy could have access to the outer region of the binary system by leaving through the L_2 or L_3 region, upper bounds on the transit velocity are computed from their Jacobi integral values, C_2 and C_3 respectively. For the spacecraft being close to the back side of the ellipsoid, an energy value close to C_3 would be a good upper bound as L_3 opens first. If the spacecraft makes a transfer to the spinning sphere, an energy value larger than C_2

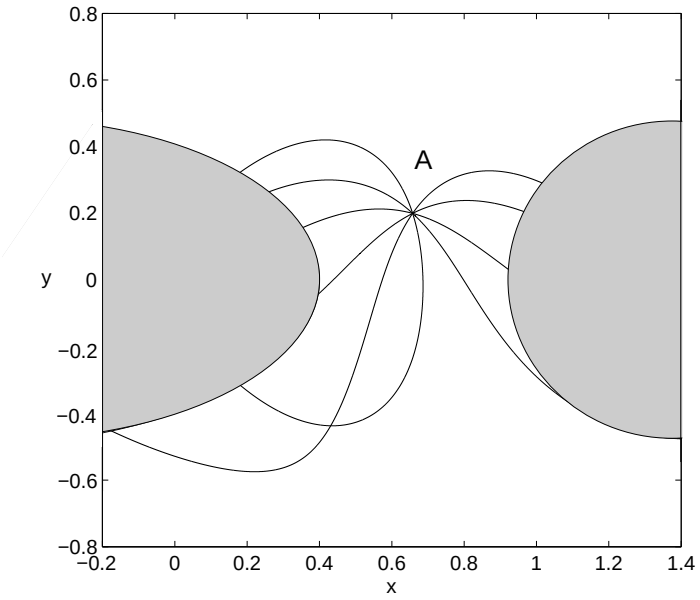

(a)

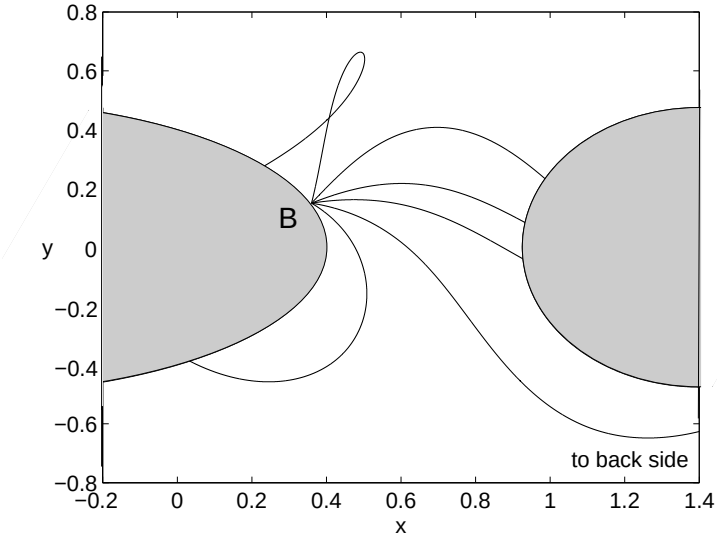

(b)

Figure 3.20: Transit and non-transit trajectories for a binary system with $r = 2$, $\nu = 0.3$ and ellipsoid parameters $\beta = \gamma = 0.5$. a) The point A represents trajectories crossing L_1 at fixed value of y, $y = 0.1$, with varying direction δ. b) The point B indicates different initial directions of launching velocities for a spacecraft leaving the surface of the ellipsoid.

might be more suitable, depending on the mass ratio.

Hence, in the design of a mission approaching by the ellipsoid side, say, and transferring to the sphere, a value of energy larger than C_2 corresponding to an orbit encircling the binary can be chosen as an upper bound on the spacecraft velocity. It is referred to as the outer region with a value C_{outer} corresponding to its Jacobi value. Given a value of C_{outer}, Eq.(3.14) is reversed to obtain the corresponding velocity at the specific location on a body surface, and set it as $\boldsymbol{v_{max}}$. This gives a bound on the velocity for the spacecraft to stay in orbit close to the binary system. The velocity correction for the spacecraft leaving the surface of the ellipsoid with a velocity $\boldsymbol{v_{sfc}}$ can be found from,

$$\triangle \boldsymbol{v} = \boldsymbol{v_{max}} - \boldsymbol{v_{sfc}}. \tag{3.45}$$

In the case of a spinning spherical primary with a spin rate given by Ω_α, a vehicle on a spherical surface of radius r_{sfc} would have a tangential velocity component given by,

$$\boldsymbol{v_T} = (\boldsymbol{\Omega} - \boldsymbol{\Omega_\alpha})\boldsymbol{r_{sfc}}. \tag{3.46}$$

Note that the sphere spin Ω_α is usually faster than the binary orbit rate Ω, and that the Jacobi integral is not constant anymore. The transit velocity on the surface of the sphere with respect to the binary system is then,

$$\boldsymbol{v_{Transit}} = \boldsymbol{v_T} + \boldsymbol{v_{sfc}}. \tag{3.47}$$

From the results on the surface conditions given by Figure 3.19, a vehicle would only need to hop in the right direction to bring the total launch velocity to the required magnitude and direction for transit. It is necessary to make sure that the energy of the spacecraft stays low enough when it hits the spinning sphere. Hence, arriving at the sphere the velocity can be monitored using Eq. (3.45) and the necessary maneuvers can be performed.

Note that these velocity bounds are defined for L_1 located between the two bodies, outside of their physical shape. For a system with the two primaries being closer to each other, the velocity limits will vary with the Jacobi integral, and if L_1 is located within one of the two bodies. This case also indicate possible material exchange between the bodies, which is discussed next.

3.2.8 Dynamical Evolution and Momentum Transfer for Binary Asteroid Systems

The results on relative equilibria combined with analysis of the dynamics of particles in the vicinity of such binary system situation provide insights on mass and momentum exchange that may occur between the two bodies. Since the mass distribution of one of the bodies is now taken into account, L_1 is a key element for transfers between the bodies. It was shown in section 3.2.3 that L_1 can be situated between or inside the bodies depending on the free parameters of the system modifying the transfer possibilities.

Equation (3.23) plotted in Figure 3.21 shows the distance between the primaries r as a function of the mass ratio ν in order to have L_1 sitting on the ellipsoid facing the sphere. The region above the solid line defines the parameters for which L_1 is outside the ellipsoid; the region below the solid line represents cases of L_1 being inside the ellipsoid.

A reasonable assumption for binary systems is that they have the same density between the two bodies, as the two binaries may have formed from a single one. To provide a better physical insight it is useful to compare the results of having L_1 sitting on the ellipsoid given above to the case of equal density between the two bodies. First, let's expand on an equal density binary system. The definition of the mass ratio, ν, gives

$$\nu = \frac{M_1}{(M_1 + M_2)} = \frac{\frac{4\pi}{3}\rho R_s^3}{\frac{4\pi}{3}\rho(R_s^3 + \alpha\beta\gamma)}, \tag{3.48}$$

where R_s is the radius of the sphere. Solving for R_s gives

$$R_s = \left[\alpha\beta\gamma\left(\frac{\nu}{1-\nu}\right)\right]^{\frac{1}{3}}. \tag{3.49}$$

Since the distance between the bodies can vary, and hence the location of L_1, the simplest situation is to have the two bodies stay in contact with each other. Then the distance between them can be varied. Here, with $\alpha = 1$ from the normalization used, the distance between the bodies is denoted as R and written as,

$$R = 1 + R_s. \tag{3.50}$$

Substituting R_s from Eq. (3.49) into Eq. (3.50), the distance between the bodies can be expressed as

$$R = 1 + \left[\beta\gamma\left(\frac{\nu}{1-\nu}\right)\right]^{\frac{1}{3}}. \tag{3.51}$$

Equation (3.51) is the dashed line plotted in Figure 3.21, that is the distance R as a function of the mass ratio ν.

From Eqs. (3.51) and (3.23), the conditions are found for L_1 to be inside or outside of a binary system with equal density. Given a value of the distance between the two bodies, r, the value of the mass ratio required to have L_1 touching the ellipsoid is computed from Eq. (3.23). Using this same mass ratio in Eq. (3.51), the corresponding distance R between two bodies with the same density can then be calculated. The meeting point in Figure 3.21 indicates that L_1 is sitting on the ellipsoid for a case of equal density, which occurs for $r = 1.22$ and $\nu = 0.08$. Note that, in this simple case, the sphere is also touching the ellipsoid. As the ellipsoid parameter β increases, this transition limit is shifted up.

In Figure 3.21, the region below the solid line indicates that $r < R$ meaning L_1 would be located inside the ellipsoid if the bodies were to be of equal density and resting on each other. In the region above the solid line, $r > R$ and L_1 is in the exterior region of the ellipsoid. As the distance between the bodies increases, the

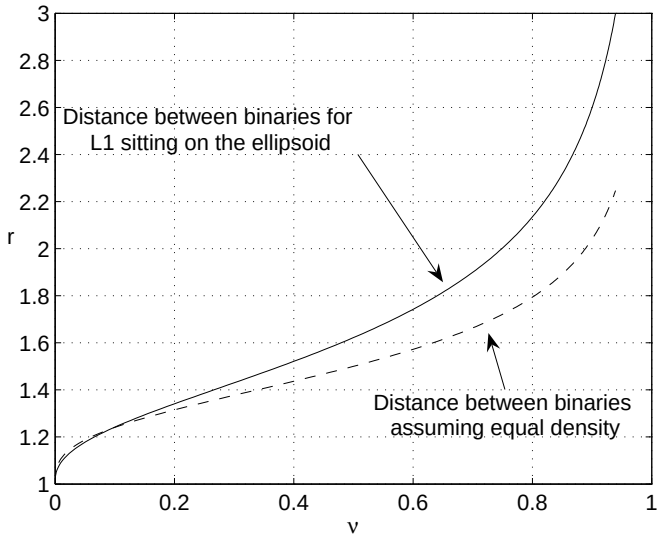

Figure 3.21: Equations (3.51-3.23) are plotted together. The dash line represents the value of the two body distance for the case of constant density with the two bodies in contact. The solid line represents the locus of the mass ratio ν and the distance r between the bodies for L_1 to be sitting on the ellipsoid, facing the sphere. For an equal density binary, the transition for L_1 from inside to outside the ellipsoid happens at $r = 1.22$, $\nu = 0.08$. Ellipsoidal parameters are $[\alpha : \beta : \gamma] = [1 : 0.5 : 0.25]$.

path from the sphere to the ellipsoid would be open to particles leaving one of the body. The connecting region is found from computing the zero-velocity limits on the spherical body given a value for the Jacobi integral. Then, the conditions allowing particles to transit from one body to the other are computed using the method from section 3.2.5.

Finally, this topic on L_1 can be related to the relative equilibria cases at the end of chapter 2. In the case of equal density of the binary bodies, for lower mass ratios, L_1 is inside the ellipsoid for the unstable equilibrium configuration while it is located between the bodies for the conjugate binary equilibrium configuration. As the mass ratio of the binary system is increased, L_1 slowly gets closer to the ellipsoid. The L_1 transition from outside to inside the ellipsoid happens for a mass ratio of $\nu = 0.6$. Note that this L_1 transition is slightly different than the equilibrium configuration bifurcation of $\nu = 0.68$, as shown in Figure 2.10.

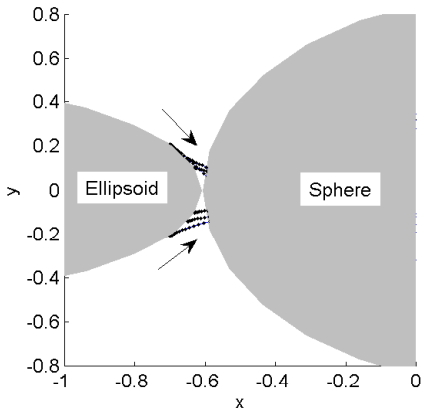

Figure 3.22: Dynamics of particles close to the point of contact of a binary system where L_1 is situated inside the ellipsoid. The arrows show the direction of motion when the particles are released on the surface of the ellipsoid.

This can be related to the Roche limit and the Roche lobe of binaries which affect the distribution of mass between the bodies. For a binary system, the Roche limit is the location where the net gravitational field of the two bodies meet, which is L_1. The Roche lobe is the region around the body within which orbital particles are gravitationally bound to that body. If the bodies overflow its Roche lobe, some material will most likely start "falling" into the other body. For binary systems in close proximity with L_1 being inside the bodies such as the case pictured in Figure 3.22, simulations show that particles on the surface tend to move toward the spherical primary. In this case, L_1 is inside the ellipsoid. The system mass ratio is 0.85 and the bodies are 1.9 units apart.The equilibrium configuration is stable in this case.

Starting from the Hill approximation [15, 91], the Hill sphere distance can be stated as

$$x = \pm \left(\frac{\mu_2}{3\mu_1} \right)^{1/3} r, \tag{3.52}$$

where μ_1 and μ_{sys} are the gravitational constant of the primary and secondary

bodies, and r is the distance between the two bodies. With the ratio of gravitational parameters expressed as

$$\frac{\mu_2}{\mu_1} \approx \left(\frac{r_1^3}{r_L^3 + r_1^3} \right), \tag{3.53}$$

where r_1 is the radius of the primary, at the limit, Eq. (3.52) is written as

$$x = \frac{r_1 r}{(3(r_L^3 + r_1^3))^{1/3}} \approx \frac{r_1 r}{3^{1/3} r_L}. \tag{3.54}$$

Hence, the system becomes unstable if $x \to r_1$. Hence, if r_L denotes the Roche limit, then the system becomes unstable if

$$\frac{r_L}{r} \approx \frac{1}{3^{1/3}}. \tag{3.55}$$

Other parameters such as the spin of a larger spherical primary may also influence particle distribution near the point of contact of binary bodies. In addition, looking at the angular momentum and energy properties for relative equilibria, as given in Figure 2.8 of section 2.4.1, one can map and characterize the mass distribution and momentum exchange that may occur within a closely formed binary system.

3.2.9 Reconnaissance Periodic Orbits

For systems where the F2BP is under a relative equilibrium assumption, it is possible to investigate orbits that can be used for close approach operations. Periodic orbits are particularly of interest for regions around the binary system or around one of the bodies. Two types of periodic orbits can be computed, direct orbits and retrograde orbits. Retrograde orbits tend to be more stable in general as the particle or spacecraft orbits a body in the opposite angular direction from the system orbital motion. Since, in this case, the relative velocity between a spacecraft and the body is higher, the perturbations are reduced or averaged.

Retrograde periodic orbits can be computed using a Poincaré map reduction

method as discussed in [97], also detailed in section 2.5.2. In brief, a surface normal to the flow is chosen and the dynamics given by Eqs. (3.3) are integrated until the trajectory crosses that surface again. Using this approach, the symmetric periodic orbits can converge after correcting the initial states and iterating until the orbit comes back to the same starting point. The stability of the periodic orbits is found from investigating the eigenvalues of the monodromy matrix and methods such as the ones described in section 2.5.4 can be used to characterize critical points [26, 76].

The circular orbital velocity is used as a first guess to start the Poincaré map iterations, for periodic orbits encircling both bodies or only a single one. The velocity is computed in the rotating frame, along the y-axis, from the expression relating the inertial and rotating frames, defined earlier as

$$\boldsymbol{v_I} = \boldsymbol{v_R} + \boldsymbol{\omega} \times \boldsymbol{r}, \tag{3.56}$$

where $\boldsymbol{v_I}$ is the inertial velocity of the particle or spacecraft, $\boldsymbol{v_R}$ is its relative velocity in the rotating frame, ω is the binary spin rate, and $\boldsymbol{r}$ is the position vector of the spacecraft relative to the system or body center of mass. The magnitude of the inertial velocity is given by

$$v_I = \pm\sqrt{\frac{\mu_{sys}}{r}}, \tag{3.57}$$

where μ_{sys} is the system gravitational constant. Since the periodic orbits computed are symmetric about the x-axis, the inertial velocity is along the y-axis as well. For orbits encircling the binary system, $\mu_{sys} = G(M_1 + M_2)$. Therefore, using Eq. (3.56), the relative velocity is

$$v_R = \pm\sqrt{\frac{\mu_{sys}}{r}} + \omega r. \tag{3.58}$$

For orbits encircling only one body, the more massive body may have less pronounced gravitational disturbances as compared to the smaller one. In the case of a massive

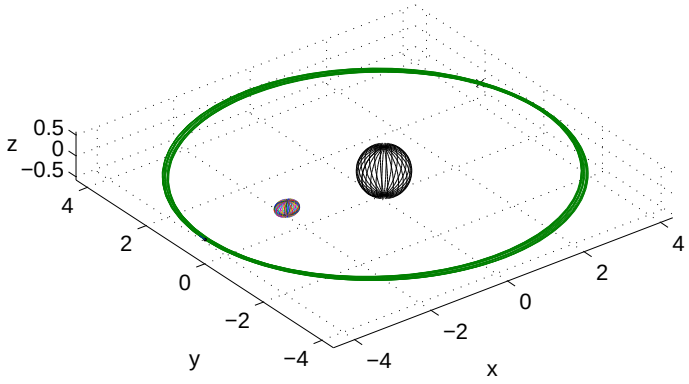

Figure 3.23: Stable retrograde periodic orbits around the binary system.

sphere, say, the specific gravitational constant is taken as $\mu_1 = GM_1$. Figure 3.23 and 3.24 show stable periodic orbits around the binary system and around a spherical primary of this binary system, respectively.

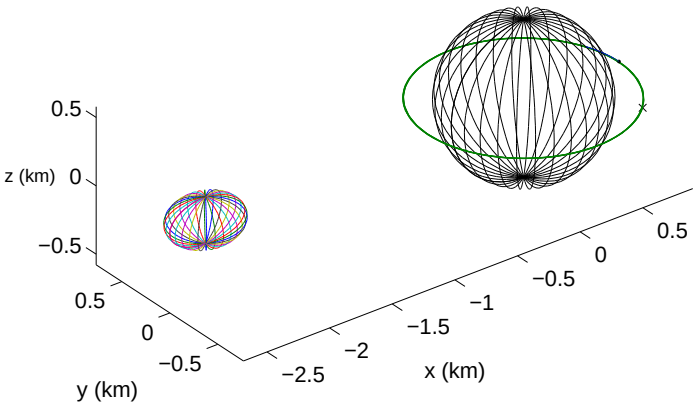

Figure 3.24: Stable retrograde periodic orbits around the massive spherical body of a binary system.

3.3 Non-Synchronized Case in the RF3BP

3.3.1 Overview

Some binary systems have been observed to have one of the bodies in synchronized rotation. In some cases, however, the bodies do not have synchronized motion, as astronomical observations show for binary systems such as 1991VH or 2003YT1 [71]. Although the analysis for such systems is fundamentally different, the stability results presented in the previous section provide insights for this non-equilibrium case.

This section focuses on the non-synchronized case of the binary system. With the system being in non-equilibrium, the geometry of the problem can be viewed as shown in Figure 3.25, where the ellipsoid spin, ω_r, is now different than the orbit period of the binary system, ω_0. For such problem, the full time-varying nonlinear equations of motion defined by Eqs. (3.1) need to be solved. As the gravitational attraction of the binary system is changing in time, the trajectories in the vicinity of the analogue equilateral points of the RF3BP become periodic orbits with a period

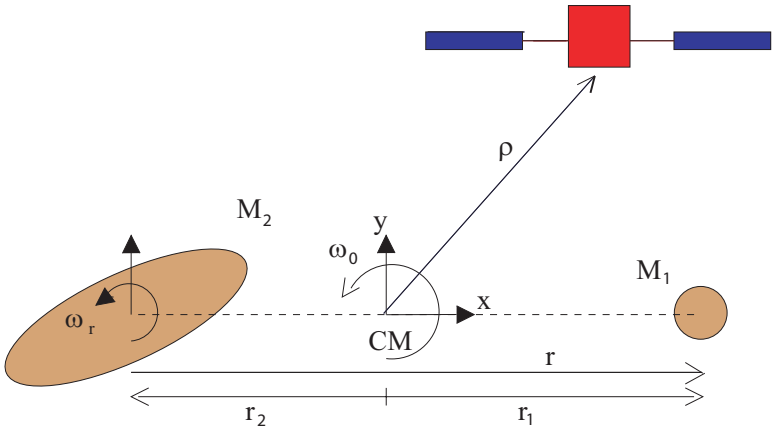

Figure 3.25: General Restricted Full Three Body Problem

equal to the period of the binary.

The first few sections describe a first order approximation method where the ratio of these two angular velocities is defined as an arbitrary free parameter in the RF3BP. The periodic orbits are computed using a Poincaré map reduction method. They are then compared to approximate results from expanding the ellipsoid potential using spherical harmonics and applying a perturbation method. The similarities in the results allow to simplify the computations in investigating the effect of the free parameters of the system. It is found that periodic orbits exist for low values of the mass ratio. The stability of these periodic orbits is also investigated using the two methods described. The stability region is reduced from the known R3BP and from results derived in the synchronized case of the RF3BP in the first part of this chapter. Finally, a method to investigate bifurcation limits is developed in the approximate system.

In the later sections, for a more realistic model, periodic perturbations to the F2BP are used in the RF3BP model. The goal is to integrate the F2BP to the RF3BP. Therefore, at each step of the integration, the F2BP dynamics are solved for and substituted into the RF3BP.

3.3.2 Binary System First Order Approximation

In the first subsection, the ratio between the mutual orbit rate and the spin rate of the ellipsoid is an added free parameter. As an approximation, this spin ratio is defined as $m = \omega_r/\omega_0$, where the ellipsoid angular velocity, ω_r, is assumed to be greater than the mean motion of the mutual orbit, ω_0. For $m \neq 1$, the $L_{4,5}$ points should bifurcate into periodic orbits. The length scale is still taken as the longest axis of the ellipsoid, α. Hence, $r = \frac{r_b}{\alpha}$, where r_b is the position vector of the sphere relative to the ellipsoid. However, from using the added free parameter m, it is now more convenient to normalize the RF3BP equations with the mean motion $\omega_0 = \sqrt{\frac{G(M_1+M_2)}{r^3}}$.

Since the motion is periodic in time, the position vector in the ellipsoid frame is expressed as $\tilde{\boldsymbol{\rho}}_{\boldsymbol{e}} = (\tilde{\boldsymbol{\rho}} - \boldsymbol{r}_{\boldsymbol{e}})\, T_r = [x_e, y_e]$ where

$$T_r = \begin{bmatrix} \cos(m-1)t & \sin(m-1)t \\ -\sin(m-1)t & \cos(m-1)t \end{bmatrix} \tag{3.59}$$

and $m = \omega_r/\omega_0$.

In components, Eqs.(3.5-3.5) are written as follows

$$\ddot{x} - 2\dot{y} - x = \frac{-\nu(x-(1-\nu)r)r^3}{r_1^3} - (1-\nu)r^3(x_e)R_{j\alpha}, \tag{3.60}$$

$$\ddot{y} + 2\dot{x} - y = \frac{-\nu y r^3}{{r_1}^3} - (1-\nu)r^3(y_e)R_{j\beta}, \tag{3.61}$$

and

$$\ddot{z} = \frac{-\nu z r^3}{{r_1}^3} - (1-\nu)r^3(y_e)R_{j\gamma}, \tag{3.62}$$

where r_1 is defined as before,

$$r_1 = \sqrt{(x-(1-\nu)r)^2 + y^2 + z^2}. \tag{3.63}$$

The R_j's expressions are the elliptic integrals representing the mass distribution of

the ellipsoid expressed in the previous chapter.

To derive analytic results to periodic orbits in the RF3BP, spherical harmonics are used as an approximation, with the general expressions given in section 2.2 on the mutual potential in the F2BP. In this case, the ellipsoid potential is expressed as

$$U_e = \frac{(1-\nu)}{r}\left[1+\frac{1}{2}\left(\frac{1}{r}\right)^2 C_{20}(3\sin^2\delta - 1) + 3\left(\frac{1}{r}\right)^2 C_{22}(1-\sin^2\delta)\cos(2\lambda) + ...\right], \tag{3.64}$$

where δ and λ are the usual spherical coordinates. Converting to the current Cartesian frame and using trigonometric identities, the ellipsoid potential becomes,

$$U_e = \frac{(1-\nu)}{r_2}\left[1 - \frac{C_{20}}{2{r_2}^2} + \frac{3C_{22}}{{r_2}^4}P_{el}\right] \tag{3.65}$$

where

$$r_2 = \sqrt{(x+\nu r)^2 + y^2 + z^2}, \tag{3.66}$$

$$P_{el} = ((x+\nu r)^2 - y^2)\cos(2(m-1)t) - 2(x+\nu r)y\sin(2(m-1)t), \tag{3.67}$$

$$C_{20} = \frac{1}{10}(2\gamma^2 - \beta^2 - 1), \tag{3.68}$$

and

$$C_{22} = \frac{1}{20}(1-\beta^2). \tag{3.69}$$

In components, and using the modified normalization above, the planar equations

of motion in the RF3BP are

$$\begin{aligned}\ddot{x} - 2\dot{y} - x =& \frac{-\nu(x-(1-\nu)r)r^3}{{r_1}^3} - \frac{(1-\nu)(x+\nu r)r^3}{{r_2}^3} \\ &+ \frac{3(1-\nu)r^3 C_{20}(x+\nu r)}{2{r_2}^5} \\ &+ \frac{3(1-\nu)r^3 C_{22}}{{r_2}^5}\left[\frac{\partial \cos 2\lambda}{\partial x}\right] \end{aligned} \tag{3.70}$$

and

$$\begin{aligned}\ddot{y} + 2\dot{x} - y =& \frac{-\nu y r^3}{{r_1}^3} - \frac{(1-\nu)y r^3}{{r_2}^3} + \frac{3(1-\nu)r^3 C_{20} y}{2{r_2}^5} \\ &+ \frac{3(1-\nu)r^3 C_{22}}{{r_2}^5}\left[\frac{\partial \cos 2\lambda}{\partial y}\right], \end{aligned} \tag{3.71}$$

where

$$\frac{\partial \cos 2\lambda}{\partial x} = 2(x+\nu r)\cos 2(m-1)t - 2y \sin 2(m-1)t$$

and

$$\frac{\partial \cos 2\lambda}{\partial y} = -2y\cos 2(m-1)t - 2(x+\nu r)\sin 2(m-1)t.$$

As expected, Eqs.(3.70) and (3.71) have small perturbation from the R3BP which are given by the spherical harmonics terms, i.e. the C_{20} and C_{22} terms.

3.3.3 Stroboscopic Poincaré Map Reduction Method

As the ellipsoid body is rotating at a different rate than the orbit rate, its gravitational attraction is periodically changing in time relative to the sphere. In the current problem, the period can be expressed as,

$$T = 1/2\left(\frac{2\pi}{m-1}\right), \tag{3.72}$$

and represents a 180^o rotation of the ellipsoid relative to the sphere. Note that this is not the period of the orbital motion of the F2BP nor is it the rotation period of the ellipsoid. A Poincaré map reduction method is used to compute the periodic orbits. Since the period is explicitly given by Eq.(3.72), similar to the method

outlined in section 2.5.2, a stroboscopic map is used where the coordinate chosen for the Poincaré map is time with $t_0 = nT$.

Using continuation of periodic orbits derived in section 2.5.3, the method was applied for variation of the mass ratio for the current application. Let's define

$$\boldsymbol{x} = \begin{bmatrix} x \\ \dot{x} \\ y \\ \dot{y} \end{bmatrix}. \tag{3.73}$$

The new correction to the initial state $\boldsymbol{x}$, $\Delta\boldsymbol{x}$, is found from,

$$\Delta\boldsymbol{x} = [I - \Phi(T)]^{-1} \left.\frac{\partial \boldsymbol{x}}{\partial \nu}\right|_T \Delta\nu, \tag{3.74}$$

where I is the identity matrix and Φ is the state transition matrix. As for the equations of motion, the state transition matrix is integrated over a full period T of the system and used in the computation of Δx. The initial conditions on Φ is the identity matrix. Φ should always have a determinant of +1. The corrected initial state is then fed into the Poincaré map method to converge to a periodic orbit again. Note that $\left.\frac{\partial \boldsymbol{x}}{\partial \nu}\right|_T$ is calculated from the following differential equation,

$$\frac{d}{dt}\left(\frac{\partial \boldsymbol{x}}{\partial \nu}\right) = \frac{\partial F}{\partial \boldsymbol{x}}\frac{\partial \boldsymbol{x}}{\partial \nu} + \frac{\partial F}{\partial \nu}. \tag{3.75}$$

Note that $\left.\frac{\partial \boldsymbol{x}}{\partial \nu}\right|_{t=0} = 0$. The matrix $\frac{\partial F}{\partial \boldsymbol{x}}$ is found from linearizing the equations of motion given by Eqs. (3.60-3.62), which gives

$$\frac{\partial F}{\partial \boldsymbol{x}} = \begin{bmatrix} \frac{\partial F_1}{\partial x_1} & \frac{\partial F_1}{\partial x_2} & \frac{\partial F_1}{\partial x_3} & \frac{\partial F_1}{\partial x_4} \\ \frac{\partial F_2}{\partial x_1} & \frac{\partial F_2}{\partial x_2} & \frac{\partial F_2}{\partial x_3} & \frac{\partial F_2}{\partial x_4} \\ \frac{\partial F_3}{\partial x_1} & \frac{\partial F_3}{\partial x_2} & \frac{\partial F_3}{\partial x_3} & \frac{\partial F_3}{\partial x_4} \\ \frac{\partial F_4}{\partial x_1} & \frac{\partial F_4}{\partial x_2} & \frac{\partial F_4}{\partial x_3} & \frac{\partial F_4}{\partial x_4} \end{bmatrix}, \tag{3.76}$$

where the components $\frac{\partial F_i}{\partial x_i}$ are,

$$\frac{\partial F_1}{\partial x_1} = 0,\ \frac{\partial F_1}{\partial x_2} = 1,\ \frac{\partial F_1}{\partial x_3} = 0, \text{ and } \frac{\partial F_1}{\partial x_4} = 0,$$

$$\frac{\partial F_2}{\partial x_1} = 1 + r^3(U_{xxs} + U_{xxe}),\ \frac{\partial F_2}{\partial x_2} = 0,\ \frac{\partial F_2}{\partial x_3} = r^3(U_{xys} + U_{xye}), \text{ and } \frac{\partial F_2}{\partial x_4} = 2,$$

$$\frac{\partial F_3}{\partial x_1} = 0,\ \frac{\partial F_3}{\partial x_2} = 0,\ \frac{\partial F_3}{\partial x_3} = 0, \text{ and } \frac{\partial F_3}{\partial x_4} = 1,$$

$$\frac{\partial F_4}{\partial x_1} = r^3(U_{xys} + U_{xye}),\ \frac{\partial F_4}{\partial x_2} = -2,\ \frac{\partial F_4}{\partial x_3} = 1 + r^3(U_{yys} + U_{yye}), \text{ and } \frac{\partial F_4}{\partial x_4} = 0.$$

The second order partial derivatives were given in Chapter 2. Note that, for the ellipsoid, the second derivatives are transformed from inertial to the rotating coordinate system fixed at the ellipsoid by,

$$U_e = T_r \tilde{U}_e T_r^{-1}. \tag{3.77}$$

Now, the expression for $\frac{\partial F}{\partial \nu}$ is given by,

$$\frac{\partial F}{\partial \nu} = \begin{bmatrix} \frac{\partial F_1}{\partial \nu} \\ \frac{\partial F_2}{\partial \nu} \\ \frac{\partial F_3}{\partial \nu} \\ \frac{\partial F_4}{\partial \nu} \end{bmatrix}, \tag{3.78}$$

where the components $\frac{\partial F_i}{\partial \nu}$ are,

$$\frac{\partial F_1}{\partial \nu} = 0 \tag{3.79}$$

$$\begin{aligned}\frac{\partial F_2}{\partial \nu} =& -\frac{(x-(1-\nu)r+\nu r)}{[(x-(1-\nu)r)^2+y^2]^{\frac{3}{2}}} + \frac{3r\nu(x-(1-\nu)r)^2}{[(x-(1-\nu)r)^2+y^2]^{\frac{5}{2}}} \\ &+ (x+\nu r-(1-\nu)r)R_{j\alpha} \\ &+ \frac{r(1-\nu)(x+\nu r)^2}{(1+\lambda)^2}\left((R_{j\alpha}+R_{j\beta}+R_{j\gamma})\left[\frac{1}{\frac{(x+\nu r)^2}{(1+\lambda)^2}+\frac{y^2}{(\beta^2+\lambda)^2}+\frac{z^2}{(\gamma^2+\lambda)^2}}\right]\right)\end{aligned} \tag{3.80}$$

$$\frac{\partial F_3}{\partial \nu} = 0 \tag{3.81}$$

$$\begin{aligned}\frac{\partial F_4}{\partial \nu} =& \frac{-y}{[(x-(1-\nu)r)^2+y^2]^{\frac{3}{2}}} + \frac{3r\nu(x-(1-\nu)r)y}{[(x-(1-\nu)r)^2+y^2]^{\frac{5}{2}}} \\ &+ yR_{j\beta} \\ &+ \frac{r(1-\nu)(x+\nu r)y}{(1+\lambda)(\beta^2+\lambda)}\left((R_{j\alpha}+R_{j\beta}+R_{j\gamma})\left[\frac{1}{\frac{(x+\nu r)^2}{(1+\lambda)^2}+\frac{y^2}{(\beta^2+\lambda)^2}+\frac{z^2}{(\gamma^2+\lambda)^2}}\right]\right).\end{aligned} \tag{3.82}$$

3.3.4 Analytic Computation of Periodic Orbits using Spherical Harmonics

To develop an analytical method, the spherical harmonics are now used to approximate the potential of the ellipsoid. In order to compute periodic orbits, the equations of motion given by Eqs. (3.70-3.71) can be written in the following form,

$$\dot{x_i} = g_i(x_j) + \mu f_i(x_j, t), \tag{3.83}$$

where $f_i(x_j, t)$ are periodic functions [60]. Comparing Eq. (3.83) to Eqs.(3.70-3.71), $g_i(x_j)$ are given by the undisturbed expressions of the R3BP, μ is the spherical harmonic coefficient C_{20} or C_{22} and $f_i(x_j, t)$ are the small perturbation introduced by the ellipsoid potential.

To get a general expression, let the solution be given as an expansion in the

parameter μ,

$$x_i = {x_i}^0 + \mu {x_i}^1 + \mu^2 {x_i}^2 + ... \tag{3.84}$$

Equation (3.84) is substituted into (3.83), and only terms up to the first order in μ are kept. Then, solving each order in μ, up to the first order, gives

$$\dot{{x_i}}^0 = g_i({x_j}^0), \tag{3.85}$$

and

$$\dot{{x_i}}^1 = \left.\frac{\partial g_i}{\partial x_j}\right|_{{x_j}^0} {x_j}^1 + f_i({x_j}^0, t). \tag{3.86}$$

For convenience in the notation, Eq. (3.86) is written in matrix form,

$$\dot{{x_i}}^1 = A{x_j}^1 + B(t), \tag{3.87}$$

which has solution,

$${x_i}^1 = \exp(At){x_{0j}}^1 + \int_0^t \exp(A(T-t))B(t)dt, \tag{3.88}$$

where ${x_{0j}}^1$ is the initial conditions for ${x_j}^1$.

For a periodic orbit, Eq.(3.88) satisfies the condition

$${x_j}^1(T) = {x_j}^1(0). \tag{3.89}$$

Hence, the initial conditions to give a periodic orbit are

$${x_{0j}}^1 = (I - \exp(AT))^{-1} \int_0^T \exp(A(T-t))B(t)dt. \tag{3.90}$$

These initial conditions are used in the solution of the ${x_j}^1$ equations. Then, the complete solution is given by Eq.(3.84).

3.3.5 Analytic Determination of Stability

The stability of these periodic orbits are then addressed using Floquet theory. In general, the stability can be investigated for a periodic system written in the form,

$$\dot{x_i} = \theta_{ij}(t)x_j \tag{3.91}$$

where the $\theta_{ij}(t)$ are periodic functions of time, with period T [60]. To relate to the current problem, a special case can be used where $\theta_{ij}(t)$ are expanded as power series in a small parameter of the form

$$\theta_{ij}(t) = a_{ij} + \mu\theta_{ij}(t) + ..., \tag{3.92}$$

where each θ_{ij} are periodic in time with period T and a_{ij} are constant. In matrix form, this translates to

$$\dot{x} = (A + \mu\Theta)\, x. \tag{3.93}$$

Now, applying this method for the current problem given by Eq. (3.83), let's expand about the periodic solution, $x_{pi} = {x_i}^p + \delta x_i$, where each ${x_i}^p$ has the form $x_{p0} + \mu x_{p1}$, to then substitute into Eq. (3.83). This reduces to

$$\begin{aligned}\delta\dot{x} &= \left(\left.\frac{\partial g}{\partial x}\right|_{x_p} + \mu \left.\frac{\partial f}{\partial x}\right|_{x_p} \right)(\delta x) + ... \\ &= \left[\left.\frac{\partial g}{\partial x}\right|_{x_{p0}} + \mu \left(\left.\frac{\partial^2 g}{\partial x^2}\right|_{x_{p0}} (x_{p1}) + \left.\frac{\partial f}{\partial x}\right|_{x_{p0}} \right) \right](\delta x) + ...\end{aligned} \tag{3.94}$$

Comparing Eq. (3.94) with Eq. (3.93), A is defined as

$$A = \left.\frac{\partial g}{\partial x}\right|_{x_{p0}}, \Theta = \left.\frac{\partial^2 g}{\partial x^2}\right|_{x_{p0}} (x_{p1}) + \left.\frac{\partial f}{\partial x}\right|_{x_{p0}}.$$

Note that A is a matrix of constants and Θ is periodic. Over one period T, the stability of the system can be evaluated by finding the roots to the equation,

$$|\lambda I - \Phi(T, 0)| = 0, \tag{3.95}$$

where Φ is the state transition matrix and λ is an eigenvalue of Φ. Note that Φ satisfies

$$\dot{\Phi} = (A + \mu\Theta)\,\Phi. \tag{3.96}$$

For a periodic system, from Floquet theory, the eigenvalues and the state transition matrix have the form $\lambda \sim e^{\alpha T}$ and $\Phi \sim e^{\alpha T}P$, where P is a periodic Lyapunov transformation with period T, and α is a constant [60]. The characteristic exponent of the eigenvalues is expanded as

$$\begin{aligned}\lambda =& e^{\alpha T} = e^{(\alpha_0+\mu\alpha_1+...)T} = e^{\alpha_0 T}(1 + \mu\alpha_1 T + ...) \\ &= e^{\alpha_0 T} + \mu\alpha_1 T e^{\alpha_0 T} + ... = \lambda_0 + \mu\alpha_1 T\lambda_0 + ...\end{aligned} \tag{3.97}$$

Now, let $\Phi = \Phi^0 + \mu\Phi^1$, with the initial conditions ${\Phi_0}^0 = I$ and ${\Phi_0}^1 = 0$ and substitute into Eq.(3.96). As before, one can solve for the zeroth and first order in μ, which gives

$$\Phi^0 = \exp(At) \tag{3.98}$$

and

$$\Phi^1 = \int_0^t \exp(A(t-\tau))\Theta\Phi^0 d\tau. \tag{3.99}$$

Substituting into Eq.(3.95), the characteristic equation is found from,

$$\left|\lambda_0 I - \Phi^0(T,0) + \mu[\alpha_1 T\lambda_0 I - \Phi^1(T,0)]\right| = 0. \tag{3.100}$$

A Taylor series expansion is applied for small μ. In doing this, all orders of μ will equal 0 independently, leading to

$$\left|\lambda_0 I - \Phi^0(T,0)\right| = 0 \tag{3.101}$$

and

$$\frac{\partial}{\partial\mu}\left|\lambda_0 I - \Phi^0(T,0) + \mu[\alpha_1 T\lambda_0 I - \Phi^1(T,0)]\right|_{\mu=0} = 0. \tag{3.102}$$

Now, let $C = A + \mu B$ be the expression inside the absolute value in Eq. (3.102)

with each entry in C being c_{ij}. Then,

$$\begin{aligned}\frac{\partial}{\partial\mu}|C| &= \sum_{i=1}^{n}\sum_{j=1}^{n}\frac{\partial}{\partial c_{ij}}|C|\frac{\partial c_{ij}}{\partial\mu} \\ &= \sum_{i=1}^{n}\sum_{j=1}^{n}(-1)^{i+j}|C|_{ij,\mu=0}\left.\frac{\partial c_{ij}}{\partial\nu}\right|_{\mu=0} = 0, \end{aligned} \tag{3.103}$$

where $|C|_{ij}$ is the minor of C corresponding to the i^{th} row and the j^{th} column. Then,

$$\sum_{i=1}^{n}\sum_{j=1}^{n}(-1)^{i+j}|A|_{ij}B_{ij} = 0. \tag{3.104}$$

Now substituting for C and rearranging,

$$\begin{aligned}&\sum_{i=j=1}^{n}\alpha_1 T\lambda_0|\lambda_0 I - \Phi^0(T,0)|_{ij} \\ &= \sum_{i=1}^{n}\sum_{j=1}^{n}(-1)^{i+j}|\lambda_0 I - \Phi^0(T,0)|_{ij}\Phi^1(T,0)_{ij}. \end{aligned} \tag{3.105}$$

Hence, for each λ_0, the corresponding α_1 is computed as

$$\alpha_1 = \frac{\sum_{i=1}^{n}\sum_{j=1}^{n}(-1)^{i+j}|\lambda_0 I - \Phi^0(T,0)|_{ij}\Phi^1(T,0)_{ij}}{T\lambda_0\sum_{i=j=1}^{n}|\lambda_0 I - \Phi^0(T,0)|_{ij}}, \tag{3.106}$$

and the characteristic exponent of the eigenvalue is given by Eq. (3.97).

The previous result leads to defining stability limits for a range of parameters, ν, m, r, β and γ. When a periodic orbit is stable, there will be two characteristic exponents, say $\alpha^1 T$ and $\alpha^2 T$, and their complex conjugates. We can assume that the system bifurcates when $\alpha^1 T = \alpha^2 T$. Substituting for α, we have

$${\alpha_0}^1 + \mu^*{\alpha_1}^1 = {\alpha_0}^2 + \mu^*{\alpha_1}^2. \tag{3.107}$$

Hence, given a mass ratio and a ratio of orbits, the corresponding μ^* is function of r, β and γ, giving results of stability on a 3-dimensional plot.

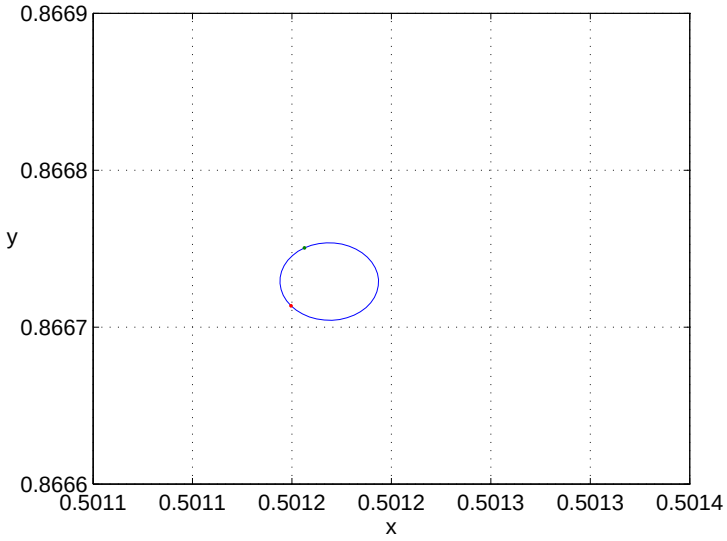

Figure 3.26: Periodic orbit in the vicinity of the L_4, L_5 using a Poincaré map method. $r = 2$, $\beta = .95$, $\gamma/\beta = 1$, $\nu = .02$, $m = 10$.

3.3.6 Comparison of Results obtained using the Poincaré Map and the First Order Perturbations Approximation

Periodic orbits were computed using the Poincaré map and the perturbation methods. Figures 3.26 and 3.27 show periodic orbits obtained with the two methods while keeping the same parameters. In these cases, $r = 2$, $\beta = \gamma = 0.95$, $\nu = 0.02$ and $m = 10$ as it is difficult to converge on a periodic orbit using the Poincaré map for a more pronounced ellipsoid. As one can notice, the orbits are slightly offset and the ones from the approximation are slightly smaller in size. Despite these small differences, the initial conditions agree to the fourth digit.

When using the full non-linear equations, i.e. Eqs. (3.60 and 3.61), periodic orbits exist for low values of the mass ratio. Figure 3.28 shows the variations in the initial conditions of the periodic orbits on the $\hat{\imath} - \hat{\jmath}$ plane for mass ratios varying from 0 (bottom right) up to 0.025. This plot has been shifted by $r\nu$ so that the ellipsoid is at the origin and the sphere at a distance 1 from it on the x axis.

The Poincaré map reduction method has been used extensively to study periodic

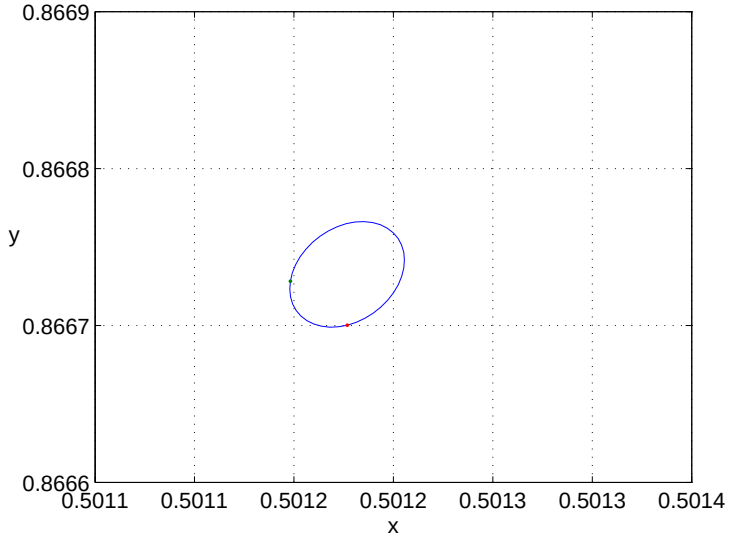

Figure 3.27: Periodic orbit in the vicinity of the L_4, L_5 using the approximate system and a perturbation method. Parameters: $r = 2$, $\beta = .95$, $\gamma/\beta = 1$, $\nu = .02$, $m = 10$.

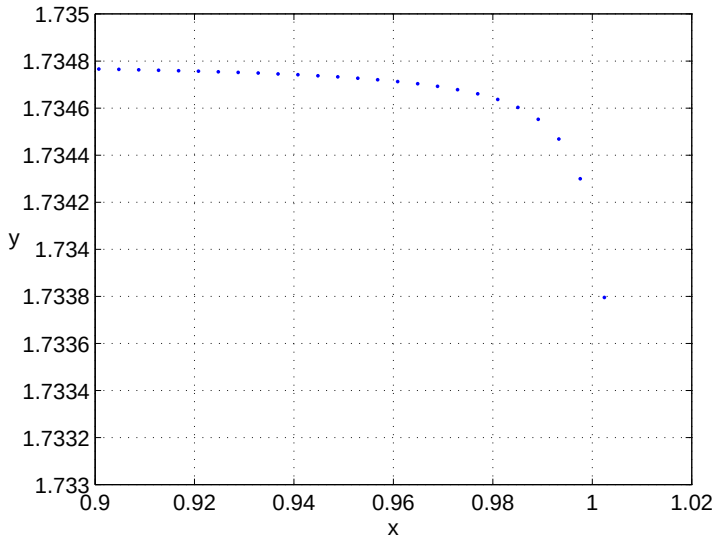

Figure 3.28: Initial conditions of periodic orbits for continuation with respect to the mass ratio, ν, in the vicinity of the L_4, L_5 using a Poincaré map method. $r = 2$, $\beta = .95$, $\gamma/\beta = 1$, $\nu = 0.001$ to 0.025, $m = 10$.

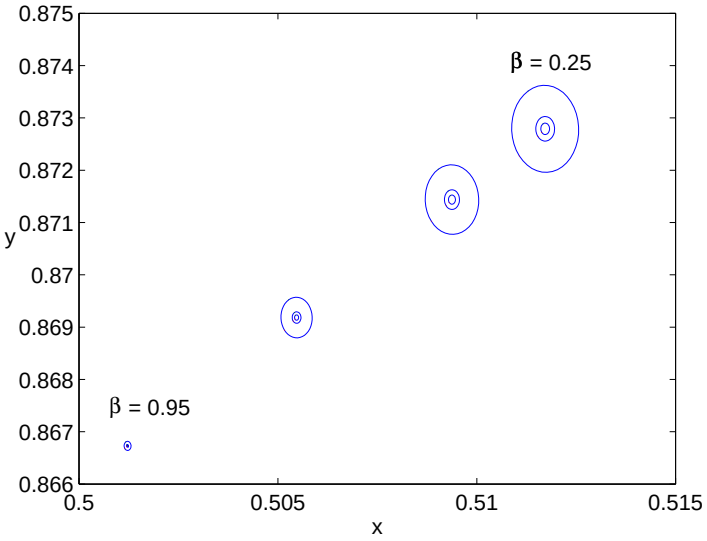

Figure 3.29: Periodic orbits in the vicinity of the L_4, L_5 using spherical harmonics expansion. $r = 2$, β varies from 0.25 to 0.95, $\gamma/\beta = 1$, $\nu = .03$, m varies from 6 to 14.

systems. Continuations for other free variables than the mass ratio, i.e.β, γ and the distance r, are mathematically difficult to compute when working with elliptic integrals. The similarity in the results indicate that the approximation using spherical harmonics recovers the results from the analytical system. Hence, the perturbation method provides insight into this behavior and is time efficient. This allows to run through the parameters without performing the difficult numerical computations.

Varying r, ν, β and γ have different effects on the periodic orbits. Decreasing the parameter β of the ellipsoid makes the orbit larger in size and shifts it away from the equilibrium solutions. In this case, the effect of the ellipsoid become more important as it becomes less spherical. On the other hand, increasing the ratio of the rotation rate, m, makes the periodic orbit smaller in size. This is because, in the limit, a fast rotating ellipsoid would resemble an oblate sphere. Figures 3.29 and 3.30 show the effect of changing the β-size of the ellipsoid and the orbit ratio.

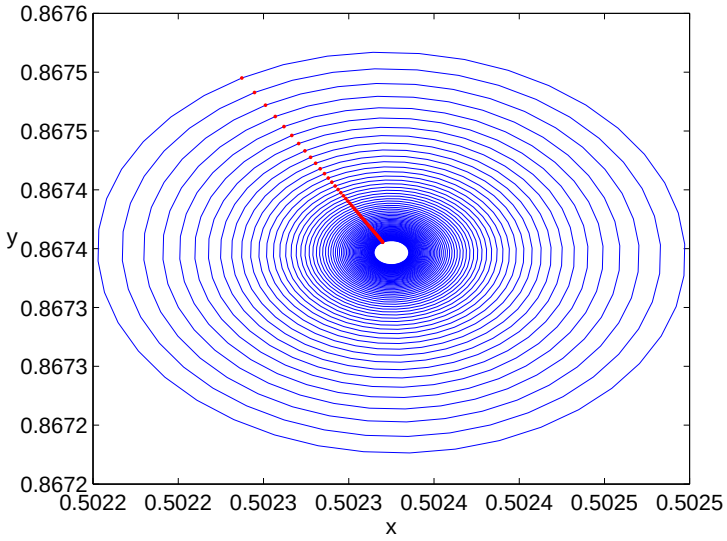

Figure 3.30: Periodic orbits in the vicinity of the L_4, L_5 using spherical harmonics expansion. Parameters: $r = 2$, $\beta = .90$, $\gamma/\beta = 1$, $\nu = .02$, m varies from 6 (outer ring) to 20.

3.3.7 Stability Comparison Analysis

For the periodic orbits computed using the Poincaré map method on the nonlinear equations, as before, the stability of the periodic orbits can be investigated by computing the eigenvalues of the state transition matrix. Since there is no integral of motion, Φ has no unity eigenvalues at a periodic orbit. In this system, a periodic orbit is stable if all the eigenvalues are 1 in magnitude. Investigating stability indicates that the region of stable motions is fairly reduced from previous results of the equilibrium case. Figure 3.31 is a plot of the stability region as function of the mass ratio and the ratio of orbits. The region below the line represents stable periodic orbits. Note that it is difficult to compute the periodic orbits across the entire range of parameter values. The stability was only computed near the boundaries. We see that stable orbits exist for small mass ratio up to 0.0235. We also notice a small region of stability near an orbit ratio of 2.

In general, it is found that the results from stability using Floquet theory diverge from the results using the nonlinear system. The difference between the two stability

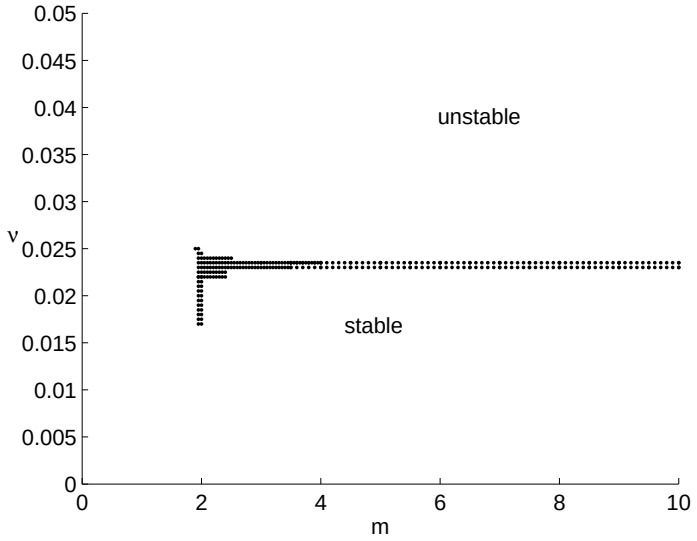

Figure 3.31: Stability region of periodic orbits using Poincare's method. The region below the line indicates stable points. The mass ratio is on the y axis and the orbit ratio on, x. $r = 2$, $\beta = .90$, $\gamma/\beta = 1$

regions is not fully understood. Figure 3.32 below shows the stability region as function of the mass ratio and the ratio of orbits using perturbation methods. Periodic orbits are stable in the shaded area. The resonance case is also not observed for low values of the orbit ratio as for the nonlinear equations. However, the ellipsoid size and the distance between the primaries reduce the stability region for decreasing β and small distance r.

Finally, a three-dimensional surface can be obtained representing the stability bifurcation limits from Eq. (3.107). Figures 3.33 and 3.34 show the relation between the spherical harmonic coefficient, μ, the orbit ratio, m, and the mass ratio, ν in the plane for easier visualization. The complete stability bifurcation surface is shown in Figure 3.35. Note that the value given by the Routh criteria is shown as a star point on the plots. As the orbit ratio gets closer to 1, i.e. closer to the synchronous case in the F2BP, the system shows more chaotic behavior as the system approaches the singularity at m=1. From the definition of μ, i.e. C_{20}, results allow values of β and γ only for small C_{20}. This happens for mass ratios close to 0.035.

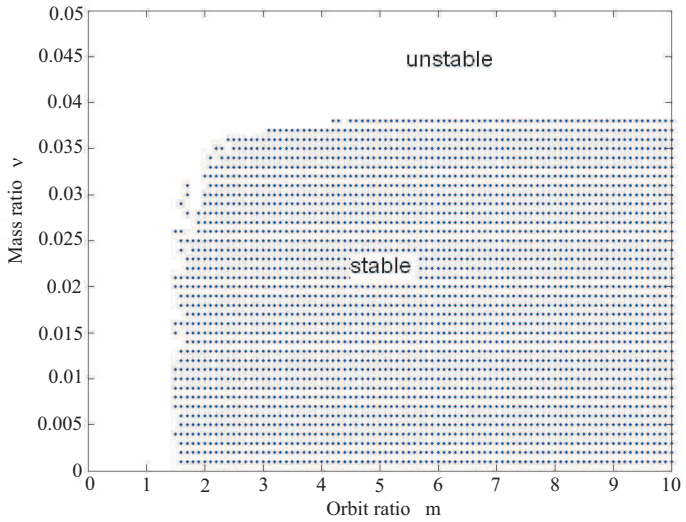

Figure 3.32: Stability region of periodic orbits in the vicinity of the L_4, L_5 using spherical harmonics expansion. $r = 2$, $\beta = 0.9$ and $\gamma/\beta = 1$

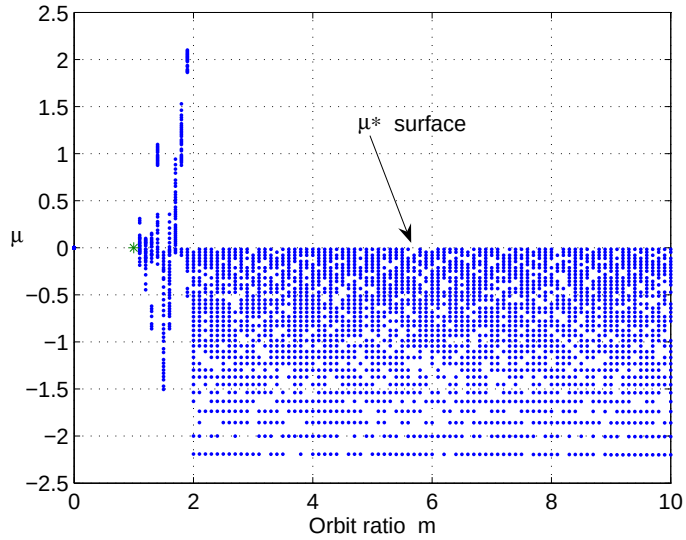

Figure 3.33: Bifurcation diagram for periodic orbits in the vicinity of the L_4, L_5 for $r = 2$: μ as function of m. The star point is the value of the Routh criteria.

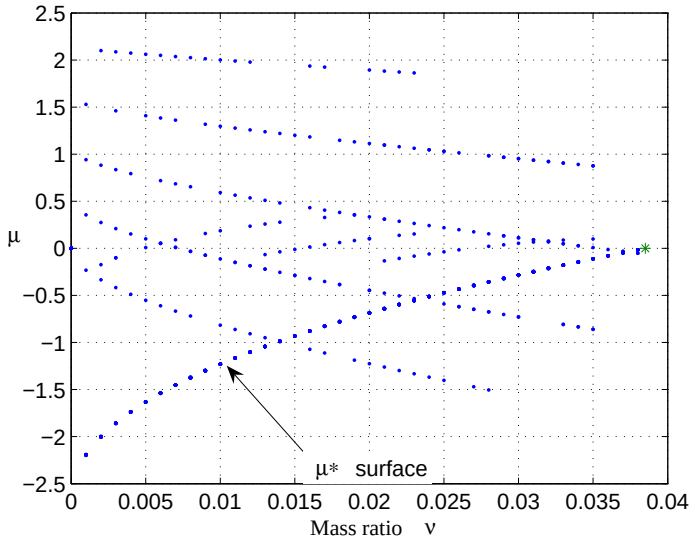

Figure 3.34: Bifurcation diagram for periodic orbits in the vicinity of the L_4, L_5 for $r = 2$: μ as function of ν. The star point is the value of the Routh criteria.

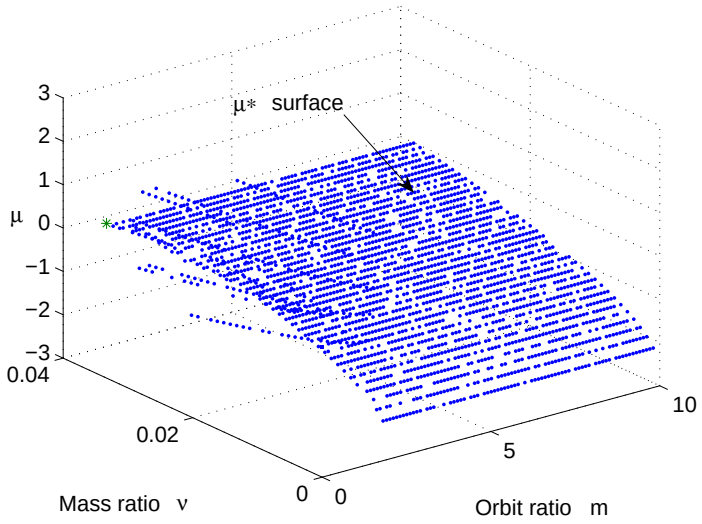

Figure 3.35: Bifurcation surface for periodic orbits in the vicinity of the L_4, L_5 for $r = 2$. The star point is the value of the Routh criteria.

The next step is the computation and general description of periodic orbits in the Full Two-Body Problem. The motion of the primaries can then be included into the model of the RF3BP.

3.4 Periodic Orbits in the RF3BP using Perturbations in the F2BP

In the previous section, the motion of the binary system was set as constant, where the ratio of the ellipsoid angular spin and the system orbit rate was a free parameter. The next step is to account for the true motion of the F2BP and to make the connection between the dynamics of the RF3BP and the F2BP. In order to do so, the dynamics of the RF3BP can be expressed under periodicity in a frame fixed to the general body with origin at the ellipsoid center of mass. In this frame, a periodic model is developed for the F2BP and substituted in the RF3BP. The periodic approximation uses the method of eigenvalues and eigenvectors described in section 2.5.6.

This problem can again be investigated in a few ways depending on the reference frame chosen. When considering a rotating frame fixed to the binary system center of mass, it is hard to define a normalizing time scale such as a mean motion. As for working in an inertial frame, the computation of an orbit could be difficult since it may not make a closed trajectory in this frame. Hence, it was found more convenient to express the dynamics of the RF3BP under periodicity in a frame fixed to the general body with origin at the general body center of mass.

For better clarity, the dynamics of a particle in this frame are restated. First, let the position of a particle relative to the center of mass of the system denoted as $\boldsymbol{\rho}$ in a frame rotating with the ellipsoid. With this frame, the same normalization introduced for the F2BP can be used. Then, the equations of motion can be written

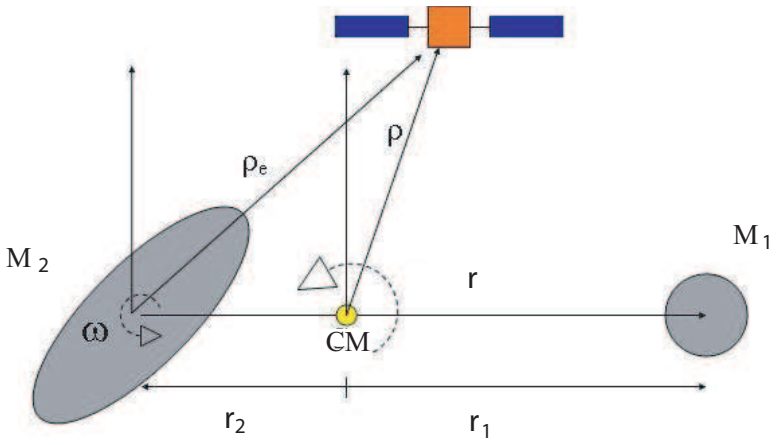

Figure 3.36: Geometry of the Restricted Full Three Body Problem

in the following form,

$$\ddot{\boldsymbol{\rho}} + 2\boldsymbol{\omega} \times \dot{\boldsymbol{\rho}} + \dot{\boldsymbol{\omega}} \times \boldsymbol{\rho} + \boldsymbol{\omega} \times (\boldsymbol{\omega} \times \boldsymbol{\rho}) = \frac{\partial U_{12}}{\partial \boldsymbol{\rho}}.$$

Note that U_{12} is a time varying potential energy expression, as the bodies are not in mutual equilibrium.

Since the F2BP is solved in a frame fixed to the ellipsoid, let $\boldsymbol{\rho_E}$ be the position of a particle relative to the center of the ellipsoid. Then, $\boldsymbol{\rho} = \boldsymbol{\rho_E} - \boldsymbol{r_E}$, as shown in Figure 3.36.

In an inertial frame, differentiating $\boldsymbol{\rho}$ twice with respect to time gives

$$\ddot{\boldsymbol{\rho}} = \ddot{\boldsymbol{\rho}}_{\boldsymbol{E}} + \ddot{\boldsymbol{r}}_{\boldsymbol{E}} = \frac{\partial U_{12}}{\partial \boldsymbol{\rho}} = \frac{\partial U_{12}}{\partial \boldsymbol{\rho_E}}. \tag{3.108}$$

Or,

$$\ddot{\boldsymbol{\rho}}_{\boldsymbol{E}} = \frac{\partial U_{12}}{\partial \boldsymbol{\rho_E}} - \ddot{\boldsymbol{r}}_{\boldsymbol{E}}. \tag{3.109}$$

In this case, the potential energy expression is expressed as,

$$U_{12} = \frac{\nu}{|\boldsymbol{\rho_E} - \boldsymbol{r}|} + (1 - \nu) U_e(\boldsymbol{\rho_E}). \tag{3.110}$$

Again, U_e represents the normalized expression for the ellipsoid body and it is

defined by Eqs. (2.18-2.20). Hence, in a frame rotating with the ellipsoid with origin at the ellipsoid center, Eq. (3.109) becomes,

$$\ddot{\boldsymbol{\rho}}_{\boldsymbol{E}} + 2\boldsymbol{\omega} \times \dot{\boldsymbol{\rho}}_{\boldsymbol{E}} + \dot{\boldsymbol{\omega}} \times \boldsymbol{\rho}_{\boldsymbol{E}} + \boldsymbol{\omega} \times (\boldsymbol{\omega} \times \boldsymbol{\rho}_{\boldsymbol{E}}) = \frac{\partial U_{12}}{\partial \boldsymbol{\rho}_{\boldsymbol{E}}} + \nu \frac{\partial U_e}{\partial \boldsymbol{r}}\bigg|_{\boldsymbol{r}} .$$

Note that the extra term in Eq. (3.111) appears as the origin is shifted from the two-body system center of mass to the ellipsoid center, for which the mutual potential of Eq. (2.16) can be substituted. Since the underlying F2BP dynamics is periodic, the added potential is also time varying. The free parameters of this system are the mass ratio, ν, the energy, E, the angular momentum, K, and the size parameters of the ellipsoid, β and γ. The angular velocity ω is substituted from the solution of the F2BP, computed from the angular momentum integral, i.e. Eq. (2.27). The angular acceleration, $\dot{\omega}$ is computed from deriving this same equation, given by Eq. (2.21) or differentiating Eq. (2.27).

3.4.1 Results and Stability Properties of Periodic Orbits

As a first step, one can look at the general dynamics under these conditions. Far from the system, the effect of the ellipsoid is small. Figure 3.37 shows the particle in the vicinity of L_4 for the case $r = 7$. In the absence of the periodic perturbations this equilibrium point is stable. When the perturbations to the F2BP is large enough, the particle leaves the L_4 region and gets in orbit around the system. Thus the F2BP periodic orbits can destabilize motion in the RF3BP.

Figure 3.38 shows an orbit near the analogue L_4 point. In this case, the ellipsoid dominates with $\nu = 0.02$ and $r = 2.0749$, giving a stable equilibrium point of the RF3BP but an unstable relative equilibria in the F2BP. This orbit is computed for the same period as the periodic model in the F2BP but it is not periodic. Figure 3.39 shows the orbit evolution on a longer simulation time.

Figure 3.40 shows a periodic orbit for a sphere dominating system with $\nu = 0.98$

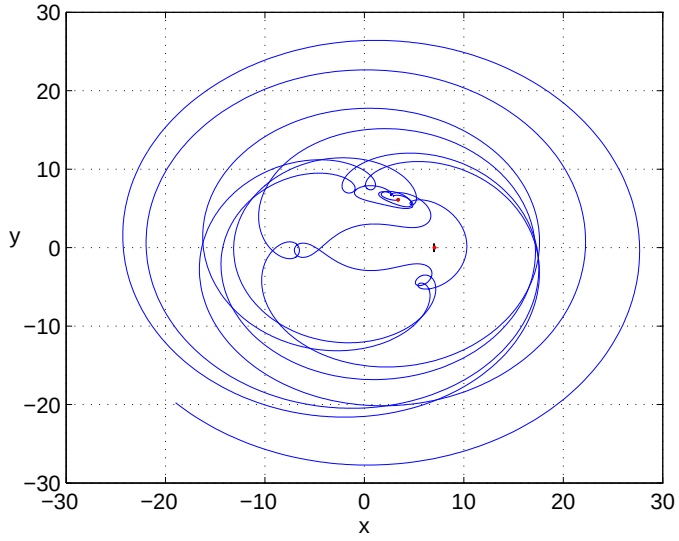

Figure 3.37: RF3BP dynamics using a periodic model for the F2BP. Initial conditions: $[q, p] = [3.407; 0; 0; 6.1063]$. Parameters: $\nu = 0.03$, $\beta = \gamma = 0.9$.

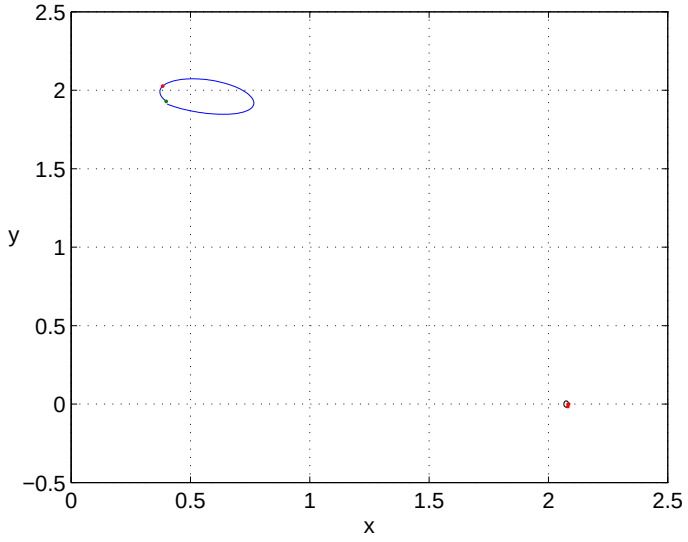

Figure 3.38: RF3BP dynamics using a periodic model for the F2BP. Initial conditions: $[q, p] = [0.3983; -0.0356; 1.9293; 0.0434]$. Parameters: $\nu = 0.02$, $\beta = \gamma = 0.9$.

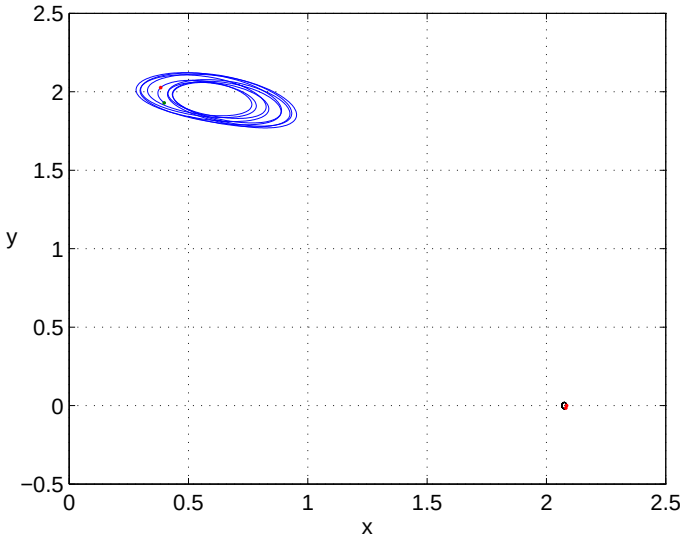

Figure 3.39: RF3BP dynamics using a periodic model for the F2BP. Initial conditions: $[q, p] = [0.3983; -0.0356; 1.9293; 0.0434]$ simulated over 10 time periods of the F2BP. Parameters: $\nu = 0.02$, $\beta = \gamma = 0.9$.

and $r = 2.0749$. The plots show three different periodic orbits from having three different perturbations in the F2BP. As the perturbation gets large, the periodic orbit amplitude increases and the periodic orbit is shifted from encircling the equilibrium location. Note that these periodic orbits are stable. These parameters give a stable equilibrium point in the RF3BP and a stable relative equilibria in the F2BP. Figure 3.41 is a closer view of one of the periodic orbits.

The results above show that the stability properties of the equilibrium conditions in both the RF3BP and the F2BP have different effects on the dynamics of the RF3BP. It was found that periodic orbits exist for systems with a massive spherical primary, which differ from the results obtained when the ratio of the ellipsoid spin to the orbit rate is assumed to be a free parameter. However, having a model for the motion of the F2BP included in the RF3BP is a higher fidelity model of the problem. Although left as future research, other periodic orbits around the system or around one of the bodies may be interesting to compute. Then, looking at the three dimensional motion is certainly a rich problem to study.

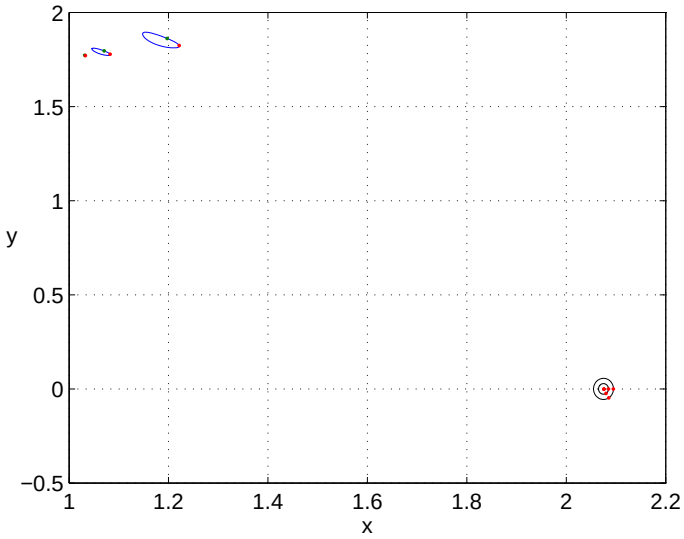

Figure 3.40: RF3BP dynamics using a periodic model for the F2BP. Initial conditions: $[q,p]_1 = [1.0315; 0.0006; 1.7722; -0.0006]$, $[q,p]_2$=[1.0706; 0.0063; 1.7956; -0.0065] and $[q,p]_3$=[1.1972; 0.0131; 1.8618; -0.0142]. Parameters: $\nu = 0.98$, $\beta = \gamma = 0.9$.

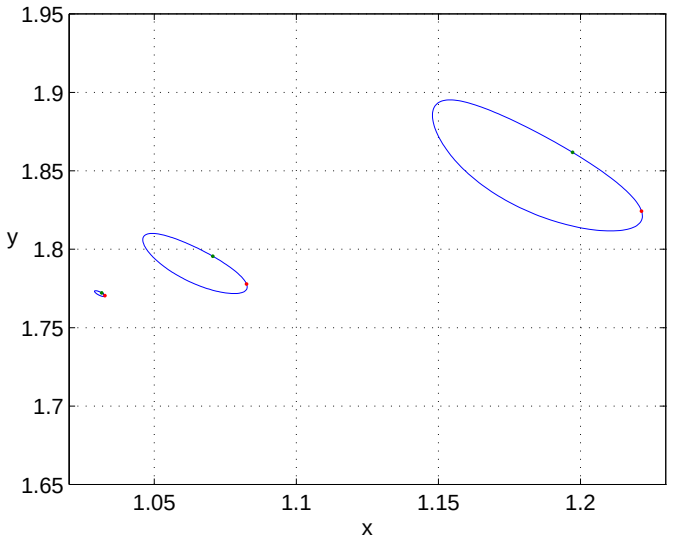

Figure 3.41: Closer view of the RF3BP dynamics using a periodic model for the F2BP. Initial conditions: $[q,p]_1 = [1.0315; 0.0006; 1.7722; -0.0006]$, $[q,p]_2$=[1.0706; 0.0063; 1.7956; -0.0065] and $[q,p]_3$=[1.1972; 0.0131; 1.8618; -0.0142]. Parameters: $\nu = 0.98$, $\beta = \gamma = 0.9$.

Having described the dynamics of particles or spacecraft in the field of binary systems, a natural extension is to look into mission design. Having surface constraints for the bodies introduce interesting robotic applications, which is introduced next.

CHAPTER 4

ROBOTIC EXPLORATION ON BINARY ASTEROID SYSTEMS

4.1 Goals and Assumptions

Robotic exploration is a natural extension of modeling the dynamics of particles in the gravitational field of two primaries. There is some heritage of rover exploration of other worlds such as the Spirit and Opportunity rovers on Mars, and landing on small bodies has been achieved by NEAR and Hayabusa [32, 49, 21, 57]. The advantage for in situ investigation is clear, and among the current small body proposals, a few are to send micro or nano rovers for sample return missions [94, 100, 46, 34]. In general, the robots will have some power generation capabilities to support their navigation tools and science instruments, as well as ways for communicating data to the spacecraft, and means of moving on the surface using small thrusters or equivalent driving systems. However, the details of a robotic mission hardware are left for future studies. The focus here is instead on the dynamics and control of these robots. Some assumptions are made on their design and subsystems, summarized in Table 4.1.

The goal in sending robots for surface investigation is to maximize the search area for mapping, imaging, and taking geological/scientific measurements or samples. Collaborative spacecraft or robot applications increase the range of scientific measurements and chance of success. A number of studies have looked at spacecraft formations and cooperative rovers applications for planetary exploration (to name a

Subsystems	Instruments
Navigation	Star tracker, relative tracking to spacecraft, relative tracking to other rovers
Telecommunications	Transmit and receive to spacecraft and to rovers
Science payload	Sensors, Langmuir probes, imagers, temperature probes
Power generation/storage	Solar arrays, batteries
Driving mechanism	Hopping devices, small thrusters
C&DH	Small processor, onboard memory

Table 4.1: Hardware needed for a robotic surface explorer at a binary asteroid system.

few, see [92, 3, 25, 27, 2, 16, 39]). Here, the proposed robotic mission is composed of a mother ship and a number of cooperative robots for surface exploration. However, for asteroid applications, one needs to design for very low gravity fields, about 1/1000 of the Earth's gravity. In such an environment, wheeled rovers might be difficult to control and navigate. There has been interest in looking at surface motion for "hoppers" on the asteroid surface, as a vehicle would most likely bounce from hitting the surface and loose traction. In addition, "hoppers" would be able to investigate a larger area in quicker time and might be easier to control. These conditions and ideas of hopping motion have already been explored for the Hayabusa mission sent to Itokawa by JAXA as it included a small hopper type robot called MINERVA, and used surface target markers as reference point [100, 75, 99]. Unfortunately, MINERVA was lost after deployment before reaching the surface.

For the current study, a spacecraft is assumed to be in orbit about a binary from which landers could be launched to the surface for further exploration. It can be assumed that the hoppers have their own star tracker, from which, by using fixed astronomical objects, they can compute their position and report their location to the spacecraft in orbit. For surface exploration purposes and collaborative work, the

hoppers also need to interact among themselves, which can be done through the use of sensors, vision systems and microprocessors. Hence, a hopper could easily move on the surface, investigating the region while taking scientific data. For surface motion, one needs to use impact dynamics in order to develop a model that predicts the distance traveled and the time it takes in reaching a given destination. This topic is introduced first and validated with simulations of hopping dynamics within the dynamics of rotating ellipsoids. The current model treats the vehicle as a particle, future work should investigate the rover as a rigid body with a size and shape. The landers could be released at one end of the asteroid, sent on a predefined grid and move to the other end. Hence, the second part of this chapter looks at the control required for such operations.

4.2 Surface Motion

4.2.1 Hopping on a Flat Surface

MINERVA, originally designed for the Hayabusa mission is a good example of a "hopper" application, where the robot uses a torque driving system as the main driver [101, 100]. Ball Aerospace also designed a sphere robot being controlled by a set of small thrusters, and having three sides opening for stability on the surface [89]. In all cases, the motion of these hoppers looks like the ballistic trajectory shown in Figure 4.1. Hoppers could easily investigate the surface by controlling their initial bounce velocity and orientation from estimating the jumping distance to be covered for a given desired location.

As shown in Figure 4.2, in general, a particle on a flat surface impacts with a velocity v_0 at a certain angle α_0. In order to solve for the subsequent motion, it is necessary to solve for the tangential and normal components of the velocity. If there is no impulse or friction in the tangential direction, this component will stay unchanged. Then, if a particle impact has no loss associated with the impact, the

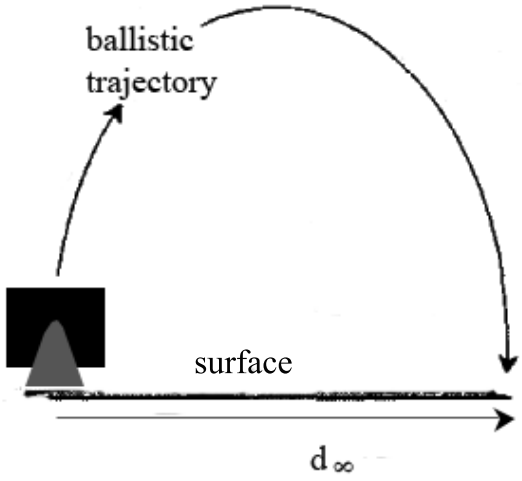

Figure 4.1: Hopping motion on asteroids.

normal velocity is reversed in direction but keeps the same magnitude. As a first step, the impact can be modeled as a perfectly inelastic impact with no sliding, that is $c_r = 0$ and $\mu = \inf$. This results in the particle staying at the same location when touching the surface, or getting "stuck" at impact. Similarly, one can look at the ideal elastic collision with $c_r = 1$. In this case, a particle impact has no loss associated with it.

However, since small bodies are most likely made of rubble pile, the particle will have a coefficient of restitution $c_r < 1$, and may be closer to 0. And, in the current application, the contact between the two objects will have a finite coefficient of friction, μ, adding an impulse opposite to the direction of motion. With a coefficient of restitution c_r and friction force μN at the impact point, where N is the normal reaction force, the normal and tangential components of the velocity after impact are,

$$v^1{}_n = c_r v_{n0} = c_r v_0 \sin(\alpha_0) \tag{4.1}$$

$$v^1{}_T = v_0 \cos(\alpha_0) - \mu(1 + c_r) v_0 sin(\alpha_0) \tag{4.2}$$

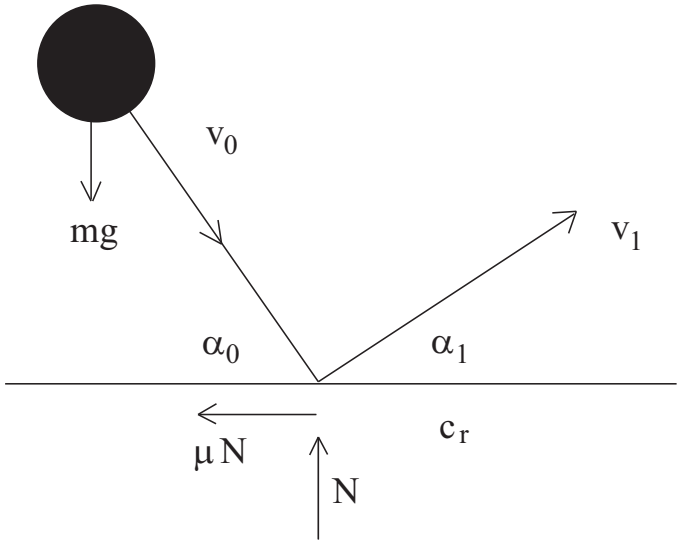

Figure 4.2: Dynamics of collisions for a particle on a flat surface with restitution and friction coefficient c_r and μ respectively.

Therefore, the velocity after impact has a new direction, α_1,

$$\tan \alpha^1 = \frac{{v^1}_n}{{v^1}_T} = \frac{c_r \sin(\alpha_0)}{\cos(\alpha_0) - \mu(1 + c_r)\sin(\alpha_0)} \tag{4.3}$$

A first order model of the dynamics of hoppers on the surface is to estimate the total time and distance from an initial jump to a stop due to friction and restitution coefficients. In order to do so, one needs to model the frame at the surface, and the non-uniform gravity field of a binary system.

4.2.2 Surface Modeling

In the numerical simulations of surface motion on asteroids, the dynamics of particles in the RF3BP is used, as well as the dynamics of impacts. A new surface frame is defined at each impact using the surface gradient and velocity direction.

The surface motion is modeled in three dimensions, with a tangential $\hat{\boldsymbol{t}}$, normal $\hat{\boldsymbol{n}}$, and cross track, $\hat{\boldsymbol{d}}$, frame fixed at the initial impact point on the surface, as shown in Figure 4.3. The normal is defined as being the unit vector in the direction of the

surface gradient,

$$\hat{\boldsymbol{n}} = \frac{\boldsymbol{\nabla} S}{|\boldsymbol{\nabla} S|}, \tag{4.4}$$

where S is the ellipsoid surface function expressed as $S = x^2 + \frac{y^2}{\beta^2} + \frac{z^2}{\gamma^2} - 1 = 0$. Note that this provides the boundary conditions the dynamics. The tangential direction is then defined as the unit vector perpendicular to the velocity,

$$\hat{\boldsymbol{t}} = \frac{\hat{\boldsymbol{t}} \times \boldsymbol{V}}{|\hat{\boldsymbol{t}} \times \boldsymbol{V}|}, \tag{4.5}$$

where $\boldsymbol{V}$ is the impact velocity expressed in the binary fixed frame, or the RF3BP. The cross track unit vector is obtained from orthogonality of the two first unit vectors,

$$\hat{\boldsymbol{d}} = \hat{\boldsymbol{t}} \times \hat{\boldsymbol{n}}. \tag{4.6}$$

Note that the cross track unit vector is always tangent at the impact point in the direction of the velocity but that the total acceleration can act in an arbitrary direction.

The velocity components computed after impact can be converted back to the RF3BP frame for numerical integration until the next impact. Having defined the unit vectors at the surface of the ellipsoid with respect to the rotating binary fixed frame, the rotation matrix of cosines is used to transform the resulting velocity from the surface frame to the RF3BP frame.

4.2.3 Effect of a Non-Uniform Gravity Field

While the surface modeling above can be applied on the surface of any single asteroid or binary asteroid system, the major difference is in the gravitational field. The general assumption for impacts on a flat surface, as shown in Figure 4.2 is that the particle moves in a uniform gravity field. For a non flat surface, the

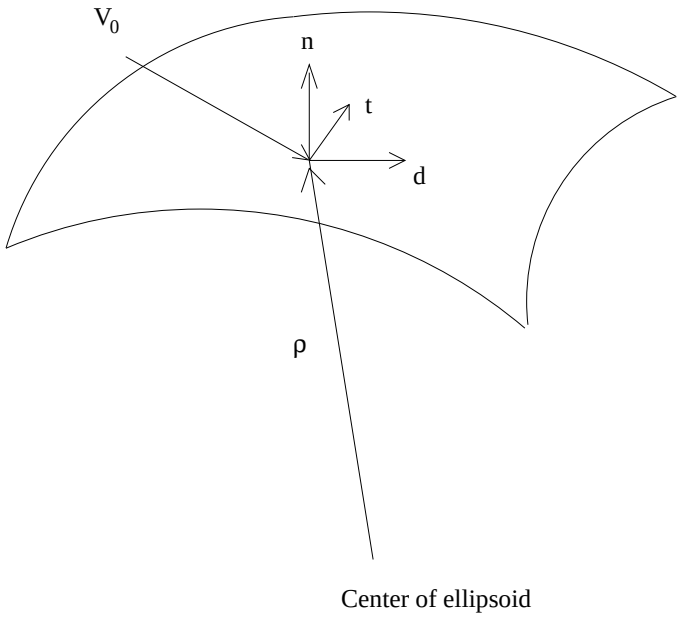

Figure 4.3: Geometry for 3D dynamical model of surface landers on small bodies.

gravity vector is dependent on the mass distribution of the body. For a sphere, the gravitational field is equivalent to the one of a point mass [15]. In the case of an ellipsoid, the gravitational field is not uniform, as shown in Figure 4.4. Note that the gray corresponds to the deviation of the gravity vector from the centroid, where the dark regions have the largest deviations. The ellipsoid has parameters $[\alpha; \beta; \gamma] = [1; 0.8; 0.6]$.

In the case of a binary system, the gravity field is surely not uniform either, and also not pointed toward the center of one of the bodies, as shown in Figure 4.5. In this case, the binary has a mass fraction of 0.95, with a distance of 9 units between the bodies and ellipsoid parameters of $[\alpha; \beta; \gamma] = [1; 0.8; 0.6]$. Note that only the ellipsoid is shown. The gray corresponds to the deviation of the gravity vector from the ellipsoid centroid, where the dark regions have the largest deviations.

The modeling for the surface dynamics on one of the bodies of a binary system needs to include the effect of the second body gravity field. Using the RF3BP model described in Chapter 3, the direction of the combined gravity field is found using the

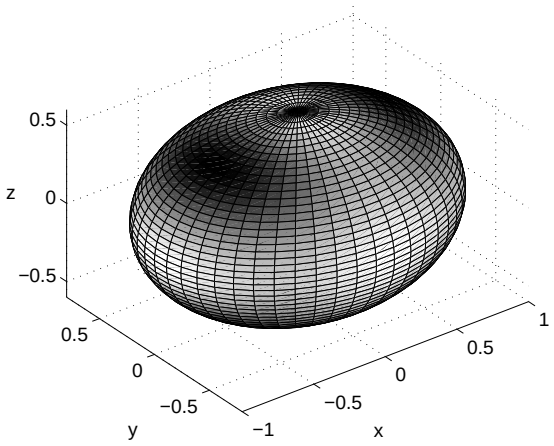

Figure 4.4: Gravity field of an ellipsoidal body. The gray scale corresponds to the deviation of the gravity vector from the centroid, where the dark regions have the largest deviations.

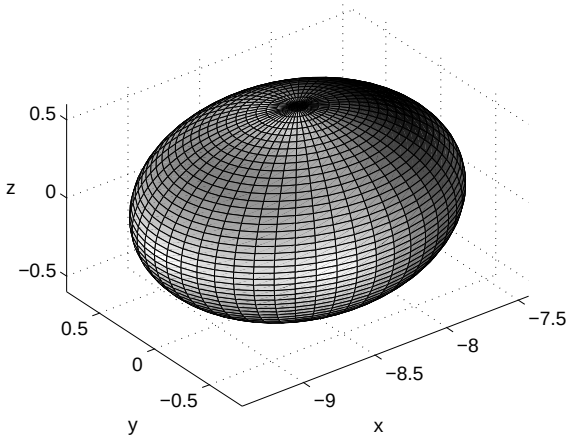

Figure 4.5: Gravity field of a binary system. The gray scale corresponds to the deviation of the gravity vector from the centroid, where the dark regions have the largest deviations.

equations of motion given by Eqs. (3.5-3.7),

$$g_x = \omega^2 x - \frac{\nu(x-(1-\nu)r)}{[(x-(1-\nu)r)^2+y^2+z^2]^{\frac{3}{2}}} - (1-\nu)(x+\nu r)R_{jx}, \tag{4.7}$$

$$g_y = \omega^2 y - \frac{\nu y}{[(x-(1-\nu)r)^2+y^2+z^2]^{\frac{3}{2}}} - (1-\nu)yR_{jy}, \tag{4.8}$$

and

$$g_z = -\frac{\nu z}{[(x-(1-\nu)r)^2+y^2+z^2]^{\frac{3}{2}}} - (1-\nu)zR_{jz}. \tag{4.9}$$

The following analytical method is developed for approximating the dynamics on a curved surface, under a non-uniform gravity field. The method approximates the local surface as a flat surface, taking the initial gravity vector as constant over that surface. For numerical simulations, the gravity vector needs to be calculated at every point of impact using Eqs. (4.7)-(4.9). Note that the gravity vector needs to be transformed to the surface frame defined in section 4.2.4.

4.2.4 Analytical Model for Dynamics on a Curved Surface in a Non-Uniform Gravity Field

Having defined a surface frame within the binary system environment, the geometry for modeling the surface dynamics is described in Figure 4.6. At the impact point, an object is again subjected to a local coefficient of restitution and surface friction factor, c_r and μ respectively. The incoming velocity $\boldsymbol{v}$, just before the next impact, is influenced by the general gravity vector $\boldsymbol{g}$ and the rotational acceleration. Note that the geometry is shown for a bounce in the normal - cross track plane, $\hat{\boldsymbol{n}} - \hat{\boldsymbol{d}}$. By approximating the local surface as a flat surface, that is considering the motion on a local tangent plane at the point of impact, it is possible to find general expressions for the time, distance and velocity components between jumps as function of the initial velocity and gravity vectors.

The normal component of the velocity is affected by the local coefficient of

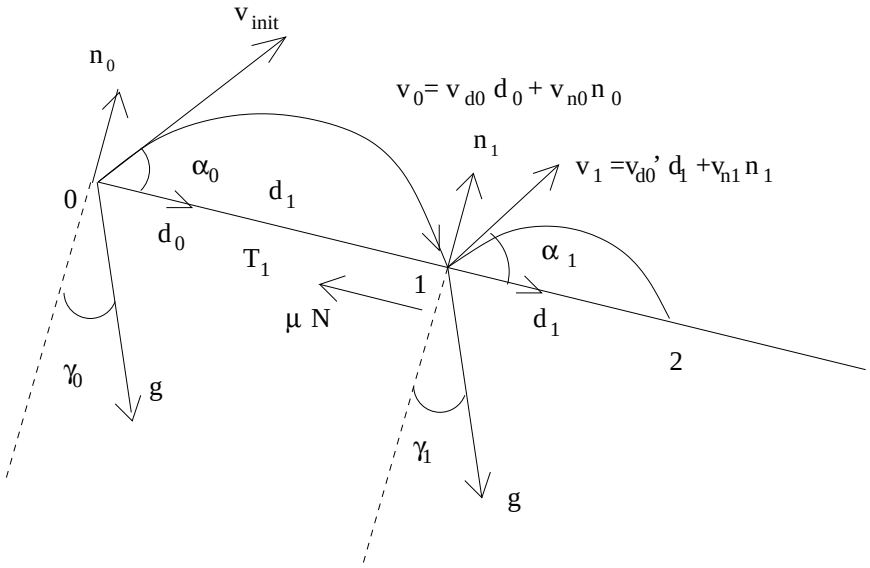

Figure 4.6: Dynamics of collisions for a particle on an inclined surface with restitution and friction coefficient c_r and μ respectively.

restitution, giving

$$v_{n_1} = -c_r v_{n_0}, \tag{4.10}$$

where v_{n_0} and v_{n_1} are the normal components before and after impact, respectively. In the tangential direction, the velocity expression is

$$v_{d_0}^{'} = v_{d_0} - \mu(v_{n_0} + v_{n_1}) = v_{d_0} - \mu(1 + c_r)v_{n_0}, \tag{4.11}$$

where $v_{d_0}^{'}$ and v_{d_0} are the tangential components before and immediately after impact, respectively. When the particle arrives at the next impact, the velocity is influenced by the gravity due to its general direction from the binary environment. Hence, the change in the cross track velocity v_{d_0} is written as

$$v_{d_0} = v_{0_d} + g_{d_0} t_{01}, \tag{4.12}$$

with

$$t_{01} = \frac{2v_{n_0}}{g_{n_0}}, \tag{4.13}$$

and where g_{n_0} and g_{d_0} are the normal and cross track components of the initial gravity vector.

Continuing the process, it is then possible to find general expressions for the velocities before and after impacts. In vector form, the velocity after the $n+1^{th}$ impact is expressed as

$$\boldsymbol{V'_{n+1}} = -c_r \hat{\boldsymbol{n}}\hat{\boldsymbol{n}} \cdot \boldsymbol{V_n} + (1 - \mu(1 + c_r)(\hat{\boldsymbol{n}} \cdot \boldsymbol{V_n}))[\boldsymbol{U} - \hat{\boldsymbol{n}}\hat{\boldsymbol{n}}] \cdot \boldsymbol{V_n}, \tag{4.14}$$

where $\boldsymbol{U}$ is the unity dyad. Similarly, the velocity just before the $n+1^{th}$ impact is influenced by the general gravity vector and the rotational acceleration. This velocity is given by

$$\boldsymbol{V_{n+1}} = -c_r \hat{\boldsymbol{n}}\hat{\boldsymbol{n}} \cdot \boldsymbol{V_n} + (1 - \mu(1 + c_r)(\hat{\boldsymbol{n}} \cdot \boldsymbol{V_n}))[\boldsymbol{U} - \hat{\boldsymbol{n}}\hat{\boldsymbol{n}}] \cdot \boldsymbol{V_n} + \Delta t[\boldsymbol{U} - \hat{\boldsymbol{d}}\hat{\boldsymbol{d}}] \cdot \boldsymbol{g}, \tag{4.15}$$

where

$$\Delta t = \frac{2|v_{n_0}|}{g_{n_0}}. \tag{4.16}$$

Note again that, because of the ellipsoidal shape, the gravity field is not uniform in the numerical simulations, whereas it is kept constant for this analytical model. Then, the distance covered between the n^{th} and $n+1^{th}$ hop is expressed as,

$$d_{n,n+1} = v'_{t_{n-1}} t_{n,n+1} + \frac{1}{2} g \sin\gamma_0 t^2_{n,n+1}. \tag{4.17}$$

The time of travel and the distance covered can be estimated using summations of the interval expressions given by Eqs. (4.16-4.17). Hence, in order to find the total time and distance from the first hit to the N^{th} hit, we express

$$t_{Total,N} = \frac{2v_{n_0}}{g_{n_0}} \sum_{n=1}^{N} c_r^{n-1} = \frac{2v_{n_0}}{g_{n_0}} \left(\frac{(1 - c_r^N)}{1 - c_r} \right) \tag{4.18}$$

and

$$d_{Total,N} = \frac{2v_{n_0}v_{0_d}}{g_{n_0}}\left(\frac{1-c_r^N}{1-c_r}\right) - \frac{2\mu v_{n_0}^2(1+c_r)}{g_{n_0}(1-c_r)}\left(\frac{(1-c_r^N)}{(1-c_r)} - \frac{(1-c_r^{2N})}{1-c_r^2}\right) + \frac{4g_{d_0}v_{n_0}^2}{g_{n_0}^2}\left(\frac{(1-c_r^N)}{(1-c_r)} - \frac{(1-c_r^{2N})}{1-c_r^2}\right) + 4\frac{\frac{1}{2}g_{d_0}v_{n_0}^2}{g_{n_0}^2}\frac{(1-c_r^{2N})}{1-c_r^2}. \quad (4.19)$$

Now letting $N \to \infty$ in Eq. (4.18), the time for the rover to reach a stop is

$$t_\infty = \frac{2v_{n_0}}{g_{n_0}}\left(\frac{1}{1-c_r}\right). \quad (4.20)$$

Similarly, summing Eq. (4.19) with $N \to \infty$, gives the distance traveled by the hopper to reach a stop, given by

$$d_{d,\infty} = \frac{2v_{n_0}v_{0_d}}{g_{n_0}(1-c_r)} + \frac{2v_{n_0}^2}{g_{n_0}(1-c_r)^2}\left(-\mu c_r + \frac{g_{d_0}}{g_{n_0}}\right). \quad (4.21)$$

These two quantities should agree with numerical simulations for small hops. However, the numerical distance may have a certain tangential deviation from its initial start as opposed to the analytical result due to the non-uniform gravity vector and the effect of a rotating body. The next section looks into a range of hops in order to validate this analytical model and to investigate and review the general effect of the different parameters of the surface such as the coefficient of restitution and the friction factor, as well as the initial hopping conditions.

4.2.5 Validation and Numerical Analysis of Surface Motion

Figure 4.7 shows an ideal case of surface hopping, where the surface is frictionless and under elastic impacts. For physically meaningful results, the surface needs to be modeled with some friction, and allowing energy loss during impact. Typical values for these surface parameters are close to those of semisolid environment, with surface made of dirt and some loose gravel [101, 75]. The resulting motion is damped compared to Figure 4.7, as shown in Figures 4.8 and 4.9. In Figure 4.8, the particle moves along the equator on a surface having a friction of 0.1 and 0.5. The effect of

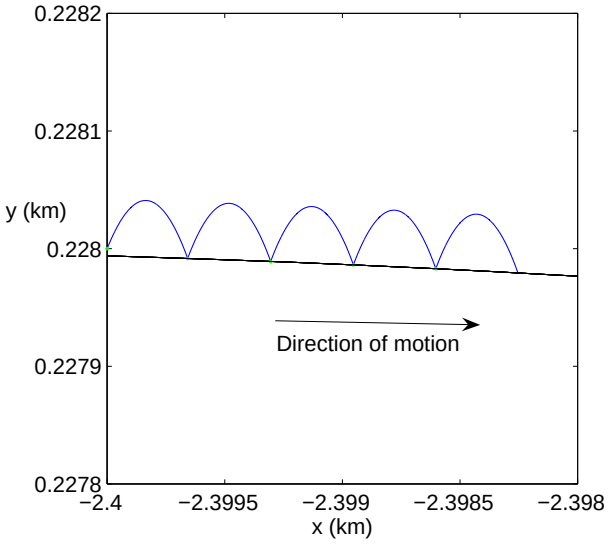

Figure 4.7: Elastic impacts for a particle moving on the surface of an ellipsoid.

both restitution and friction coefficients is shown in Figure 4.9, where each impacts looses about 75% of their initial kinetic energy. In addition, Figure 4.9 shows the effect of different initial velocities, also launching from different angles. For these simulations, the surface was modeled with a restitution of $c_r = 0.25$ and a friction factor of $\mu = 1$. As expected, the motion is damped quickly for all cases.

For the numerical cases shown in Figures 4.7-4.9, the total time is calculated using the numerical integrator scheme, adding every interval of time between hops. Similarly, the total distance traveled can be calculated, accounting for the curvature of the ellipsoid in this case. In order to validate the method developed using the analytical surface dynamics, these values of time and distance can be compared to Eqs. (4.20) and (4.19), that is t_∞ and $d_{d,\infty}$, respectively. It was found that, provided the jumps don't exceed 5 meters, the analytical model agree within 1 % compared to the numerical simulations. The amplitude of such a jump is represented in Figure 4.9 by the hop with initial velocity vector of $\boldsymbol{v} = [0.01; 0.05]$ corresponding to an initial velocity of 1-2 cm/s. These simulations were done for an asteroid size of 600 m $\times$ 500 m $\times$ 300 m. This also provides a stopping condition for numerical integration,

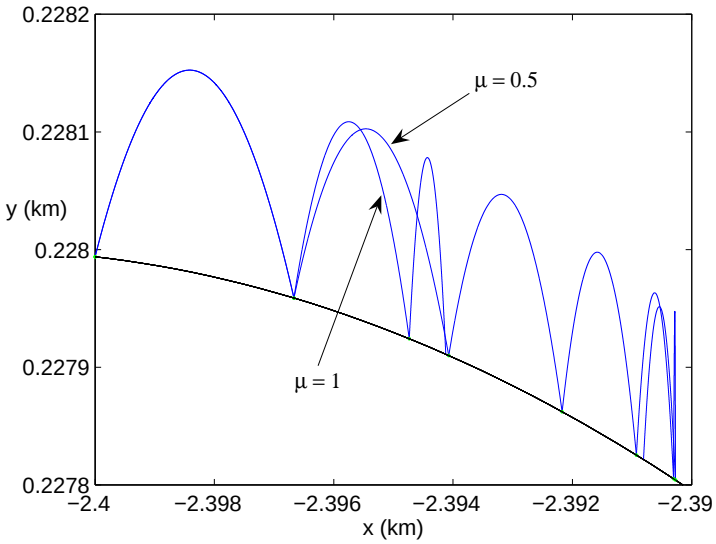

Figure 4.8: Top view of a particle moving along equator for perfectly elastic impacts under friction of 1 and 0.5.

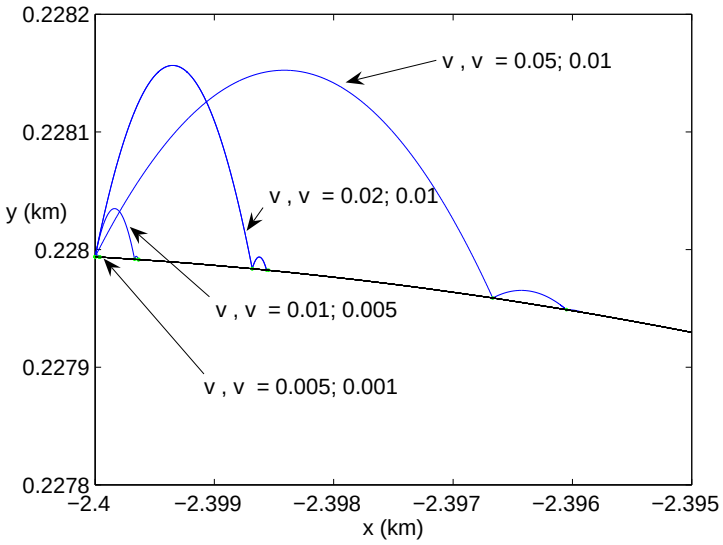

Figure 4.9: Effect of initial velocities on surface motion considering a surface modeled with a restitution and friction coefficients of 0.25 and 1, respectively.

avoiding the infinite number of bounces that occur when the craft settles.

4.2.6 Condition for Zero Velocity

Since there is friction between the particle and the surface, mathematically the frictional term could overcome the transversal velocity at impact and make the resulting transversal velocity to be negative, which is physically impossible. In the present analysis, the particle can only achieve a zero transversal velocity. In reality, a negative transverse velocity will lead to a lateral stop. Figure 4.8 shows simulations for varying friction factors. We see clearly that adding more friction slows down any dynamical motion rapidly.

For arbitrary initial conditions, the number of bounces can be computed in order for a vehicle to reach a stop. If N is the stopping bounce, then $v'_{t_{N-1}} = 0$. We want to compute the condition from Eq. (4.14) such that,

$$v_{0_d} - \frac{\mu v_{N_0}(1+c_r)(1-c_r^N)}{(1-c_r)} + \frac{2v_{N_0}g_{d_0}(1-c_r^N)}{g_{n_0}(1-c_r)} \leq 0 \tag{4.22}$$

where the N^{th} bounce makes the particle stop its lateral motion. Note that the particle may still have a normal velocity. Now, to compute N, the condition is that

$$v_{0_d} \leq \left[\mu(1+c_r) - 2\frac{g_{d_0}}{g_{n_0}}\right] \frac{v_{N_0}(1-c_r^N)}{(1-c_r)}. \tag{4.23}$$

It can be assumed that $\left[\mu(1+c_r) - 2\frac{g_{d_0}}{g_{n_0}}\right] > 0$, otherwise $N = 1$. Then,

$$\frac{v_{0_d}}{v_{N_0}} \frac{(1-c_r)}{\left[\mu(1+c_r) - 2\frac{g_{d_0}}{g_{n_0}}\right]} \leq 1 - c_r^N, \tag{4.24}$$

or

$$c_r^N \leq 1 - \frac{v_{0_d}}{v_{N_0}} \frac{(1-c_r)}{\left[\mu(1+c_r) - 2\frac{g_{d_0}}{g_{n_0}}\right]}. \tag{4.25}$$

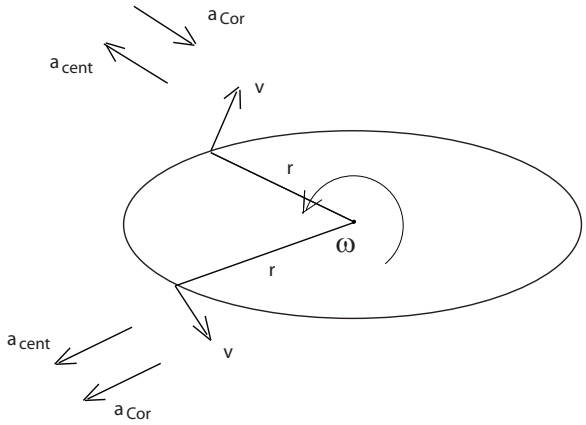

Figure 4.10: Influence of the Coriolis and centripetal accelerations.

Hence, given initial conditions, the stopping bounce N obtained is,

$$N \geq \frac{\ln\left[1 - \frac{v_{0_d}}{v_{N_0}} \frac{(1-c_r)}{\left(\mu(1+c_r) - 2\frac{g_{d_0}}{g_{n_0}}\right)}\right]}{\ln c_r}, \tag{4.26}$$

or, knowing the initial direction γ_0 as in Figure 4.6,

$$N \geq \frac{\ln\left[1 - \frac{v_{0_d}}{v_{N_0}} \frac{(1-c_r)}{(\mu(1+c_r) - 2\tan\gamma_0)}\right]}{\ln c_r}. \tag{4.27}$$

Having defined all mathematical tools for this analytical method to be valid and consistent, the next step is to look at the dynamics on the surface of a rotating body.

4.2.7 Influence of a Rotating Ellipsoid on the Surface Dynamics

On a rotating ellipsoid, a particle is influenced by the Coriolis and centripetal accelerations. As shown in Figure 4.10, on the side leading the rotational motion denoted by A, both the centripetal and Coriolis accelerations are pointed away from the body. The particle on the surface would then be assisted in its jump, allowing to cover a longer distance. On the other side, at B, the two accelerations are opposite to each other, which causes the particle to slow down.

In addition, for an ellipsoidal body, it is possible to find points on the surface

where an object could stay in equilibrium. The stability of these equilibrium points depends on the ellipsoid spin and shape parameters. One would expect that the dynamics of hopping robots on the surface of a small body are affected by these equilibria and their stability. Because of this, control of the dynamics of any surface landers may be required in order to investigate specific regions.

In [24], the authors use classical dynamics and geometrical analysis to investigate the stability of surface equilibrium points for a rotating ellipsoid. For convenience, some of their results are recalled here. The dynamics on the surface of a single rotating ellipsoid can be written using Lagrange coefficients,

$$\ddot{\bar{\boldsymbol{\rho}}} + 2\boldsymbol{\omega_r} \times \dot{\bar{\boldsymbol{\rho}}} + \boldsymbol{\omega_r} \times (\boldsymbol{\omega_r} \times \bar{\boldsymbol{\rho}}) = \frac{\partial U_e}{\partial \bar{\boldsymbol{\rho}}} + \lambda \boldsymbol{\nabla} S, \tag{4.28}$$

where $\bar{\boldsymbol{\rho}}$ is the nondimensional position vector of a particle on the surface relative to the ellipsoid center of mass, $\boldsymbol{\omega_r}$ is the ellipsoid spin, and U_e is the ellipsoid potential, as defined by Eqs. (2.18-2.20) in Chapter 2. Solving for equilibrium, three equilibrium points can be computed, P_1(1,0,0), $P_2(0, \beta, 0)$, and $P_3(0, 0, \gamma)$. Their stability satisfies the following conditions [24]. For P_1 to be stable, the ellipsoid needs

$$\begin{aligned} 0.5(R_{j\alpha} - \beta^2 R_{j\beta}) &< \omega^2(1 - \beta^2) \\ 0.5(R_{j\alpha} - \gamma^2 R_{j\gamma}) &< \omega^2. \end{aligned} \tag{4.29}$$

For P_2 to be stable,

$$\begin{aligned} 0.5(R_{j\alpha} - \beta^2 R_{j\beta}) &> \omega^2(1 - \beta^2) \\ 0.5(\beta^2 R_{j\beta} - \gamma^2 R_{j\gamma}) &< \omega^2 \beta^2. \end{aligned} \tag{4.30}$$

Finally, for P_3 to be stable,

$$0.5(R_{j\alpha} - \gamma^2 R_{j\gamma}) > \omega^2 \tag{4.31}$$

$$0.5(\beta^2 R_{j\beta} - \gamma^2 R_{j\gamma}) > \omega^2 \beta^2. \tag{4.32}$$

Note that two points cannot be stable at the same time. The R_j's expressions are derived from the ellipsoid potential and defined in section 2.3.

It is observed that, for small perturbations, a moving object on the surface of a rotating ellipsoid tends to stay closer to a stable equilibrium point and stay further away from an unstable one. Figure 4.11 shows the dynamics of a particle being dropped near the unstable pole, where the stable point is P_2 along the y axis of the ellipsoid. Note that the simulations are obtained for an ideal surface. It is clear that the particle stays away from the unstable region, even as it moves toward the opposite side. The particle generally tends to stay near the stable region around P_2. Figures 4.12 and 5.11 shows an example where the polar regions are stable. The curves shown are made of a series of hops under perfect surface conditions, where the disturbances are smaller in Figure 5.11. Again, note that, in order to see the general dynamical tendencies, the simulations were also obtained under perfect conditions. Figure 4.14 shows a simulation of surface dynamics under non ideal conditions, with restitution and friction coefficients of 0.5, although keeping the same asteroid parameters and spin rate as in Figure 5.11. In this case, it is clear that the general surface dynamics are influenced by the stability of the polar region.

An ellipsoid rotating at a fast spin rate or a more prolate ellipsoidal body are the typical cases to have the conditions satisfied for surface equilibria at the equator instead of at the polar regions. A particle situated at the same relative latitude as the case shown in Figure 4.14 will tend to stay away from the unstable polar region, and instead go toward the stable one at the equator, which is shown in Figure 4.15. The binary system 1999 KW4 provides an interesting real case example of

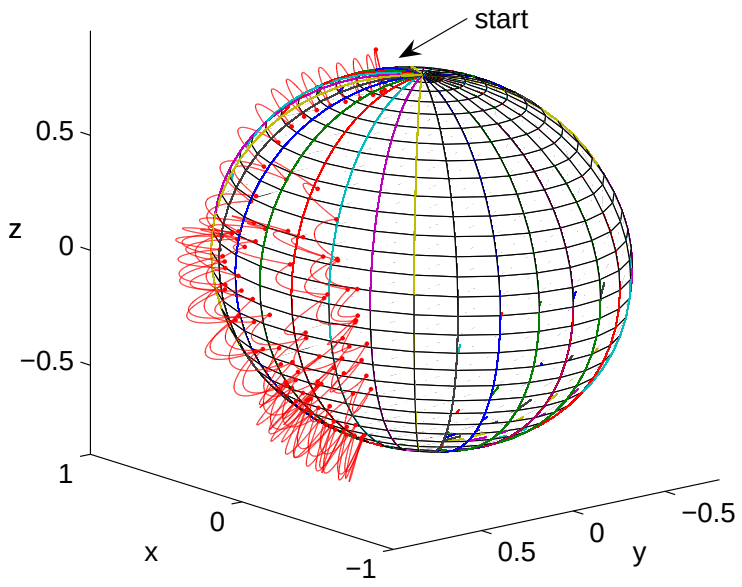

Figure 4.11: Dynamics around stable and unstable points of a rotating ellipsoid. The point along the y-axis, P_2, is stable.

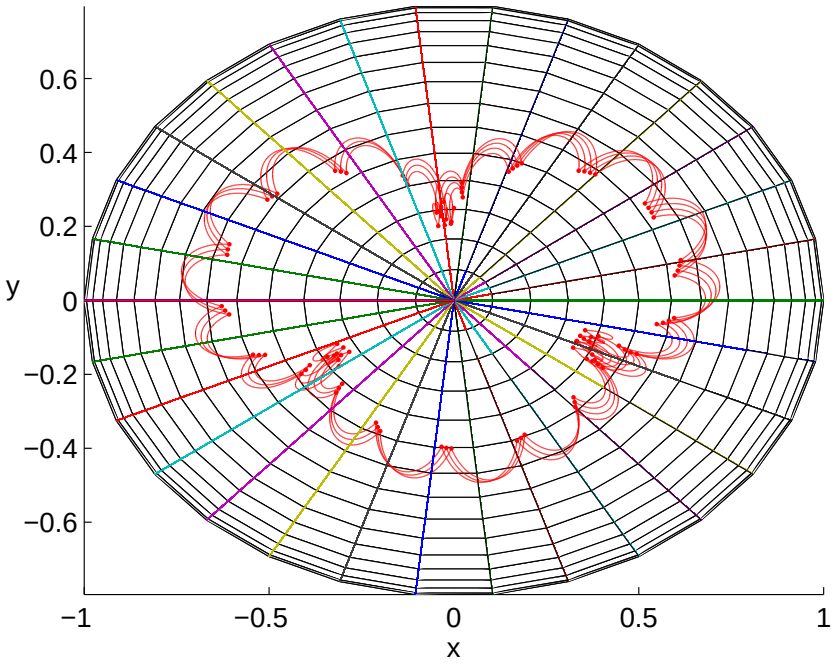

Figure 4.12: Dynamics around the stable polar point of a rotating ellipsoid, P_3.

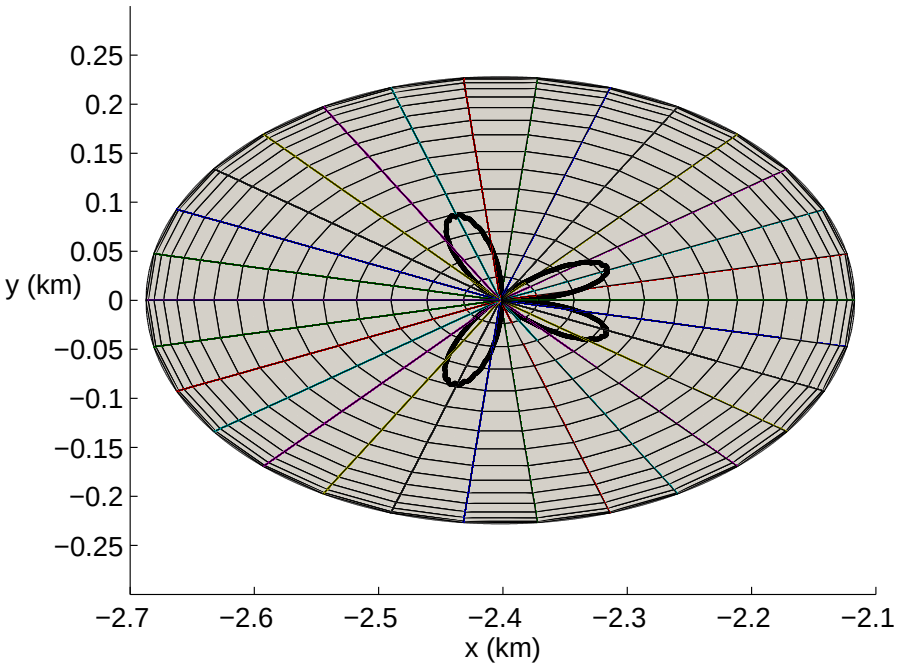

Figure 4.13: Top view of the dynamics close to a stable pole. The trace is made of hops under ideal conditions with zero friction and elastic impacts.

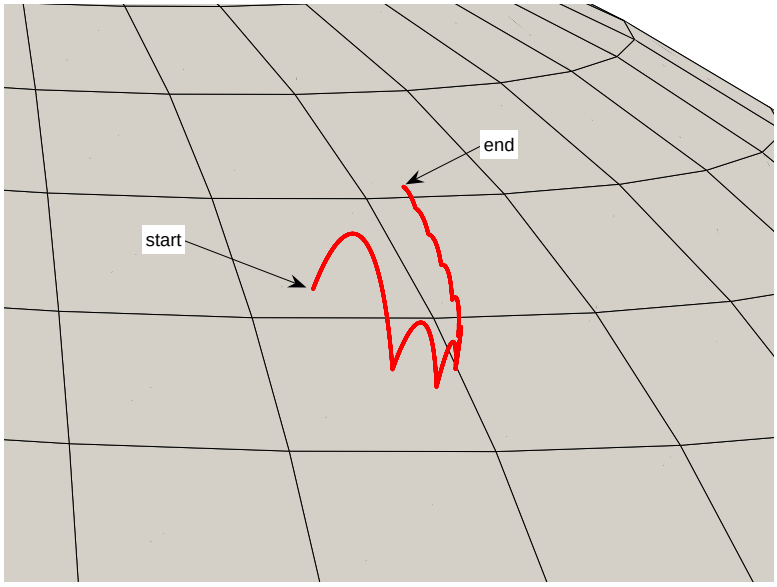

Figure 4.14: Dynamics close to a stable pole assuming restitution and friction factors of 0.5.

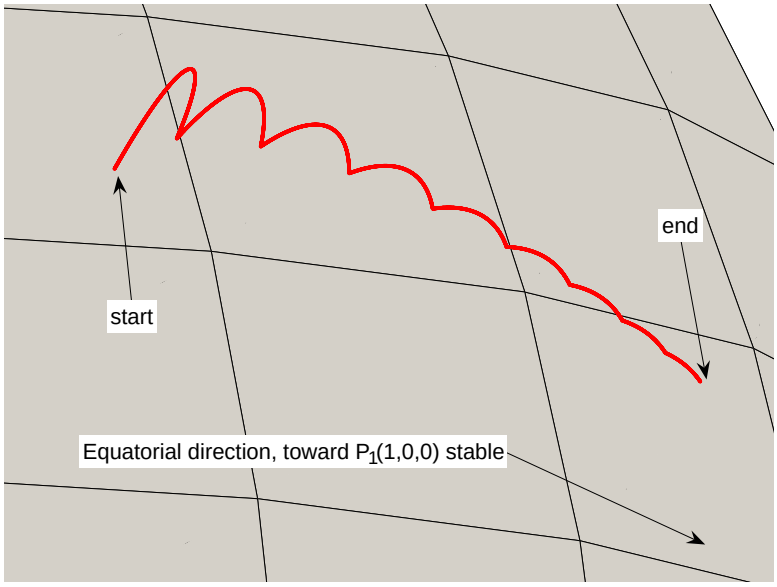

Figure 4.15: Dynamics close to a stable equatorial axis assuming restitution and friction factors of 0.5.

such situation [87], which is presented as a case study for a robotic mission design in the next chapter. In this case, the primary binary body was found to be in an almost disruptive state, which results in the asteroid having an equatorial bulge. In fact, the stability of surface equilibria explains current observations of asteroids where material is accumulated near the equator while some other asteroids have accumulation near the poles (also see [24]).

4.3 Control Algorithms

4.3.1 Motivation

The goal in surface investigation is to cover the maximum search area of the asteroid for mapping, imaging, and taking geological/scientific measurements or samples. To this date, only single probes were sent to small bodies. Current thoughts are to include more than one small landers or probes on the surface for better mapping, seismology, sampling, and to increase the mission reliability. Robots can be sent on a predefined grid and move accordingly. With the spacecraft in orbit, they could all

get feedback on their respective position on the surface.

In order to reach a desired location, hoppers could estimate the jumping distance to be covered and compute the required velocity. Having a dynamical model with knowledge of the environment, control algorithms can further be developed. There are many variables to consider in making efficient moves: time and distance to travel, fuel consumption, external disturbances, obstacles, collaborative tasks, etc. Too many jumps would consume time and energy while making high jumps could be hard to track. For efficient surface investigation, a discrete control law is developed for a single hopper, and the method is extended for multiple cooperative vehicles as they increase the range of scientific investigations and the probability of success. Many control strategies have been considered, either for unmanned aerial vehicles, cars, buses, boats, or underwater vehicles. Some of them involve leader-follower [28] or string and mesh-stable approaches [90, 66]. Other possible approaches include following virtual structures [3, 92] and potential methods [103]. These methods are difficult to implement in asteroid applications due to the discrete nature of the hopping dynamics.

The current control design is a leaderless control taking reference on sliding-mode control techniques [63, 102]. The next sections explain how the dynamical model can be used in the design a discrete control law for cooperative hoppers.

4.3.2 Control Law for a Single Hopper

Keeping in mind the surface dynamics model from section 4.2.4, the goal is to minimize the error associated with the travel. For doing so, a discrete control law can be developed acting on the error between hops. If the position at the n^{th} jump is represented in the cross track-tangential plane, $\hat{\boldsymbol{d}} - \hat{\boldsymbol{t}}$, by

$$\eta^n = \begin{bmatrix} d_d \\ \\ d_t \end{bmatrix}. \tag{4.33}$$

The $n+1^{th}$ location is then the sum of the previous location and the distance covered from jumping

$$\eta^{n+1} = \eta^n + \Delta\eta, \tag{4.34}$$

where $\Delta\eta$ is to be solved in such a way that the error on the position decreases in time. If the error at the n^{th} jump is defined as

$$\epsilon^n = \eta^n - \eta_d, \tag{4.35}$$

where η_d is the desired end position, then a control parameter K can be chosen such that the error decreases over each bounce, that is,

$$\epsilon^{n+1} = e^{-K}\epsilon^n. \tag{4.36}$$

Substituting for ϵ^{n+1} and ϵ^n in Eq. (4.36) gives

$$\eta^{n+1} - \eta_d = (\eta^n - \eta_d)e^{-K}. \tag{4.37}$$

Or, substituting Eq. (4.34) and solving for $\Delta\eta$ give

$$\Delta\eta = (\eta^n - \eta_d)\left[e^{-K} - 1\right]. \tag{4.38}$$

Hence, Eq. (4.38) determines the distance to be covered given a desired position and control parameter K. Using this result in the surface dynamics model, Eq. (4.21) can be inverted to find the initial velocity component. Hence, the cross track velocity component is given by

$$v_{0_d} = \frac{g_{n_0}(1-c_r)}{2v_{n_0}}\left[d_d + \frac{2v_{n_0}^2\mu c_r}{g_{n_0}(1-c_r)^2} + \frac{2v_{n_0}^2 g_{t_0}}{g_{n_0}^2(1-c_r)^2}\right]. \tag{4.39}$$

Therefore, a jump distance $\Delta\eta$ is computed from Eq. (4.38), with a given value of the control parameter K. Then, from Eq. (4.39), the initial velocities are computed in order to achieve that distance $\Delta\eta$. Some results are shown in

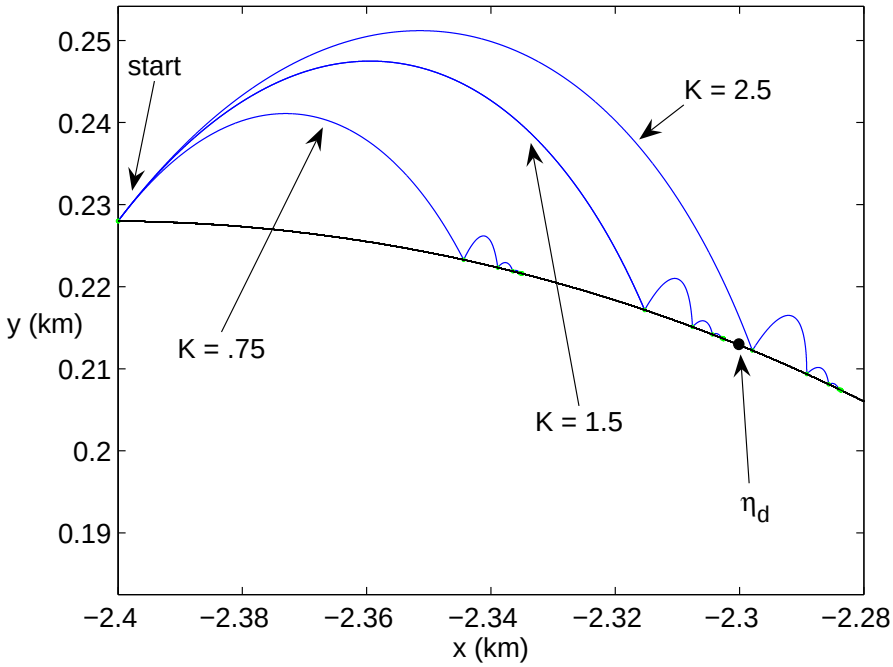

Figure 4.16: Controlled dynamics of a single rover with coefficient of restitution and friction factor set to 0.5. K are the control variables and η_d is the desired end position.

Figure 4.16, for a single hopper. We compare three different controlled dynamics, $K = 0.75$, $K = 1.5$ and $K = 2.5$, under the same surface conditions, with $c_r = 0.5$ and $\mu = 0.5$ corresponding to a semi-hard sandy surface. The desired end position is set at $x = -2.3\ km$ in the binary frame, labeled η_d in Figure 4.16. It is clear that increasing the control K reduces the number of hops necessary to reach η_d. However large values of the control parameter, such as $K = 2.5$, make the hopper overshoot η_d. Undershooting a target might be a better strategy. A hopper would need to relocate itself and estimate its required distance to reach η_d again. In this case, more jumps are needed in order to reach the objective, which takes more time but increases the chance of success.

To map the entire surface, a hopper would need to make a series of controlled jumps. In order to maintain low energy and stay within the influence of the small body, a threshold value on the launch velocity would be needed. After each jump,

the distance to be covered can be updated from the new position, and the procedure is re-iterated until the final position is reached. For better efficiency, a hopper formation would cover a larger area. Hence, a natural extension is to look at control of collaborative hoppers, which is discussed next.

4.3.3 Control Law for Cooperative Hoppers

For collaborative hoppers, sliding-mode control, also used for collaborative unmanned aerial vehicles, is applied. As described in [102], The goal is to have a formation to navigate to a desired end point while maintaining or achieving a certain configuration. For collaborative robots, the notation η_i^n is used for the i^{th} hopper at the n^{th} location. The $n+1^{th}$ location is then defined as

$$\eta_i^{n+1} = \eta_i^n + \Delta\eta_i, \tag{4.40}$$

where, again, the distance, $\Delta\eta_i$, is solved in such a way that the error on the position decreases in time. For the current application, the error expression needs to take into account the absolute error, i.e., the error with respect to the hopper's desired location, as well as the relative error for each hopper relative to its neighbors. The error term is then defined as,

$$\begin{aligned}\epsilon_i^n =&(\eta_i^n - \eta_{d,i}^n) + K_r(\eta_{i,j}^n - \eta_{i-1,j}^n + \eta_{d,i-1,j}) \\ &+ K_r(\eta_{i,j}^n - \eta_{i+1,j}^n + \eta_{d,i+1,j}) + K_r(\eta_{i,j}^n - \eta_{i,j-1}^n + \eta_{d,i,j-1}),\end{aligned} \tag{4.41}$$

where K_r is a weight factor giving precedence on the absolute or relative hopper end position.

Earlier work has shown mesh stability of a triangular formation as illustrated in Figure 4.17 [102]. Hence, for the current work, a triangular formation of three hoppers is investigated as a first step. As for the single hopper, a control parameter

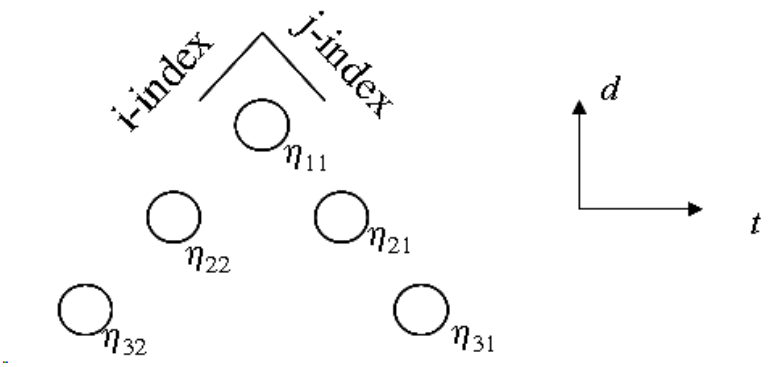

Figure 4.17: Triangular Formation for Collaborative Hoppers.

K is chosen such that the error decreases in time, that is

$$\epsilon_i^{n+1} = e^{-K}\epsilon_i^n. \tag{4.42}$$

And, using a control parameter K_r on the relative position of the hoppers, the error expression for the three hoppers are written as

$$\epsilon_1 = (\eta_1 - \eta_{d,1}) + K_r(\eta_1 - \eta_2 - \eta_{d,12}) + K_r(\eta_1 - \eta_3 - \eta_{d,13}), \tag{4.43}$$

$$\epsilon_2 = (\eta_2 - \eta_{d,2}) + K_r(\eta_2 - \eta_1 - \eta_{d,21}) + K_r(\eta_2 - \eta_3 - \eta_{d,23}), \tag{4.44}$$

and

$$\epsilon_3 = (\eta_3 - \eta_{d,3}) + K_r(\eta_3 - \eta_1 - \eta_{d,31}) + K_r(\eta_3 - \eta_2 - \eta_{d,32}). \tag{4.45}$$

Substituting for ϵ^{n+1} and ϵ^n from Eq. (4.42) for all three hoppers gives

$$\begin{aligned}(\eta_1^{n+1} - \eta_{d,1}) + K_r(\eta_1^{n+1} - \eta_2^{n+1} - \eta_{d,12}) + K_r(\eta_1^{n+1} - \eta_3^{n+1} - \eta_{d,13}) = \\ e^{-K}\left[(\eta_1 - \eta_{d,1}) + K_r(\eta_1 - \eta_2 - \eta_{d,12}) + K_r(\eta_1 - \eta_3 - \eta_{d,13})\right],\end{aligned} \tag{4.46}$$

$$(\eta_2^{n+1}-\eta_{d,2}) + K_r(\eta_2^{n+1} - \eta_1^{n+1} - \eta_{d,21}) + K_r(\eta_2^{n+1} - \eta_3^{n+1} - \eta_{d,23}) =$$
$$e^{-K}\left[(\eta_2 - \eta_{d,2}) + K_r(\eta_2 - \eta_1 - \eta_{d,21}) + K_r(\eta_2 - \eta_3 - \eta_{d,23})\right], \tag{4.47}$$

and

$$(\eta_3^{n+1}-\eta_{d,3}) + K_r(\eta_3^{n+1} - \eta_1^{n+1} - \eta_{d,31}) + K_r(\eta_3^{n+1} - \eta_2^{n+1} - \eta_{d,32}) =$$
$$e^{-K}\left[(\eta_3 - \eta_{d,3}) + K_r(\eta_3 - \eta_1 - \eta_{d,31}) + K_r(\eta_3 - \eta_2 - \eta_{d,32})\right]. \tag{4.48}$$

Then using Eq. (4.40) for $\Delta\eta_1$, $\Delta\eta_2$, and $\Delta\eta_3$, Eq. (4.46-4.48) become

$$\Delta\eta_1(1+2K_r) - K_r\Delta\eta_2 - K_r\Delta\eta_3 =$$
$$\eta_1^n(1+2K_r)(e^{-K}-1) + \eta_2^n K_r(1-e^{-K}) + \eta_3^n K_r(1-e^{-K})$$
$$+ n_{d,1}(1-e^{-K}) + n_{d,12}K_r(1-e^{-K}) + n_{d,13}K_r(1-e^{-K}), \tag{4.49}$$

$$\Delta\eta_2(1+2K_r) - K_r\Delta\eta_1 - K_r\Delta\eta_3 =$$
$$\eta_2^n(1+2K_r)(e^{-K}-1) + \eta_1^n K_r(1-e^{-K}) + \eta_3^n K_r(1-e^{-K})$$
$$+ n_{d,2}(1-e^{-K}) + n_{d,21}K_r(1-e^{-K}) + n_{d,23}K_r(1-e^{-K}), \tag{4.50}$$

and

$$\Delta\eta_3(1+2K_r) - K_r\Delta\eta_1 - K_r\Delta\eta_2 =$$
$$\eta_3^n(1+2K_r)(e^{-K}-1) + \eta_1^n K_r(1-e^{-K}) + \eta_2^n K_r(1-e^{-K})$$
$$+ n_{d,3}(1-e^{-K}) + n_{d,31}K_r(1-e^{-K}) + n_{d,32}K_r(1-e^{-K}). \tag{4.51}$$

Hence, solving for the three $\Delta\eta$'s gives the distance the three hoppers should jump to. As for the case of a single hopper, given a distance to cover, Eq. (4.21) can be inverted to find the initial velocity components for the required move. The overall motion is governed by the control parameters K and K_r. The next section investigates different scenarios of interest.

4.3.4 Results and Discussion on the controlled dynamics for surface motion

Applying the control law developed in the previous section, preliminary results are shown in Figures 4.18-4.20 for a collinear motion used as a validation case, and a triangular formation of three robots. In Figure 4.18, the three hoppers are released from a same point and move along the equator, each having a different set of final position as indicated in the figure. Note that the control scheme assumes the hoppers can update their position using star trackers and sensors before making the next hop. In Figure 4.19, the hopper formation achieves the desired configuration and position within a few hops using control parameters $K = 1.5$ and $K_r = 0.5$, for a longitudinal separation distance less than 100 meters. Reducing the control K_r makes the triangular path wider before reaching the desired position, which may be desired depending on the application.

In order to have more insight in the control efficiency, the distance to cover was increased by 3 in the simulation shown in Figure 4.20. Having a desired position far from the starting point, the dynamics of the asteroid has a more dominant influence on the dynamics and control of the hoppers. In the case shown in Figure 4.20, the asteroid has stable polar regions. It is clear that the hoppers are "attracted" by the polar regions, making slight curves toward the pole in their trajectory. Even though the following hop attempts to correct the situation, the hoppers 2 and 3 located closer to the polar regions are again attracted to it. This effect could make it impossible for a hopper to reach the desired position and configuration. Note that the paths shown in Figure 4.19-4.20 are made of a series of hops from bouncing on the surface, while the hops that are indicated represent controlled jumps.

Hence, the control developed above give good results for small motion, within 100 meters. For large distance to cover, having a higher gain K_r will keep the formation tight before reaching the final desired location, which may prevent the hoppers to

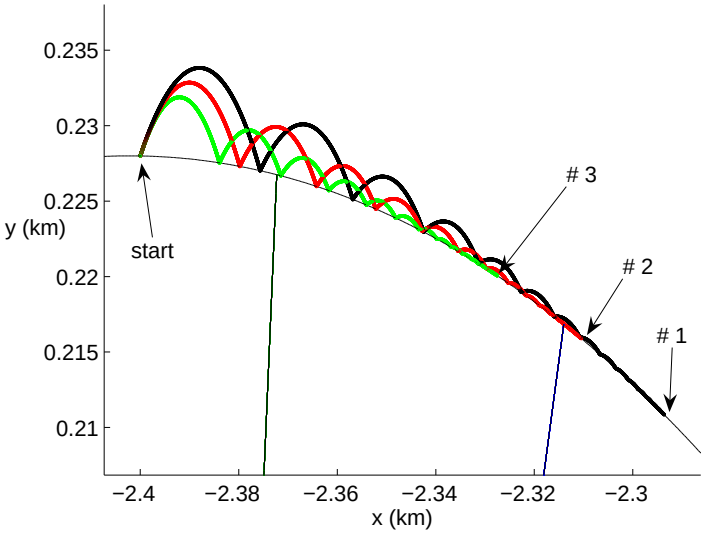

Figure 4.18: Controlled dynamics of a linear robot formation with coefficient of restitution and friction factor set to 0.5 and control parameters K=1.5 and K_r=0.5. Hoppers 1, 2, and 3 have reached their final position.

have their trajectory deflected by stable or unstable regions of the asteroid. However, further investigation is needed in order to design an optimal control system valid for longer travel distance and to possibly counteract stronger nonlinear perturbations from the asteroid's dynamics.

As shown in Figure 4.15, a more rapidly rotating body can have a stable equilibrium at the equator instead of the polar region. In this case, hoppers will tend to stay closer to either one of the principal axes at the equator. However, the disadvantage comes in when the asteroid spins close to its disruption rate, as in the case of Alpha in the binary system 1999 KW4 [87]. In this particular case, the analytical model looses its accuracy as even a low energy hop can make a particle, or a hopper, stay in orbit for a few revolutions.

The next chapter is an interesting application looking at a possible robotic mission design to the binary system 1999 KW4. All the methods developed in the previous chapters are applied during different phases of the mission, from approaching the system to investigating the surface of both bodies.

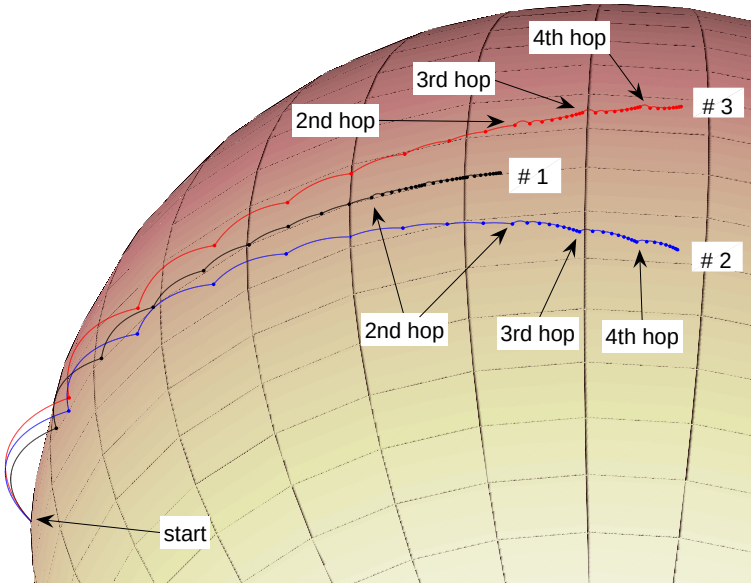

Figure 4.19: Controlled dynamics of a triangular robot formation with coefficient of restitution and friction factor set to 0.8 and 0.1, control parameters of K=1.5 and K_r=0.5, and a longitudinal distance to cover less than 100 meters. Hoppers 1, 2, and 3 have reached their final position.

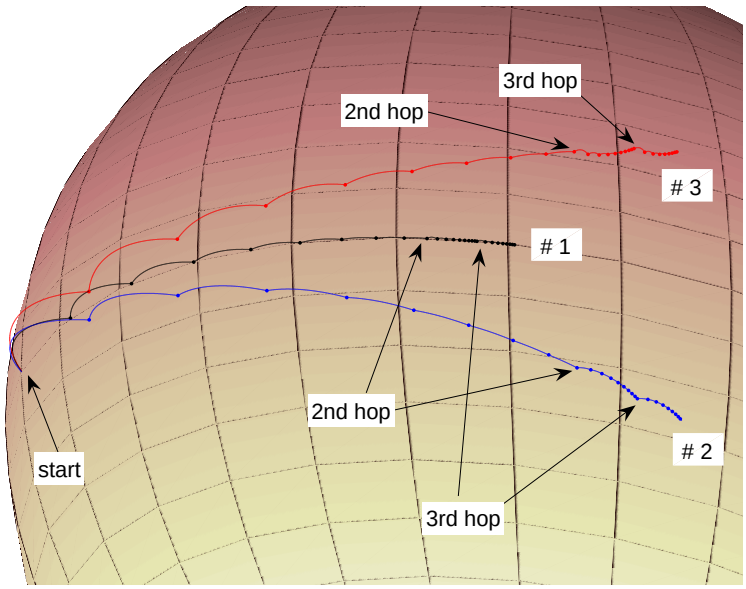

Figure 4.20: Controlled dynamics of a triangular robot formation with coefficient of restitution and friction factor set to 0.8 and 0.1, and control parameters K=1.5 and K_r=0.5, with a distance to cover of 200 meters while the polar region is stable. Hoppers 1, 2, and 3 have reached their final position.

CHAPTER 5

MISSION DESIGN TO A BINARY SYSTEM: APPLICATION TO 1999 KW4 AND OTHER CASE STUDIES

5.1 Motivation and Assumptions

Missions such as NEAR, Stardust, Hayabusa, Rosetta, and now DAWN have proven that a spacecraft can be sent to a small body at modest cost. From a science point of view, studying these systems provides a testbed for new technologies and contributes to our understanding of the solar system. As part of the planetary exploration effort, this section looks at the design of a mission to a binary asteroid system, taking 1999 KW4 as a case study. The objective is to define the requirements for the mission operations near the binary system or on the surface of the bodies. The mission phases are developed in order to take advantage of the binary system's dynamical features. For this, the dynamics of the F2BP, the RF3BP, and the surface motion of previous chapters can be integrated, extended, and specialized to KW4.

The mission is designed such that a spacecraft can approach the binary through the smallest primary, and place small landers on the surface for further exploration. Eventually, robots would hop to the side facing the primary, and then travel across the L_1 region using a simple jump to investigate the massive body. The next sections describe the reasoning for why this approach may be the best one. Each phase is then described in details, from approach to departure.

Since 1999 KW4 is one binary system among many, and may not be the most

easily accessible, the last section of the chapter compares this case study to others and describes how this approach is applicable and suitable to other systems.

5.2 1999 KW4 Parameters

The binary system 1999 KW4 is one of the few binary systems in the Near Earth Asteroids population observed by radar or photometry [64, 71]. It is located on an eccentric orbit crossing the path of Earth, Venus, and Mercury, with a semi-major axis of about 0.64 AU, eccentricity of 0.69, and inclination of 39°. Detailed models of both bodies are available [87, 64], as shown in Figure 5.1, and precise dynamical simulations of the system has been performed using geometrical analysis and Lie group computations [18]. However, the ellipsoid-sphere model is found to be a good approximation for the current work, where the dynamics developed in chapter 3 is used. The two bodies are referred to as Alpha and Beta, representing a massive sphere and a smaller ellipsoid, respectively.

The physical parameters of 1999 KW4 were found from high-resolution radar imaging. The distance between the body's centers of mass was found to be $r_b = 2.54$ km and the total mass of the binary system is $M_1 + M_2 = 2.472 \times 10^{12}$ kg, which gives $G(M_1 + M_2) = 1.65 \times 10^{-7}$ km^3/s^2. The binary system has a mass fraction of $\nu = 0.9457$, an orbit period T of 17.458 hrs, and an orbit rate of $\Omega = 1.00 \times 10^{-4}$ rad/s. Alpha has a radius of 0.0786 km while the Beta shape parameters are $[2\alpha : 2\beta : 2\gamma] = [0.57 : 0.455 : 0.343]$ km. From the orbital parameters, the distances of Alpha and Beta relative to their center of mass are $r_1 = 0.138$ km and $r_2 = -2.402$ km. Alpha itself has its own spin rate, with a period of 2.8 hrs, written also as $\Omega_\alpha = 6.23 \times 10^{-4}$ rad/s. Note that Alpha's spin doesn't affect the dynamics of the two bodies but it is a characteristic to consider in designing the mission. Beta is locked in a gravity gradient orbit which is represented by the F2BP in relative equilibria from section 2.4. This geometry is shown in Figure 5.2.

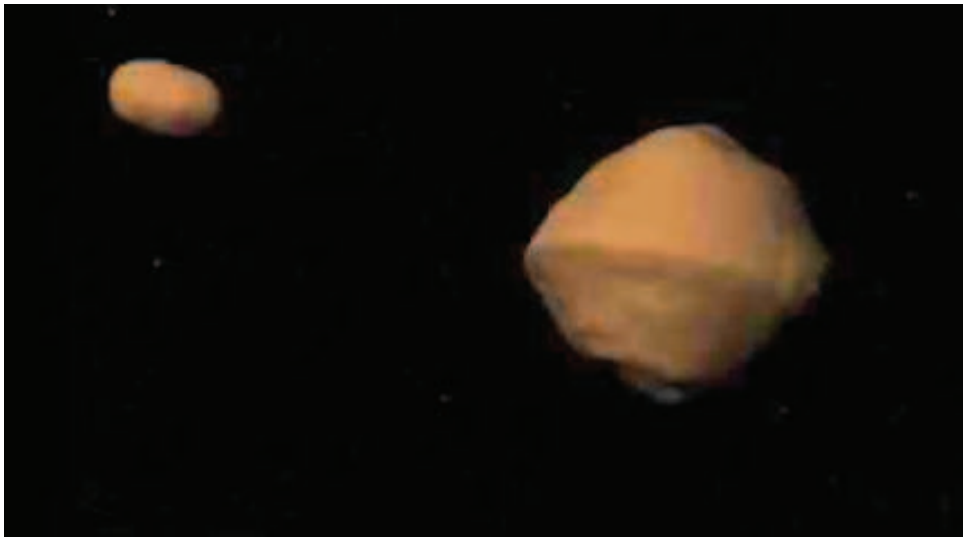

Figure 5.1: Model of the binary system KW4.

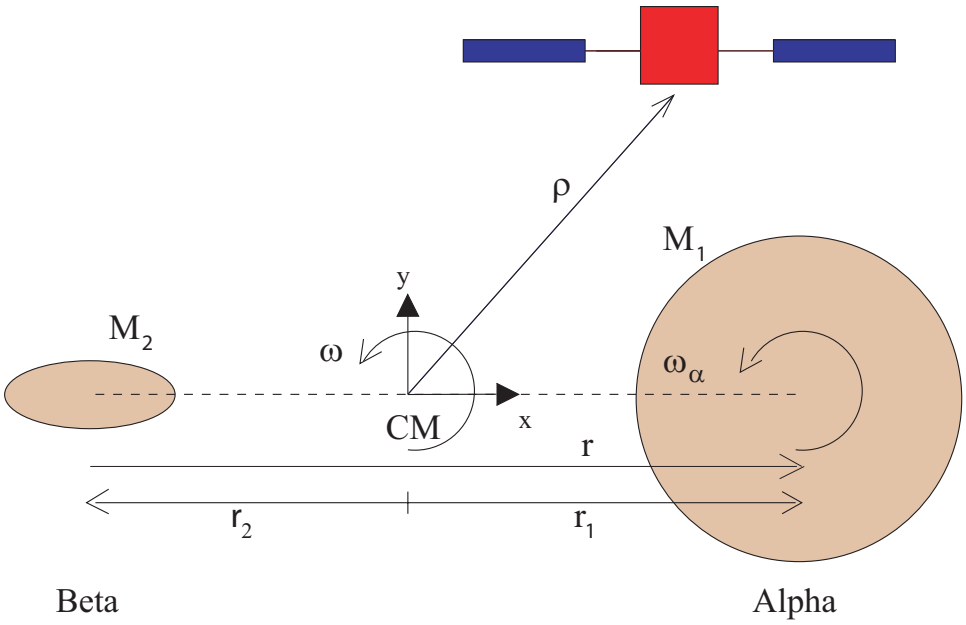

Figure 5.2: The Restricted Full Three Body Problem modeled for the binary asteroid system 1999 KW4. Note that $\nu \sim 1$ and Alpha has its own spin rate different than the binary orbit rate. Beta keeps the same configuration with respect to Alpha.

To work with non-dimensional units, the scaling length and time are defined as $\alpha = 0.57/2$, and $n = \sqrt{(\frac{G(M_1+M_2)}{\alpha^3})} = 2.67 \times 10^{-3}\ rad/s$. The non-dimensional distance between the bodies becomes $r = 8.9123$, and the rotation rate of the system is then $\omega = 0.0377$. Note that ω agrees with the angular velocity of the F2BP in a relative equilibrium given by Eq. (2.27). For Alpha, the non-dimensional spin rate is then, $\omega_\alpha = 0.233$.

The next sections explain how the energy constraints and zero-velocity curves are used as a base for a mission design to such a system.

5.2.1 Equilibrium Points, Stability and Jacobi Constant

The collinear equilibrium solutions are solved using Eq. (3.19) with $y = 0$ and $z = 0$. For the equilateral solutions, one needs to compute them numerically with the known results of the R3BP taken as a first guess. Looking at the stability conditions given by Eqs. (3.33), as expected, the collinear points are unstable. And, as expected, the results indicate that L_1 is outside the ellipsoid. In addition, for the mass fraction of 1999 KW4, $L_{4,5}$ are also unstable. Following the convention on the Lagrangian points notation given in Figure 3.4, the results on Lagrangian points, their associated Jacobi constant, and their respective stability are listed in Table 5.1.

To have better insight on the allowable regions of motion around 1999 KW4, Figure (5.3) shows the zero-velocity curve plot for 1999 KW4. The mission phases are described in the following.

Lagrangian Points	Distance km (normalized)	Jacobi $10^{-7}\ km^2/s^2$ (normalized)	Stability
L_1	$-1.777(-6.236)$ 0 0	$-1.121(-0.194)$	no
L_2	$2.594(9.100)$ 0 0	$-0.993(-0.172)$	no
L_3	$-3.140(-11.016)$ 0 0	$-1.097(-0.190)$	no
$L_{4,5}$	$-1.1318(-3.971)$ $\pm 2.195(7.704)$ 0	$-0.959(-0.166)$	no

Table 5.1: Lagrangian points for the binary system 1999 KW4 with corresponding Jacobi constants and stability.

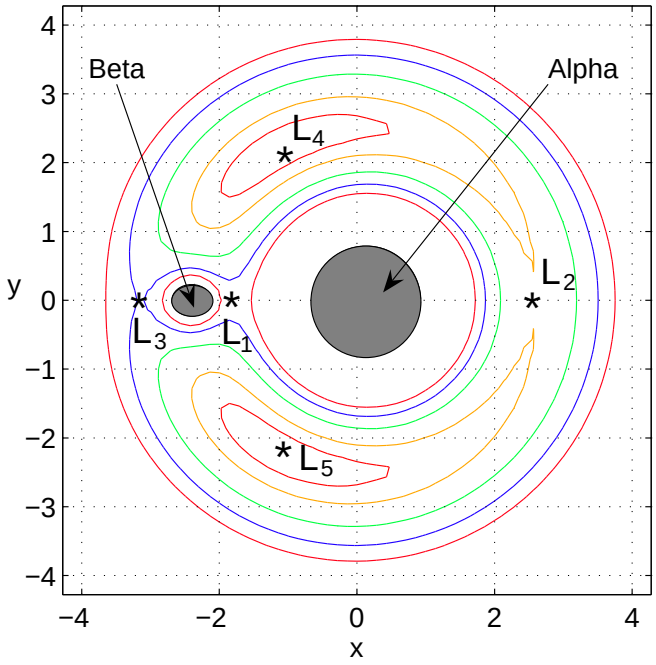

Figure 5.3: Zero-velocity curve plot for 1999 KW4 with $r = 2.54\ km$. The circle and ellipse around α and β represent the bodies.

5.3 Mission Design

5.3.1 Approach Strategy

Since the orbit of 1999 KW4 crosses the path of Earth, the binary periodically comes close to the Earth. The next close approaches are in 2018, 2019, and especially in 2036, with close approach distances of 11.7×10^6 km, 5.18×10^6 km, and 2.3×10^6 km, respectively [31]. Unfortunately, KW4 is in the low end of the available systems due to its orbital parameters, a combination small semi-major axis, large eccentricity, and high inclination. It is estimated that the velocity required to reach KW4, also called ΔV, is on the order of 21.3 km/s [30]. The detailed trajectory analysis is left for future study and the following focuses on the operations close to the binary, which can also be applied to other systems as discussed in the second half of this chapter. For a system such as 1999 KW4, the following sections show that approaching through Beta first is the best option to consider, from both environmental stability and mission operations.

5.3.2 Insertion Retrograde Orbits Characteristics

Arriving at the binary system, the spacecraft can first be placed on a retrograde circular orbit around the binary system for better stability. Figure 5.4 provides an example of such orbit. At about 4 km from the system center of mass, the retrograde orbital speed is 0.203 m/s in the inertial frame with a period of 34.4 hrs, or 0.803 m/s in the rotating frame with a period of 7 hrs. Since the velocity of Beta is 0.27 m/s in the binary fixed space, the relative speed between the spacecraft and Beta is about 1.073 m/s.

The spacecraft can also use this outer orbit as a platform for the rest of the mission. An orbit inclination between 150^o and 180^o may facilitate communications between the hoppers and the spacecraft, as the spacecraft would be able to view the upper and lower hemispheres of Beta every 7 hrs. For the case shown in Figure

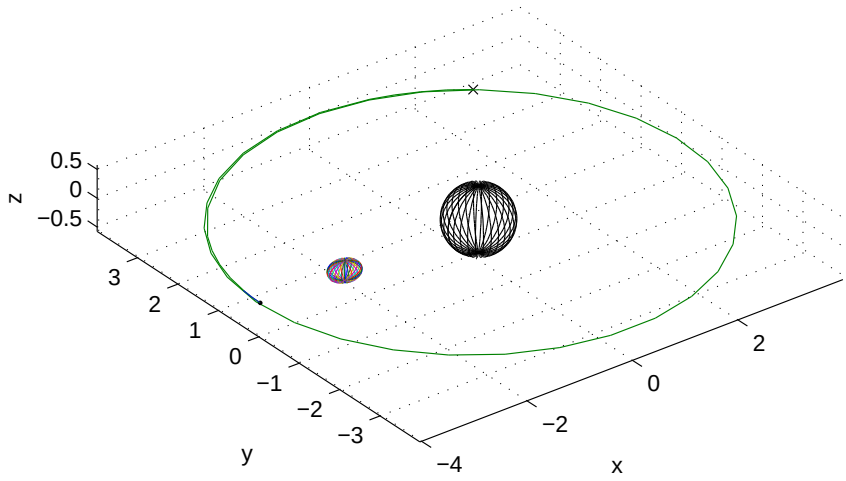

Figure 5.4: Retrograde orbit around the binary system 1999 KW4.

(5.4), the retrograde periodic orbits are unstable, although the orbits only have a weak instability. Figure (5.5) shows this same periodic orbit over a period of a year. As the orbits get closer to Beta, retrograde orbits are difficult to compute since Beta now has a more important influence.

If needed, the spacecraft can also stay temporarily in orbit around the small ellipsoid Beta, which is shown in Figure 5.6. At this altitude, about 1.35 km from the center of mass of Beta, the orbits are unstable. Closer orbits in the vicinity of Beta are also found, shown in Figure 5.7. Note that these orbits are also unstable.

5.3.3 Approach to Beta

The choice of the approach is made considering both asteroid environments of the binary system. Since the equilateral points L_4 and L_5 are unstable, they do not provide interesting approach options. From the characteristic parameters of KW4, Alpha has a more rapid spin and hence, a periodic motion relative to Beta. On the

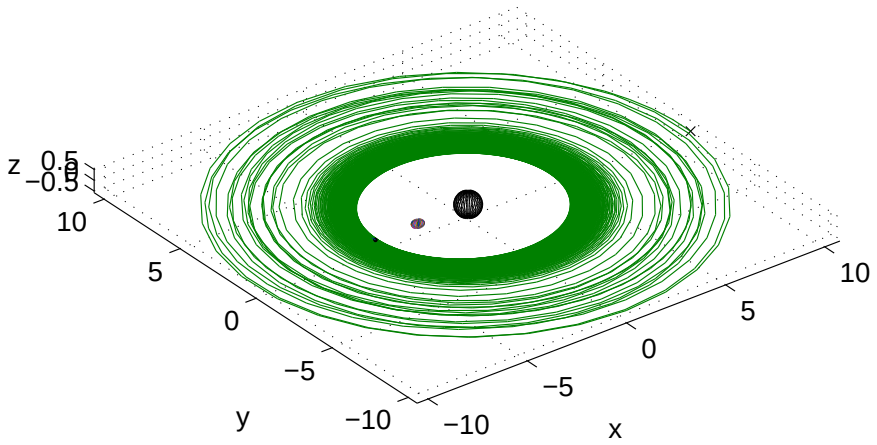

Figure 5.5: Retrograde orbit around the binary system 1999 KW4, over a year period.

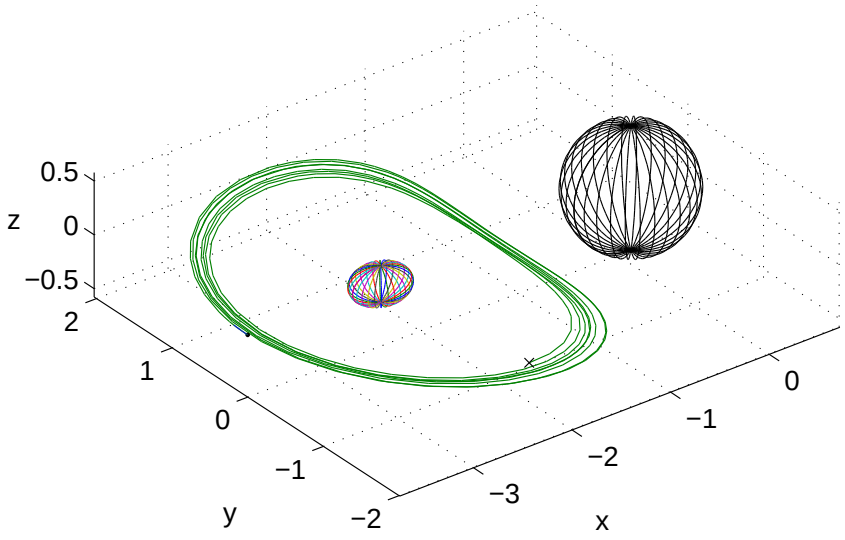

Figure 5.6: Unstable retrograde orbit around Beta, secondary body of 1999 KW4, 1.35 km from Beta's center of mass.

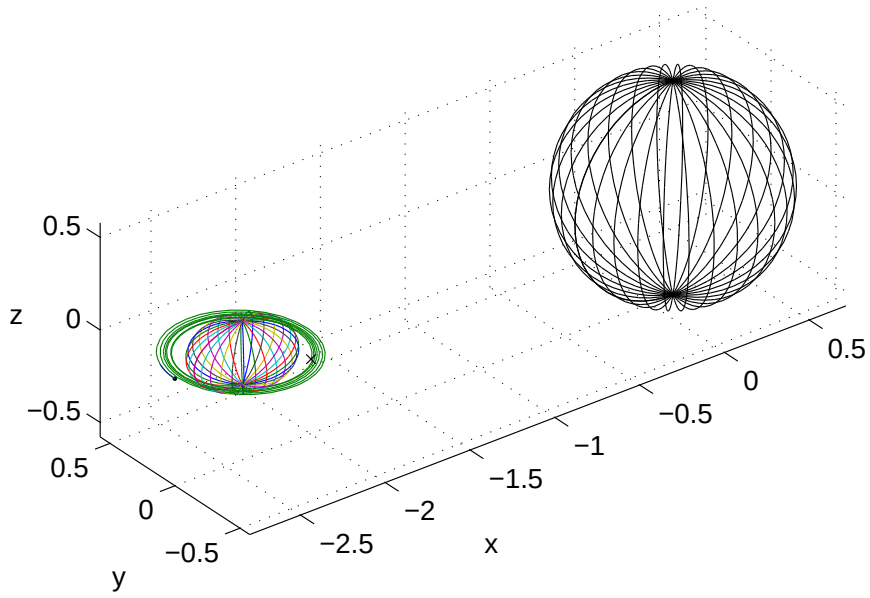

Figure 5.7: Unstable retrograde orbit near Beta, secondary body of 1999 KW4, 0.5 km from Beta's center of mass.

other hand, being in relative equilibrium configuration, Beta has a fixed attitude relative to Alpha. Hence, Beta would provide a more stable landing site. In addition, its Lagrangian point L_3 is the first to open after L_1, as defined in Figure 3.4. This is as expected from the observations made in section 3.2.3 since KW4 has a large mass ratio. Hence, taking these facts into consideration, the spacecraft approaching the binary system through L_3, on the side of Beta, is the best approach to take. This also limits the probability of escaping from the system as the spacecraft could only exit from the same entrance region.

Figure 5.8 provides an example of an insertion trajectory going through L_3 and landing on Beta. From the orbiting platform, the spacecraft could eject the robots with a simple spring mechanism while staying on this orbit for the remaining of the mission. Near the crossing point between the landing trajectory and the spacecraft orbit in Figure 5.8, the velocity of the robot would need to be 0.263 m/s oriented

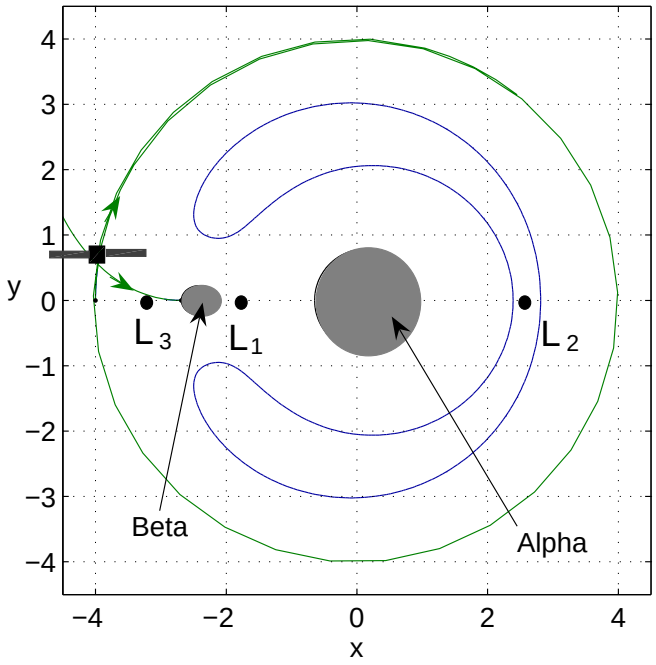

Figure 5.8: Binary system approach of a spacecraft through L_3.

at 45.6^o from the binary axis line. Hence, from simple relative motion, the ejecting velocity Δv is found to be 1.27 m/s oriented at 81.4^o from the binary axis line. The impact speed for this landing trajectory is 0.38 m/s in the binary fixed frame. Note that this example has not been optimized. The design and mission goals may influence landing velocities.

5.3.4 Surface Investigation of Beta

As the gravity is low, a lander on the surface will in general bounce several times before settling. In order to escape, a hopper on Beta would need to jump at a speed higher than 0.65 m/s relative to Beta, or about 0.2 m/s in the rotating frame, which opens regions exterior to the large encircling orbits of the system in Figure 5.3. Instead, by maintaining a low energy state, the hoppers would be restricted to a region close to Beta, as shown in Figure 5.9.

Landing on one end of Beta, a possible scenario is for the hoppers to be sent

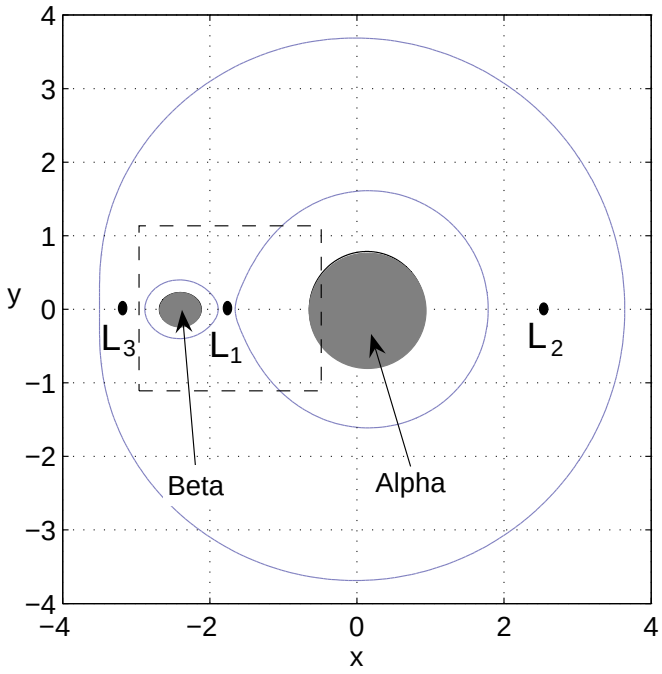

Figure 5.9: Regions of motion restricted to Beta and Alpha only.

to the other end of the small asteroid, maintaining an equally spaced grid between them. Figure 5.10 provides a close up view of the bouncing dynamics. Note that the trajectories shown are simulations of the nonlinear equations. As described in section 4.2.7, the centripetal and Coriolis accelerations influence the dynamics of landers. Being on the leading edge, a hopper can make a larger jump. In order for the landers to communicate and update their position, the spacecraft in orbit can be used to transmit scientific data.

The dynamics described in section 4.2.4 can be used to approximate small hops. In the case of KW4, referring to section 4.2.7 on surface equilibria of an ellipsoid, Beta is P_3 stable meaning its pole is a stable point. The dynamics of a hopper close to its pole is strongly influenced by its stability. As shown in Figure 5.11, hoppers near the pole would stay around this region. Note that the trajectory is made of small hops under ideal conditions. Robust control of the hoppers may be required in

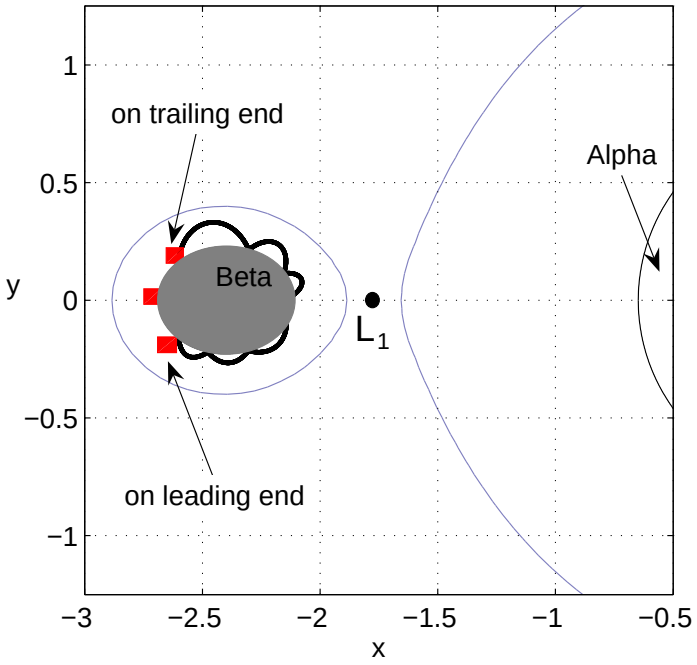

Figure 5.10: Close view of hoppers' distribution on Beta x-y plane of the rotating frame.

order to access the equatorial regions, or leave a stable pole.

Using the dynamics and control algorithm developed in Chapter 4, Figure 5.12 shows a simulation of hoppers traveling on the surface, surveying one end to the other along the equator. In this case, three hoppers released on the L_3 side move from their initial position to achieve a triangular formation and continue to the other end. The trajectories shown are made of a series of bounces from the low gravity environment. As one can see, the dynamics is not perturbed near the equator. After a few hops, the hoppers have achieved the desired configuration although the slight curve in the trajectory of hoppers 2 and 3 indicates the influence of the rotating ellipsoid having stable poles. Note that, since a hopper will bounce a few times before reaching a stop, it is assumed that the hoppers can update their position to evaluate the required jumping velocity. For safety of the operation, a threshold value was set to insure low enough velocities on the surface of Beta.

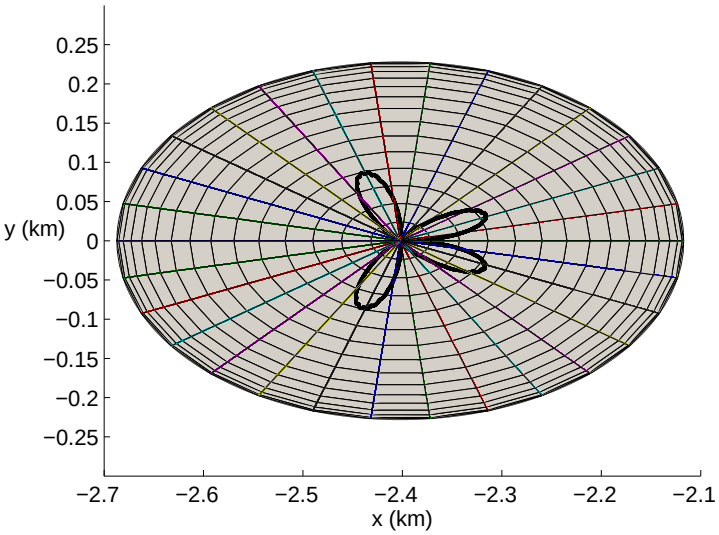

Figure 5.11: Top view of the dynamics close to the stable pole of Beta.

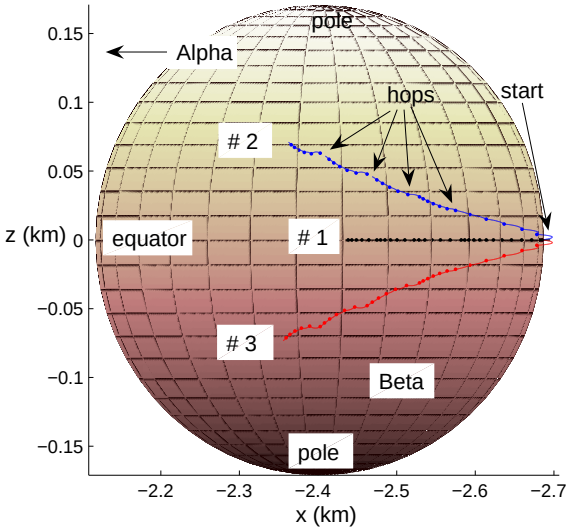

Figure 5.12: Controlled dynamics of a triangular formation of hoppers, surveying one end to the other along the equator. Hoppers 1, 2, and 3 have achieved their formation. Their trajectory is deflected due to Beta having stable pole regions.

5.3.5 Transition from Beta to Alpha

One unique feature of a binary asteroid system is the possibility to transit from one body to the other from a simple jump. As the hoppers reach the other end of Beta, facing Alpha, transition to Alpha is possible provided that the Jacobi value of the hopper is higher than that of L_1. As outlined in section 3.2.5, knowing the conditions for transit and non-transit trajectories from linear investigation at L_1, the system can be integrated backward and forward in time in order to find initial and final conditions on the surface of either body. To insure a vehicle is still trapped within the binary system, its velocity needs to be smaller than 0.65 m/s on Beta or smaller than 0.9 m/s on Alpha in the binary frame.

Figure 5.14 shows a concrete example of a possible transit. At A, the hopper jumps at a speed of 0.185 m/s oriented at 9.6^o from the x axis, in the frame rotating with the binary system. Arriving at Alpha, the landing velocity in the binary fixed frame is 0.16 m/s, at 12.4^o. Considering that Alpha is spinning, the surface velocity on Alpha is given by $(\Omega_\alpha - \Omega)r_c = v_s$ in the binary rotating frame, where r_c is the radius of the sphere. For 1999 KW4, this tangential velocity v_s is 0.40 m/s. Hence, the total velocity at B is 0.56 m/s, which is below the velocity limits for escape. Other possible transfer trajectories are shown in Figure 5.14, from changing the surface launching conditions. A non-transfer trajectory is also shown, jumping towards the other body at first but not having proper conditions to transit.

The transition opportunity given by the environment of 1999 KW4 is also one additional reason for making the landers go from Beta to Alpha instead of the opposite. Since Alpha has its own spin faster than their mutual orbit, its periodicity relative to Beta makes the launch window small. On the other hand, arriving at Alpha is not an issue in terms of timing, and the robots can continue the surface investigation. However, because of Alpha's spin, special energy consideration needs to be investigated, and is described next.

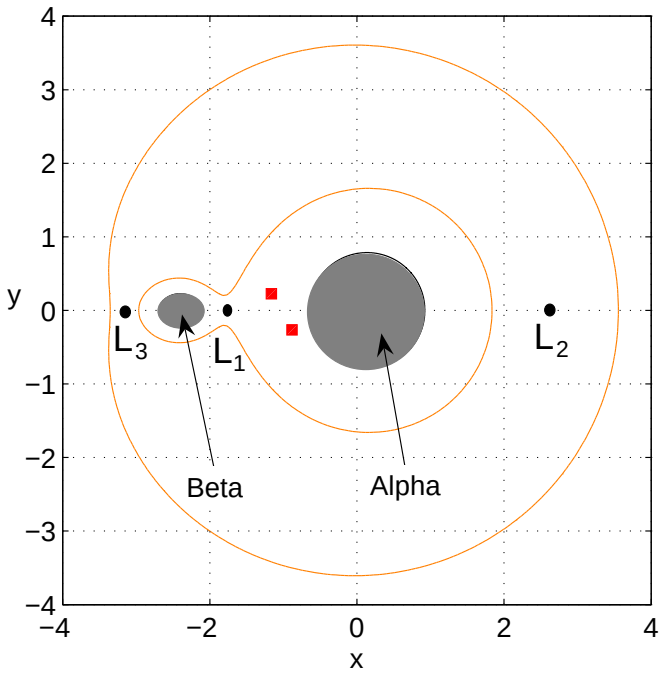

Figure 5.13: Transition to Alpha.

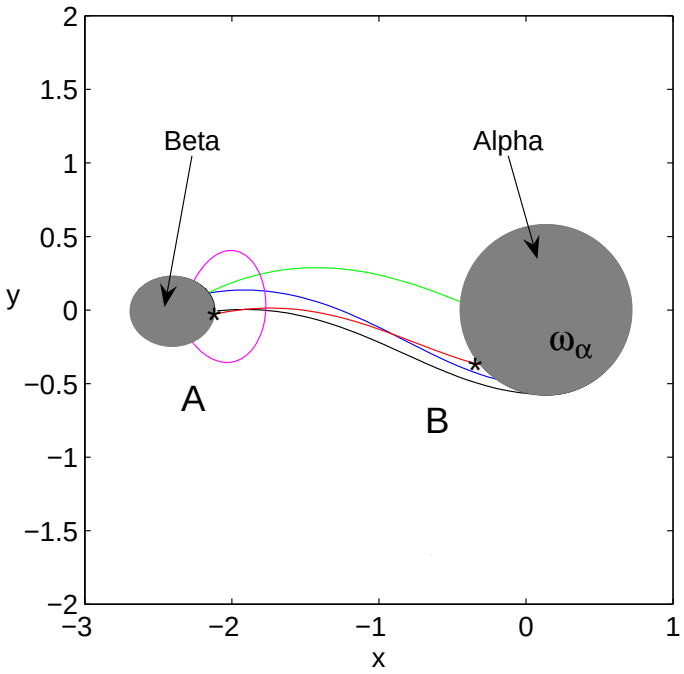

Figure 5.14: Transition and non-transition paths from Beta to Alpha.

5.3.6 Energy Constraints on Alpha

It is useful to first look at the energy involved for an object being on the surface, and rotating with Alpha. For a circular orbit about Alpha, which is 0.786 km in radius, the velocity in the Alpha frame is computed from

$$v = \sqrt{\frac{\mu_\alpha}{r_c}} = 0.445 \quad m/s, \tag{5.1}$$

where $\mu_\alpha = GM_1 = 1.5599 \times 10^{-7}\ km^3/s^2$. Now, from Alpha's spin itself, a particle would have a velocity of

$$v_\alpha = \omega_\alpha r_c = 0.490 \quad m/s. \tag{5.2}$$

Since these two velocities, v and v_α, are not far from being equal, one can infer that the particles near the equator are close to being in orbit about Alpha.

It is useful to investigate the zero-velocity curves near Alpha in order to verify if particles on the surface would be able to leave the system. If the spacecraft is located on the x-axis on Alpha toward the ellipsoid, that is, at $[-(0.786 - 0.138); 0]\ km$, its associated Jacobi constant is $C_{x1} = -2.0362 \times 10^{-7}\ km^2/s^2$. If it is located on the other side of the massive primary, at $[(0.786 + 0.138); 0]\ km$, its Jacobi constant is $C_{x2} = -2.0114 \times 10^{-7}\ km^2/s^2$. Since these C values are smaller than all the three values of the collinear points, these points have not opened up yet to the spacecraft on the surface of Alpha. Hence, there is no escape possible from orbiting close to the surface of Alpha.

In order to leave the system, from the zero-velocity curves shown in Figure (5.3), a spacecraft or particle would need a Jacobi integral higher than $C = -0.19$ or $C = -1.0996 \times 10^{-7}\ km^2/s^2$, which is referred to as C_{out}. This value corresponds to the large circular zero-velocity curve around the binary system. Inverting Eq.(3.14) for a spacecraft on the surface of Alpha, between the two primaries, the spacecraft would need to have a velocity of at least $v_{max\alpha} = 0.870\ m/s$ in the rotating frame in

order to have access to the outer region.

5.3.7 Surface Exploration of Primary Alpha

The surface model described for Beta can be applied to Alpha as well, together with the discrete control law algorithm. However, since Alpha is rapidly spinning, a hop at the equator can place a robot in orbit about it. A hopper would only need to jump with a velocity greater than 0.05 m/s relative to the surface of Alpha in order to stay in orbit around Alpha. With an energy state smaller than all three values of the collinear points, these points wouldn't have opened up yet and hence, there could be no escape possible from orbiting in the regions close to L_1 or L_2. The maximum velocity that a vehicle would need in order to escape the system is found to be 0.5 m/s relative to Alpha surface, or 0.9 m/s in the binary frame.

Since Alpha spins rapidly, faster than Beta, moving particles or landers on Alpha tend to "fall" toward the equator. In the current model, Alpha is modeled as a sphere. Surface motion on a sphere is different than for an ellipsoid. To have more accurate results, one would need Alpha to have parameters such as $[\alpha; \beta; \gamma] = [1; 1; 0.8]$ parameters. Considering the true shape of Alpha, mapping its effective gravity slopes as shown in Figure 5.15 shows that any loose particles on its surface would have a tendency to accumulate at the equator [87, 64]. The arrows indicate the angular deviation of the acceleration from the local downward direction due to gravity and spin. This makes it difficult to explore the polar regions. This would be of interest, however. Precise numerical simulations have also give more insights into the effect of Alpha having a more oblate mass distribution on the system orbital elements and the spin axis orientation [18].

5.3.8 Stable Periodic Orbits around Alpha

As for the binary reconnaissance orbits described in section 5.3.2, periodic orbits around Alpha can be computed. These orbits can be used as part of the

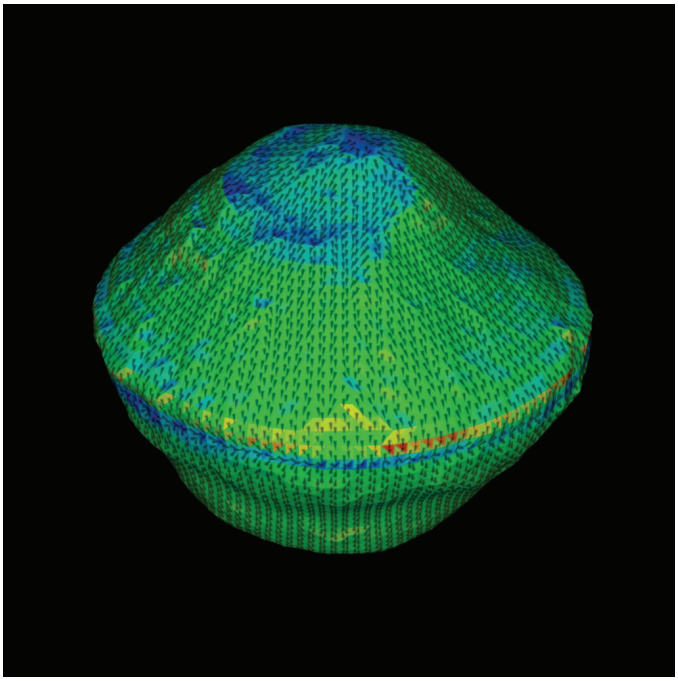

Figure 5.15: Effective gravitational sloped on KW4.

mapping investigation, for moving around the asteroid, or for station keeping orbit, communicating with hoppers on Alpha. Direct or retrograde orbits can be computed. It is found that retrograde periodic orbits are stable when very close to the surface. Figure 5.16 shows a stable retrograde orbit at a 10-meter altitude from the surface of Alpha. The stability of the periodic orbit changes near an altitude of 60 meters. Figure 5.17 shows a periodic orbit at 100 meters from the surface. The instabilities are strong and a spacecraft or particle may be brought on an impact trajectory toward Beta.

5.3.9 End of Mission Scenario

Hoppers that have not been lost can meet again on the opposite side of Alpha and eventually be brought to Earth. A possible option is for the hoppers to be equipped with a small launching device that can put it in orbit with enough energy to rendezvous with the spacecraft. Since Alpha is spinning at $2.15°/min$, timing of

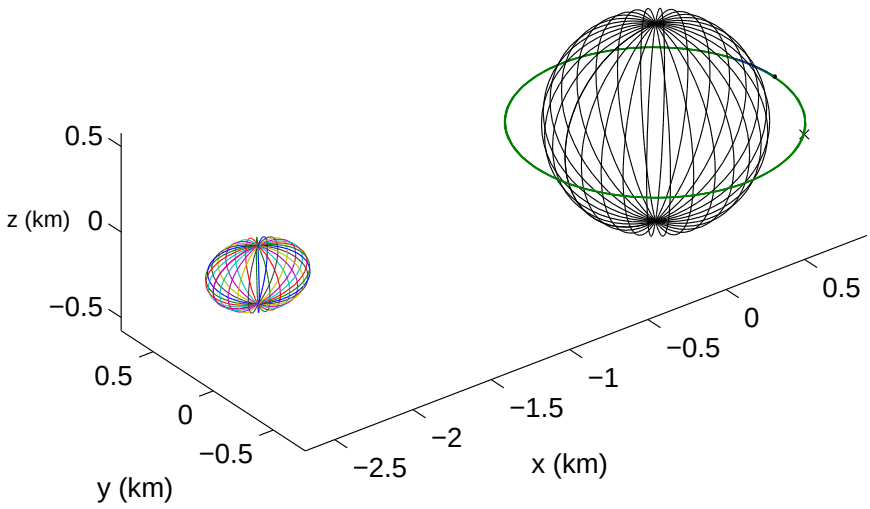

Figure 5.16: Stable retrograde periodic orbits around the massive spherical body of a binary system. The spacecraft is at an altitude of 15 meters from the surface.

this operation might be a challenge. Figure 5.18 shows a departure scenario where the hoppers leave Alpha through L_2. In order to pass by L_2, a hopper needs to launch at 0.85 m/s at least.

Another option would be for the hoppers to meet with the spacecraft on an orbit around Alpha as described in the previous section. The launching capability of the hoppers can then be reduced greatly, simplifying the design of the surface probes. Timing issues are also partially solved with this departure situation. The spacecraft can then leave Alpha through the same L_2 opening shown in Figure 5.18.

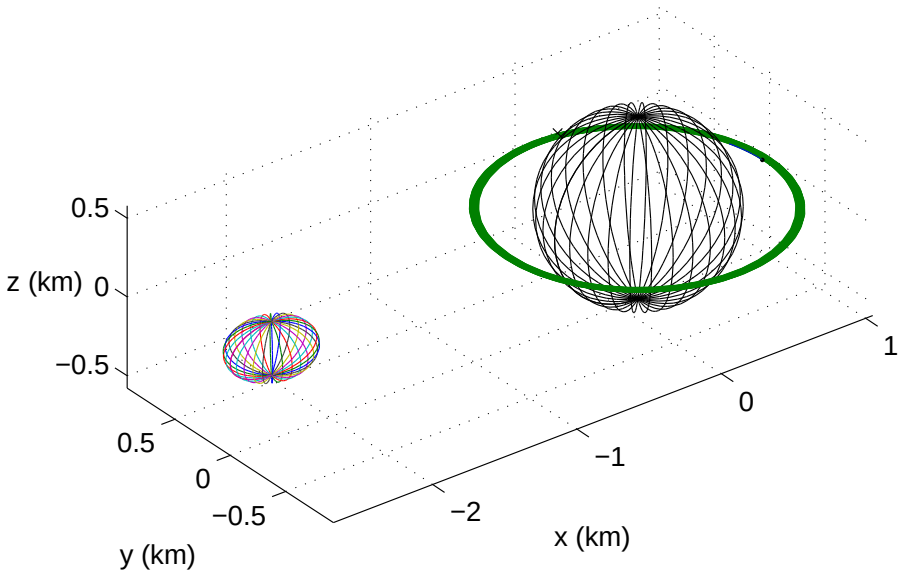

Figure 5.17: Unstable retrograde periodic orbits around the massive spherical body of a binary system. The spacecraft is at an altitude of 100 meters from the surface.

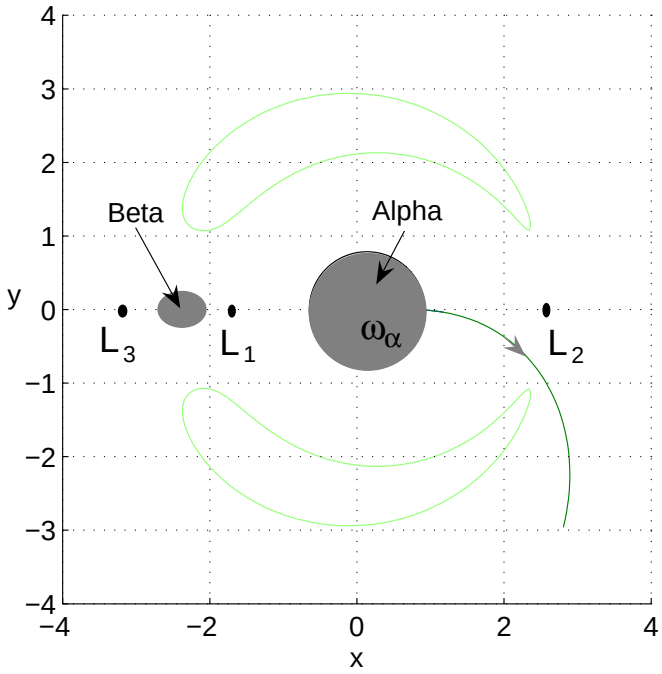

Figure 5.18: End of mission scenario: the hoppers can leave α through L_2 and rendezvous with the spacecraft in orbit about KW4.

5.4 Comparing 1999 KW4 to Other Known Binary Systems

5.4.1 Known Binary Systems

Unfortunately, the binary system 1999 KW4 is one of the least accessible binary systems in terms of ΔV, as calculated on the website "Binary near-Earth asteroids detected by radar" by L. Benner [30]. However, the methods developed for the F2BP and RF3BP and the mission design described in the previous sections can be applied to a few known, more easily accessible binary systems. There are a number of publications on observations of binary systems in the Near-Earth (NEA) and Main Belt Asteroids (MBA) population. References [71, 58, 59, 68, 70, 65, 69, 67, 55, 96] are only a few on radar imaging or photometry of binary asteroid systems within the NEA population, from which data will be useful to compare with 1999 KW4.

Some of these binary systems are listed in Table 5.2, with some orbital and physical characteristics of interest, and ΔV requirements relative to Earth. In this table, ΔV is the velocity required in order to reach the binary system from Earth, P_1, P_2, and P_{mut} are the periods of the primary, secondary, and mutual orbit of the system, D_1 and D_2 are the primary and secondary projected diameter, and r_b is the distance between the two. The last column was added to give a nondimensional distance between the binary bodies following the scaling defined for the F2BP and the RF3BP. Although a few systems are missing key parameters such as the period of the secondary body to determine the state of the system, i.e. in relative equilibrium or not, it is possible to find interesting cases. In fact, most of the binaries where the desired parameters have been obtained, binary systems 1 to 6, are in relative equilibrium, and are among the cheapest in terms of ΔV.

Note that some observations have also even catalogued a few asteroid systems composed of more than two asteroids [54]. This topic is left for future study.

#	Binary	ΔV (km/s)	P_1 (hr)	P_2 (hr)	P_{mut} (hr)	D_2/D_1	D_1 (km)	D_2 (km)	r_b (km)	r
1	Didymos (1996GT)	5.102	2.26	11.9	11.9	0.22	0.75	0.165	1.1	13.33
2	2000 DP107	5.97	2.77	42.20	42.20	0.41	0.8	0.328	2.6	15.85
3	1999 DJ4	6.04	2.51	17.73	17.73	0.5	0.35	0.175	0.8	9.14
4	1991 VH	6.37	2.62	NA	32.69	0.4	1.1	0.44	3.2	14.54
5	1996 FG3	6.61	3.59	16.15	16.14	0.31	1.5	0.465	2.6	11.18
6	1998 PG	6.66	2.52	14.01	NA	0.3	0.9	0.27	1.5	11.11
7	Dionysus (1984KD)	6.75	2.71	NA	27.74	0.2	1.5	0.3	3.8	25.33
8	2000 UG11	6.88	4.44	NA	18.4	0.6	0.26	0.156	0.4	5.13
9	Hermes (937UB)	7.78	13.89	13.89	NA	0.9	0.6	0.54	NA	NA
10	2001 SL9	9.32	2.4	NA	16.4	0.28	0.8	0.224	1.4	12.5
11	1994 AW1	10.25	2.52	NA	22.3	0.49	1.0	0.49	2.3	9.39
12	1999 HF1	13.03	2.32	NA	14.03	0.23	NA	NA	7.0	NA
13	2002 CE26	14.08	3.29	NA	16	0.07	3	0.21	5.1	48.57
14	2003 YT1	16.47	2.34	< 6	30	0.18	1.0	0.18	2.7	30
15	1998 RO1	19.4	2.49	14.52	14.54	> 0.4	NA	NA	1.4	NA
16	1999 KW4	21.3	2.765	17.45	17.44	[0.3,0.4]	1.5	0.57	2.54	8.91

Table 5.2: Orbital, physical, and ΔV characteristics of Near Earth Asteroid systems [30, 71, 96]

5.4.2 Comparison with 1999 KW4: Similarities and Differences

From looking at Table 5.2, the system 1996 FG3 seems to be the closest to 1999 KW4. The asteroid sizes and the distance between the bodies are very similar. Hence, the velocities and orbits described in the previous section are fairly representative of this system as well. However, 1996 FG3 requires about 3 times less ΔV than 1999 KW4. Since the primary is spinning at a slower rate than Alpha, dynamics and control on that asteroid may be easier to handle.

Didymos is about half the scale of KW4, and the ratio of the two asteroid diameters is also 10% smaller. While the system is in relative equilibrium, the small scale of the binary would make any surface motion on the small body difficult to estimate and control from the low gravity at such a small scale. To date, the smallest size asteroid visited by a probe was Itokawa with dimensions 535 m $\times$ 294 m $\times$ 209 m, target of the Hayabusa mission [49, 57, 21, 99], which is twice as big as the secondary of Didymos. A mission may decide to avoid attempting to reach the secondary in this case. With the primary still spinning much faster than the orbit rate, navigation, control, and surface operations may be a great challenge.

While having a similar distance r_b compared to KW4, the bodies of 2000 DP107 are also about half the size of Alpha and Beta. Hence, the system has a nondimensional separation distance r twice as large as KW4. As for Didymos, dynamics and control for surface exploration would be a challenge even though the asteroids are at least the size of Itokawa.

1999 DJ4 has similar orbital periods for the primary and the mutual orbit of the system compared to KW4. However, the overall system is at a much smaller scale, with the primary being almost half the size of Beta. Although slightly bigger, the system 1998 PG is a similar case as 1999 DJ4.

In order to have a better insight of the surface operations and the velocities

involved on binary systems discussed above, Table 5.3 give preliminary computations for the binary system energy constraints, orbital velocities, and surface velocities for transfer between the two bodies. Note that r_1, r_2, are the distance of primary and secondary with respect to their center of mass, and V_1, V_2, and V_{sys} are the orbital velocities around the primary, the secondary, and around the binary system, respectively. The orbital radius were chosen to be between 20 and 30 m away from the surface of each body, and 2 km away from the system center of mass. The computations assume equal density of 2.2 g/m^3 for the binary bodies, with both having a spherical shape.

Asteroid	Mass ratio	r_1 km	r_2 km	L_1 km	L_2 km	L_3 km	L_4 km	V_1 m/s	V_2 m/s	V_{sys} m/s
Didymos (1996GT)	0.9895	0.011	-1.09	-0.9292	1.1045	-1.2635	-0.5383 0.9524	0.28	0.006	0.11
2000 DP107	0.9355	0.17	-2.43	-1.7714	2.6692	-2.4317	-1.1320 2.2511	0.30	0.030	0.106
1999 DJ4	0.8889	0.09	-0.71	-0.4705	0.8367	-1.0103	-0.3111 0.6925	0.12	0.020	0.04
1996 FG3	0.9945	0.014	-2.525	-2.2800	2.6053	-2.5851	-1.2854 2.2511	0.58	0.007	0.28
1998 PG	0.9737	0.04	-1.46	-1.1720	1.5163	-1.7912	-0.7105 1.2989	0.34	0.015	0.14

Table 5.3: Orbital parameters of target binary systems.

Observations for the other binary systems listed in Table 5.2 are missing period of the secondary or distance between the bodies. Hence, it is not possible to infer the state of the system, i.e. in stable relative equilibrium or not. However, from the sizes reported and some periods, binary systems 1991 VH, Dionysus, Hermes, and 1994 AW1 could be interesting options to pursue. It can be noted that Hermes is the only asteroid system thought to have both the primary and the secondary in synchronized motion. Also, although the bodies are small, 2000UG11 may also be of interest since the distance between the body is smaller than other binary systems. Again, further observations would be necessary to find other potential targets for a mission to a binary and refine the above assumptions.

5.4.3 Extension to Planetary Flyby Opportunities

Since binaries are thought to have formed from rotational fission or planetary flybys [82, 96, 12], it would be interesting to have a mission going to asteroids coinciding with a flyby opportunity. In doing so, the change in rotation rate could be measured, validating theories on rotational fission, tidal effects, and rubble-pile or aggregate asteroid models. In the case of fission, the system would reveal its internal structure directly. In addition, the event would also give further evidence of the evolution paths of a binary, going from an unstable to a stable state say as the bodies drift apart, described in Chapter 2.

In order to scientifically investigate a flyby opportunity, one of the best approaches would be to have a net of surface probes acting as target markers. With a small driving mechanism device, these probes could be designed to move in a collaborating manner from a release location on the surface to a defined grid, as approached in Chapter 4. As the shape of the body changes over time, a three dimensional differential shape would be obtained from the network of probes, which can be measured by a spacecraft in orbit close to the system.

Looking at the JPL Near Earth Program, there will be opportunities to observe the effect of planetary flyby on asteroid systems [31]. It was shown that binary encounters with Earth or Venus out to 8 planet radii can alter orbit properties of the binary [12, 11, 17]. Hence, in order to choose a close approach distance suitable for science investigation, the search was done for flyby closer than the Moon relative to Earth. Results are presented in Table 5.4. Asteroids 2005yr3, 2001av43, and 2001wn15 may be interesting targets to consider since they will flyby Venus, Earth, and Mercury in a near time frame. Note that, to date, no binary systems are predicted to make a flyby at such a close approach distance.

Asteroid	Date of CA	Planet flyby	Distance CA (AU)
2007eh	2012 Feb 14.6	Jupiter	1.77226
2005yr3	2012 Dec 21.5	Venus	0.00247
2001av43	2013 Nov 18.7	Earth	0.00742
2001wn15	2015 May 28.7	Mercury	0.0026
2006ec	2023 Mar 4.1	Earth	0.06975 (.000210 min)
2007eh	2024 Sep 19.3	Jupiter	1.74327
137108	2027 Aug 7.3	Earth	0.00261
153814	2028 Jun 26.2	Earth	.001671
99942	2029 Apr 13.9	Earth	0.00025
1994vh8b	2031 Oct 30.3	Moon	0.00210
1994vh8b	2031 Oct 29.9	Earth	0.00218
2007hw4	2032 Sep 10.8	Venus	0.00256
2005ta	2034 Oct 5.3	Moon	0.00130
2002ta58	2061 Oct 8.3	Earth	0.0016
2002ta58	2061 Oct 8.3	Moon	0.0020
2000bm19	2063 Mar 3.0	Venus	0.00181
2006ec	2063 Mar 9.1	Moon	0.0024
2006ec	2063 Mar 9.3	Earth	0.00221
2000qx69	2064 Aug 23.1	Earth	0.00255
2001av43	2064 Nov 13.4	Earth	0.00438
2003jy2	2066 Jun 11.3	Venus	0.00228
2000sg344	2069 May 2.0	Earth	0.00129
2000sg344	2069 May 4.0	Moon	0.00033
2001oa14	2073 Feb 14.2	Mars	0.00220
2004ru10	2079 Nov 16.9	Mercury	0.00263

Table 5.4: Close approaches of asteroids [31]

CHAPTER 6

CONCLUSIONS AND FUTURE DIRECTIONS

6.1 Summary and Contributions

This final chapter summarizes the methods, findings and contributions of the previous chapters. Then, future research directions are discussed.

6.1.1 The Restricted Full Three Body Problem

This objective of this work is to enable spacecraft missions to a binary asteroid system. In order to solve the problem of spacecraft orbiters near a binary, one needs to first solve for the dynamics of the two bodies themselves. By looking at an ellipsoid-sphere system, the problem is greatly simplified while keeping interesting dynamical features. This work first looks at the conditions for which the relative configuration of the ellipsoid-sphere system is locked, and how the binary system may evolve in time. It was found that two equilibrium states exist for a given a value of angular momentum, where only the distance between the binary bodies differs. It was also demonstrated that these solutions are opposite in stability, with the system being unstable when the bodies are close to each other. Then, from looking at small perturbations in the vicinity of these equilibrium solutions, periodic orbit families were computed using a Poincaré map method. It is found that the lowest energy state of these periodic families is precisely at the relative equilibrium state itself. From looking at the energy of the system, it is possible to find paths where the binary system may evolve from an unstable close configuration to a stable state.

Then, having defined the dynamics of the binary system, one can then look at the motion of particles or spacecraft in its vicinity. Two different problems were investigated, when the two bodies keep the same configuration as they orbit each other, and when periodic perturbations are introduced. In the first case, the energy constraints were characterized and compared to the known Restricted Three Body Problem. This can be done using current tools in astrodynamics, such as the Jacobi integral, zero-velocity curves, and equilibrium solutions. Interestingly, the results indicate that it may not be feasible to assume that the equilateral triangle equilibrium point analogues in the RF3BP will be appropriate orbits from which to observe a binary system. While the gravitational models used in this analysis are rather approximate and simplified, it is probable that adding additional realism will tend towards decreasing the stability regions even further.

Periodic orbits around the binary and around one of the two asteroids can also be computed, and may be used as reconnaissance orbits. Then, looking specifically at the mid-regions between the bodies, the nature of the collinear point allows transfer trajectories. Knowing the transit conditions, the corresponding surface conditions on the bodies can be computed from integrating the RF3BP equations of motion. This is unique for binary systems and provides a novel research opportunity in terms of small body exploration. As an extension to this, if the bodies are close to each other, material exchange may be possible, providing insights on the system evolution.

Accounting for small perturbations, the challenge is to integrate the dynamics of the binary into the model for the RF3BP. Assuming a constant motion in both the F2BP and the RF3BP, periodic orbits near the equilateral Lagrangian points L_4 and L_5 were computed. Then, using approximations for the ellipsoid potential, analytical methods were derived in order to facilitate and complete the computations. Periodic orbits can also be investigated using Poincaré maps and small approximations for the dynamics of the F2BP itself, giving more accurate results and insights on the

true dynamics.

6.1.2 Robotic Exploration and Applications

The models and findings from the F2BP and the RF3BP are integrated for applications into robotic exploration of binary systems. Having a physical shape for the binary components introduces surface constraints and forces one to develop prediction methods for the dynamics and control of surface exploration landers. Since the gravity is low on asteroids, an analytical model is derived using impacts, predicting the total distance covered and time of travel while accounting for a non-uniform gravity field, and coefficients of friction and restitution. However, it was found that the dynamics of a rotating body has an important influence on the dynamics of surface landers as they may get attracted to stable regions of the body. Hence, control for surface motion may be desired in order to investigate certain regions that are not dynamically reachable. The control is developed for a single hopper and extended to collaborative probes.

Finally, integrating all methods, the last chapter showed a case study for the binary system 1999 KW4 and provided a discussion on other binary systems of interest. From energy constraint considerations and environmental stability, it was shown how a mission can take fully advantage of the system dynamics by approaching through the smallest body which is locked in configuration with respect to the primary. Then, after landing on the small ellipsoid, the hoppers can make their way to the other end of the small body, and transit to the primary.

The current interest in asteroid systems combined with the discussion presented on the methods and findings of spacecraft orbiters at binaries can hopefully be considered as a motivation to design one of the next low-cost Near-Earth Object robotic missions towards such a system.

6.2 Future Research Directions

There are many refinements and extensions that can be made to the current model. The gravitational influence of the sun may be an important perturbation to the dynamics of asteroids, which was not accounted for in the present work. The solar radiation has also been shown to have an effect on the rotational state of an asteroid, also called YORP effect [13, 81, 83]. Considering these effects on a binary system will most likely give very rich dynamics to investigate. A natural extension is to model systems of more than two bodies, such as the triple asteroidal system 87 Sylvia [54].

There may also be other regions or specific orbits of interest, especially considering out of plane orbits, where these external perturbations may be coupled to the in-plane dynamics. Then, taking a full model for the binary system, such as done in [18, 52], and looking at the three dimensional motion, would take this analysis a step further. These are also enabling elements for missions to binaries in order to improve and develop more accurate and robust tools for guidance and navigation near small bodies or on their surface.

In addition, beside improving on all mission subsystems, the robotic exploration dynamics and control can be researched in more detail, and developed for specific mission operations. As an example, one of the topics not fully well understood is the effect of a planet on an asteroid as it flies by it. Tidal forces are difficult to evaluate since the composition itself and type of aggregate are not well known. It would be interesting to look into how robotic missions may be used to understand and provide more data on these possible dynamical interactions. The next step is to develop and prototype an actual surface robot for the exploration purposes. The attitude dynamics would then need to be considered and studied, as there will be coupling with the translational and rotational dynamics.

In the same line of thought, research is needed to develop accurate guidance and

control law, and navigation methods for probe formations on small bodies. Current interest is to have small landers on the surface or probes under the surface for geological measurements. In terms of surface motion, the real surface of asteroids may bring many disturbances in the motion of a lander if the surface is made of loose regolith. A simple way to include these perturbations is to include and simulate the dynamics using random errors added to the state variables. Then, surface motion and operations may be designed with the help of a probabilistic knowledge on the current position.

Finally, as a more futuristic topic, robotic missions to small bodies can also serve as precursors to human exploration of asteroids [50]. The current Moon and Mars programs from the U.S. Vision declared by President Bush in 2003 has revived the interest in lunar activities, being the next step before sending human to Mars. In order to prepare for such an endeavor, small bodies need to be further studied to serve as possible human exploration missions, providing a short trip to outer space.

BIBLIOGRAPHY

[1] S. Abe, T. Mukai, N. Hirata, O. Barnouin-Jha, A. Cheng, H. Demura, R.W. Gaskell, T. Hashimoto, K. Hiraoka, T. Honda, T. Kubota, M. Matsuoka, T. Mizuno, R. Nakamura, D. Scheeres, and M. Yoshikawa. Mass and local topography measurements of itokawa by hayabusa. *Science*, 312:1344–1347, 2006.

[2] T.D. Barfoot and C.M. Clark. Motion planning for formations of mobile robots. *Robotics and Autonomous Systems*, 46:65–78, 2004.

[3] R. Beard, J. Lawton, and F. Hadaegh. A coordination architecture for spacecraft formation control. *IEEE Transactions on Control Systems Technology*, 9, 6:777–790, 2001.

[4] J. Bellerose and D.J. Scheeres. Periodic orbits in the full two body problem. Number IAC-06-C1.5.05. International Astronautical Congress, 2006.

[5] J. Bellerose and D.J. Scheeres. Stability of equilibrium points in the restricted full three body problem. *Acta Astronautica*, 60:141–152, 2007.

[6] J. Bellerose and D.J. Scheeres. Energy and stability in the full two body problem. *Celestial Mechanics and Dynamical Astronomy*, 100(1):63–91, 2008.

[7] J. Bellerose and D.J. Scheeres. The restricted full three-body problem: Application to binary system 1999 kw4. *Journal of Guidance, Control, and Dynamics*, 31(1):162–171, 2008.

[8] J. Bellerose and D.J. Scheeres. Periodic orbits in the full two-body problem. Number AAS-06-169. AAS/AIAA Spaceflight Mechanics Conference, 22-26 January 2006.

[9] J. Bellerose and D.J. Scheeres. Energy constraints in the restricted full three-body problem: Application to binary system 1999 kw4. Number AAS-07-224. AAS/AIAA Spaceflight Mechanics Conference, 28 January - 1 February 2007.

[10] J. Bellerose and D.J. Scheeres. Periodic orbits in the vicinity of the equilateral points of the restricted full three-body problem. Number AAS-05-295. AAS/AIAA Astrodynamics Specialists Conference, 7-11 August 2005.

[11] W.F. Bottke and H.J. Melosh. The formation of asteroid satellites and doublet craters by planetary tidal forces. *Nature*, 381:51–53, 1996.

[12] B. Chauvineau and P. Farinella. The evolution of earth-approaching binary asteroids: A monte carlo dynamical model. *Icarus*, 115:36–46, 1995.

[13] S.R. Chesley and 9 colleagues. Direct detection of the yarkovsky effect by radar ranging to asteroid 6489 golevka. *Science*, 302:1739–1742, 2003.

[14] C.C. Conley. Low energy transit orbits in the restricted three-body problem. *SIAM Journal of Applied Mathematics*, 16 (4):732–746, July 1968.

[15] J.M.A. Danby. *Fundamentals of Celestial Mechanics*. Willmann-Bell, VA, second edition, 1992.

[16] P. D'Arrigo and S. Santandrea. The apies mission to explore the asteroid belt. *Advances in Space Research*, 38 (9):2060–2067, 2006.

[17] F. Marzari D.J. Scheeres and A. Rossi. Evolution of neo rotation rates due to close encounters with earth and venus. *Icarus*, 170:312–323, 2004.

[18] E.G. Fahnestock and D.J. Scheeres. Simulation and analysis of the dynamics of binary near-earth asteroid (66391) 1999 kw4. *Icarus*, NA:NA, 2008.

[19] B.P. Flannery, W.H. Press, S.A. Teukolsky, and W.T. Vetterling. *Numerical Recipies in C, The Art of Scientific Computing*. Cambridge University Press, second edition, 1996.

[20] R.L. Forward. *Rocheworld*. Baen, 1990.

[21] A. Fujiwara, J. Kawaguchi, D. K. Yeomans, M. Abe, T. Mukai, T. Okada, J. Saito, H. Yano, M. Yoshikawa, D. J. Scheeres, O. Barnouin-Jha, A. F. Cheng, H. Demura, R. W. Gaskell, N. Hirata, H. Ikeda, T. Kominato, H. Miyamoto, A. M. Nakamura, R. Nakamura, S. Sasaki, and K. Uesugi. The rubble-pile asteroid itokawa as observed by hayabusa. *Science*, 312:1330–1334, 2006.

[22] F. Gabern, W.S. Koon, J.E. Marsden, and D.J. Scheeres. Binary asteroids observation orbits from a global dynamical picture. *SIAM Journal on Applied Dynamical Systems*, 5 (2):252–279, 2006.

[23] D.T. Greenwood. *Principles of Dynamics*. Prentice-Hall, New York, 2nd ed., 1988.

[24] V. Guibout and D.J. Scheeres. Stability of surface motion on a rotating ellipsoid. *Celestial Mechanics and Dynamical Astronomy*, 87:263–290, 2003.

[25] V.M. Guibout and D.J. Scheeres. Spacecraft formation dynamics and design. 29 (1):121–133, 2006.

[26] M. Hénon. Exploration numérique du problème restreint ii. *Annales Astronautiques*, pages 992–1007, 1965.

[27] J.-F. Hamel and J. de Lafontaine. Linearized dynamics of formation flying spacecraft on a j2-perturbed elliptical orbit. 30 (6):1649–1658, 2007.

[28] J. Hedrick, M. Tomizuka, and P. Varaiya. Control issues in automated highway systems.

[29] DAWN http://dawn.jpl.nasa.gov/.

[30] L. Benner http://echo.jpl.nasa.gov/ lance/binary.neas.html last updated 11/26/07.

[31] S. Chesley http://neo.jpl.nasa.gov/ last updated 01/29/08.

[32] Near Earth Asteroid Rendezvous http://nssdc.gsfc.nasa.gov/planetary/near.html.

[33] New Horizons Pluto Charon http://pluto.jhuapl.edu/index.php.

[34] ESA Near Earth Asteroid Sample Return http://sci.esa.int/science e/www/object/index.cfm?fobjectid=40608.

[35] NASA Deep Impact Mission http://solarsystem.nasa.gov/deepimpact/index.cfm.

[36] NASA WISE http://solarsystem.nasa.gov/missions/profile.cfm?MCode=WISE.

[37] Stardust NASA Comet Sample Return Mission http://stardust.jpl.nasa.gov/home/index.html.

[38] Phobos-Grunt http://www.aerospaceguide.net/mars/phobos grunt.html.

[39] EADS Astrium APIES http://www.astrium.eads.net/families/exploring-the-universe/solar system/apies.

[40] European Space Agency Rosetta http://www.esa.int/esaMI/Rosetta/index.html.

[41] ESA SIMONE http://www.esa.int/gsp/completed/neo/simone.html.

[42] ESA NEO Space Mission Preparation http://www.esa.int/SPECIALS/NEO/SEMZRZNVGJE 0.html.

[43] NASA Stardust Status Report http://www.nasa.gov/mission pages/stardust/news/stardust 20070201.html.

[44] CNES Leonard http://www.sp.ph.ic.ac.uk/ nach/NEO:Reports from OU/Appendix C2 Barucci.pdf.

[45] W.M. Kaula. *Theory of Satellite Geodesy.* Blaisdell Publishing Company, Waltham, Massachusetts, 1966.

[46] J. Kawaguchi and F. Terui. International collaboration and global exploration. AIAA 3rd Space Exploration Conference, February 26-28 2008.

[47] E. Kuehrt. S1-4 dlr vision and plan. First Meeting of The International Primitive Body Exploration Working Group (IPEWG), January 13-16 2008.

[48] E. Kuhrt, S. Mottola, G. Hahn, A. Borner, and S. Montenegro. S5-9 asteroidfinder - a proposal for a dlr compact satellite mission. First Meeting of The International Primitive Body Exploration Working Group (IPEWG), January 13-16 2008.

[49] J. Hitoshi Kuninaka, A. Fujiwara, and Tono Uesugi. Muses-c, its launch and early orbit operation. *Acta Astronautica*, 59:669–678, 2006.

[50] R.R. Landis, D.J. Korsmeyer, P.A. Abell, and D.R. Adamo. A piloted orion flight to a near-earth object: A feasibility study. Number AIAA-2007-6168. AIAA SPACE 2007 Conference and Exposition, 2007.

[51] P. Lee, R. Richards, A. Hildebrand, and the PRIME Mission Team. Prime: A small body mission at mars. Canadian Space Astronomy Workshop, Nov 23-24, 2006.

[52] T. Lee, M. Leok, and N.H. McClamroch. Lie group variational integrators for the full body problem in orbital mechanics. *Celestial Mechanics and Dynamical Astronomy*, 98(2):121–144, 2007.

[53] A.J. Maciejewski. Reduction, relative equilibria and potential in the two rigid bodies problem. *Celestial Mechanics and Dynamical Astronomy*, 63:1–28, 1995.

[54] F. Marchis, P. Descamps, D. Hestroffer, and J. Berthier. Discovery of the triple asteroidal system 87 sylvia. *Nature*, 436:822–824, 2005.

[55] J.-L. Margot, M.C. Nolan, L.A.M. Benner, S.J. Ostro, R.F. Jurgens, J.D. Giorgini, M.A. Slade, and D.B. Campbell. Binary asteroids in the near-earth object population. *Science*, 296(5572):1445–1448, 2002.

[56] P. Michel. S2-3 a binary asteroid as a target of a space mission : Scientific interest. First Meeting of The International Primitive Body Exploration Working Group (IPEWG), January 13-16 2008.

[57] T.G. Mller, T. Sekiguchi, M. Kaasalainen, M. Abe, and S. Hasegawa. Itokawa: The power of ground-based mid-infrared observations. *International Astronautical Union*, 2:261–266, 2006.

[58] S. Mottola, G. Hahn, P. Pravec, and L. Sarounova. S/1997 (3671). *IAU Circ*, 6680, 1997.

[59] S. Mottola and F. Lahulla. Mutual eclipse events in asteroid binary system 1996 fg3: Observations and a numerical model. *Icarus*, 146:556–567, 2000.

[60] F.R. Moulton. *Differential Equations*. Dover, 1970.

[61] F.R. Moulton. *An Introduction to Celestial Mechanics*. Dover, 1970.

[62] First Meeting of The International Primitive Body Exploration Working Group (IPEWG) January 13-16 2008 Japan The http://www.jspec.jaxa.jp/okinawa index.html.

[63] R. Olfati-Saber and R. Murray. Graph rigidity and distributed formation stabilization of multi-vehicle systems. 3:2965–2971, 2002.

[64] S.J. Ostro, J.L. Margot, L.A.M. Benner, J.D. Giorgini, D.J. Scheeres, E.G. Fahnestock, S.B. Broschart, J. Bellerose, M.C. Nolan, C. Magri, P. Pravec, P. Scheirich, R. Rose, R.F. Jurgens, E.M. De Jong, and S. Suziki. Radar imaging of binary near-earth asteroid (66391) 1999 kw4. *Science*, 314:1276–1280, 2006.

[65] S.J. Ostro, J.L Margot, M.C. Nolan, L.A.M. Benner, R.F Jurgens, and J.D. Giorgini. 2000 dp107. *IAU Circ*, 7596, 2000.

[66] A. Pant, P. Seiler, and K. Hedrick. Mesh stability of look-ahead interconnected systems. *IEEE Transactions on Automatic Control*, 47, 2:403–407, 2002.

[67] P. Pravec and 10 collegues. Two-period lightcurves of 1996 fg3, 1998 pg, and (5407) 1992 ax: One probable and two possible binary asteroids. *Icarus*, 146:190–193, 2000.

[68] P. Pravec and 11 collegues. (65803) 1996 gt. *IAU Circ*, 8244, 2003.

[69] P. Pravec, P. Kusnirak, M. Hicks, B. Holliday, and B. Warner. 2000 dp107. *IAU Circ*, 7504, 2000.

[70] P. Pravec, P. Kusnirak, L. Sarounova, P. Brown, N. Kaiser, G. Masi, and F. Mallia. 1999 dj4. *IAU Circ*, 8316, 2004.

[71] P. Pravec, P. Scheirich, P. Kuniraka, L. arounova, S. Mottola, G. Hahnb, P. Brownc, G. Esquerdo, N. Kaiser, Z. Krzeminski, D.P. Prayd, B.D. Warner, A.W. Harris, M.C. Nolang, E.S. Howell, L.A.M. Benner, J.-L. Margot, A. Galad, W. Holliday, M.D. Hicks, Yu.N. Krugly, D. Tholen, R. Whiteley, F. Marchis, D.R. DeGraff, A. Grauer, S. Larsonn, F.P. Velichko, W.R. Cooney Jr., R. Stephens, J. Zhut, K. Kirschu, R. Dyvigu, L. Snyder, V. Reddy, S. Moorex, Gajdo, J. Vilagi, G. Masi, D. Higgins, G. Funkhouser, B. Knight, S. Slivanab, R. Behrendac, M. Grenonac, G. Burki, R. Royad, C. Demeautis, D. Matter, N. Waelchli, Y. Revazaf, A. Klotz, M. Rieugne, P. Thierryag, V. Cotrezai, L. Brunetto, and G. Kober. Photometric survey of binary near-earth asteroids. *Icarus*, 181:63–93, 2006.

[72] J.E. Prussing and B.A. Conway. *Orbital Mechanics*. Oxford University Press, NY, first edition, 1993.

[73] R. Richardson and W.F. Bottke S.G. Love. Tidal distortion and disruption of earth-crossing asteroids. *Icarus*, 134:47–76, 1998.

[74] F. Rocard, E. Linglais, and A. Barucci. S5-6 cnes report on leonard mission : A study of in-situ analysis of a near-earth object. First Meeting of The International Primitive Body Exploration Working Group (IPEWG), January 13-16 2008.

[75] S. Sawai, J. Kawaguchi, D. Scheeres, N. Yoshizawa, and M. Ogasawara. Development of a target marker for landing on asteroids. *Journal of Spacecraft and Rockets*, 38 (4):601–608, 2001.

[76] D.J. Scheeres. *On Symmetric Central Configurations with Application to Satellite Motion about Rings*. 1992.

[77] D.J. Scheeres. The restricted hill four-body problem with applications to the earth-moon-sun system. *Celestial Mechanics and Dynamical Astronomy*, 70:75–98, 1998.

[78] D.J. Scheeres. Stability in the full two body problem. *Celestial Mechanics and Dynamical Astronomy*, 83:155–169, 2002.

[79] D.J. Scheeres. Stability of relative equilibria in the full two-body problem. *Annals of the New York Academy of Sciences*, 1017:81–94, 2004.

[80] D.J. Scheeres. Relative equilibria for general gravity fields in the sphere-restricted full 2-body problem. *Celestial Mechanics and Dynamical Astronomy*, 94(3):317–349, 2006.

[81] D.J. Scheeres. The dynamical evolution of uniformly rotating asteroids subject to yorp. *Icarus*, 188:430–450, 2007.

[82] D.J. Scheeres. Rotational fission of contact binary asteroids. *Icarus*, 189:370–385, 2007.

[83] D.J. Scheeres, M. Abe, M. Yoshikawa, R. Nakamura, R.W. Gaskell, and P.A. Abell. The effect of yorp on itokawa. *Icarus*, 188:425–429, 2007.

[84] D.J. Scheeres and S. Augenstein. *Spacecraft Motion about Binary Asteroids*, volume 116 of *Astrodynamics 2003, Part II, Advances in the Astronautical Sciences Series*, pages 991–1010. 2003.

[85] D.J. Scheeres and J. Bellerose. The restricted hill full 4-body problem: Application to spacecraft motion about binary asteroids. *Invited paper in a special issue of Dynamical Systems: An International Journal. Edited by M.Dellnitz and J.E.Marsden*, 20(1):23–44, 2005.

[86] D.J. Scheeres and E.G. Fahnestock. Simulation of the full two rigid body problem using polyhedral mutual potential and potential derivatives approach. *Celestial Mechanics and Dynamical Astronomy*, 96(3-4):317–339, 2006.

[87] D.J. Scheeres, E.G. Fahnestock, S.J. Ostro, J.L. Margot, L.A.M. Benner, S.B. Broschart, J. Bellerose, J.D. Giorgini, M.C. Nolan, C. Magri, P. Pravec, P. Scheirich, R. Rose, R.F. Jurgens, E.M. De Jong, and S. Suziki. Dynamical configuration of binary near-earth asteroid (66391) 1999 kw4. *Science*, 314:1280–1283, 2006.

[88] D.J. Scheeres, B.G. Williams, and J.K. Miller. Evaluation of the dynamics environment of an asteroid: Application to 433 eros. *Journal of Guidance, Control and Dynamics*, 23:466–475, 2000.

[89] D. Shiga, http://space.newscientist.com/article/dn11001, and NewScientist.com 22 January 2007.

[90] D. Swaroop and J. K. Hedrick. String stability of interconnected systems. *IEEE Transactions on Automatic Control*, 41, 3:349–357, 1996.

[91] V. Szebehely. *Theory of Orbits*. Academic Press, NY, first edition, 1967.

[92] M. Tillerson, L. Breger, and J. How. Distributed coordination and control of formation flying spacecraft. 2:1740–1745, 2003.

[93] C. Trenkel, P. DArrigo, and S. Barraclough. S5-8 apex: A mission concept to explore the physical properties of asteroid apophis and their impact on orbital evolution. First Meeting of The International Primitive Body Exploration Working Group (IPEWG), January 13-16 2008.

[94] G. Vane. S2-9 using very small rovers to explore the surface of primitive bodies. First Meeting of The International Primitive Body Exploration Working Group (IPEWG), January 13-16 2008.

[95] R. Walker, N. Wells, S. Green, and A. Ball. The simone mission: Close reconnaissance of the diverse neo population as a precursor to impact mitigation. Number AIAA 2004-1483. 2004 Planetary Defense Conference: Protecting Earth from Asteroids, 23 - 26 February 2004.

[96] K.J. Walsh and D.C. Richardson. Binary near-earth asteroid formation: Rubble pile model of tidal disruptions. *Icarus*, 180:201–216, 2006.

[97] S. Wiggins. *Global Bifurcation and Chaos*. Springer-Verlag, New York, 1998.

[98] T. Yamada. S2-12 marco-polo capsule and dash-ii mission. First Meeting of The International Primitive Body Exploration Working Group (IPEWG), January 13-16 2008.

[99] H. Yano, T. Kubota, H. Miyamoto, T. Okada, D. Scheeres, Y. Takagi, K. Yoshida, M. Abe, O. Barnouin-Jha, A. Fujiwara, S. Hasegawa, T. Hashimoto, M. Ishiguro, M. Kato, J. Kawaguchi, T. Mukai, J. Saito, S. Sasaki, and M. Yoshikawa. Touchdown of the hayabusa spacecraft at the muses sea on itokawa. *Science*, 312:1350–1353, 2006.

[100] T. Yoshimitsu, T. Kubota, and I. Nakatani. S2-10 proposal of micro rovers on small solar system bodies. First Meeting of The International Primitive Body Exploration Working Group (IPEWG), January 13-16 2008.

[101] T. Yoshimitsu, T. Kubota, I. Nakatani, T. Adachi, and H. Saito. Micro-hopping robot for asteroid exploration. *Acta Astronautica*, 52:441–446, 2003.

[102] Z. Zheng and A. Girard. Leaderless formation control using dynamic extension and sliding control. *IFAC World Congress*, 2008.

[103] T. Zohdi. Computational design of swarms. *International Journal for Numerical Methods in Engineering*, 57:2205–2219, 2003.